# MODEL DESIGN AND EXPERIMENTAL INVESTIGATION OF FLOATING WIND TURBINE

**A Thesis Submitted to**
**the Graduate School of Engineering and Sciences of**
**İzmir Institute of Technology**
**in Partial Fulfillment of the Requirements for the Degree of**

**MASTER OF SCIENCE**

**in Mechanical Engineering**

**by**
**Ali Arıdıcı**

**October 2022**
**İZMİR**

# ACKNOWLEDGMENTS

First, I would like to thank my supervisor Assoc. Prof. Ünver ÖZKOL, for inspiring knowledge and for including me in this great project. He has been a great mentor during my thesis study with his suggestions and by leaving me inspired and eager to learn more.

Secondly, thank all my colleagues with whom I collaborated on the project and who did not withhold their support and knowledge from me throughout the project and thesis. My sincere thanks to especially Assoc. Prof. Bergüzar ÖZBAHÇECİ always considers me as one of her students.

A big thanks go out to especially İsmail Gürkan DEMİRKIRAN and Ezgi ŞATIROĞLU always being ready to give suggestions and for some good discussions with me. Also, I owe a big thanks to İsmail for lots of thesis-writing hours and for supporting me like a big brother; I will never forget those times.

Last but not least, I would like to thank my family and Gülşah YARIMCA for always giving me fantastic and indispensable support. I can not thank them enough for the patience they have shown me. That means everything to me.

# ABSTRACT


## MODEL DESIGN AND EXPERIMENTAL INVESTIGATION OF FLOATING WIND TURBINE

Floating offshore wind energy has great potential (which constitutes almost 80% of total offshore wind energy) to meet electricity demand of the world at the same time to reach net-zero emission goal by 2050. Floating offshore wind turbines (FOWT) are able to achieve highest capacity factor since local effects of the offshore terrains are lesser. Thus, it receives stronger and more stable wind. On the other hand, combined hydrodynamic and aerodynamic forces with 6 degrees of freedom (DoF) bring unsteadiness and therefore, challenges on FOWT design. Furthermore, significant rotational motions, particularly pitch motion, lead the turbine to transient state which can not be simulated through conventional numerical tools. Therefore, to understand the dynamics of the FOWT, it is necessary to conduct experimental studies to obtain results by considering all the parameters.

The main aim of the thesis is to investigate the dynamic response of the FOWT under the extreme wind and wave conditions. A 1/40 Froude-scaled version of the Northel POYRA P36/300 mounted on the spar-type floating platform was developed by colleagues as a part of TUBITAK (217M451) project. In this thesis, experimental studies were carried out in the wave flume with a wind nozzle in the hydraulic laboratory of IZTECH Civil Engineering Department. Atmospheric boundary layer (ABL) was scaled, and instruments of the experiment were calibrated to characterize wind nozzle and wave maker, which are vital to obtaining reliable results. The wind nozzle was designed based on experimental data to reproduce correct Froude-scaled ABL.

# ÖZET

## YÜZER RÜZGAR TÜRBİNİ MODEL TASARIMI VE DENEYSEL İNCELENMESİ

Toplam denizüstü rüzgar enerjisi potansiyelinin neredeyse %80'ini oluşturan denizüstü yüzer rüzgar enerjisi, dünyanın elektrik talebini karşılama ve 2050 yılı için sıfır emisyon hedefine ulaşmada büyük potansiyele sahiptir. Denizüstü bölgelerde arazilerin lokal özelliklerinin rüzgara negatif etkisi çok az olduğundan daha güçlü ve stabil rüzgar vardır. Bu yüzden denizüstü yüzer rüzgar türbinleri (YRT) en yüksek kapasite faktörüne erişebilmektedir. Diğer taraftan aerodinamik ve hidrodinamik kuvvetler YRT'nin 6 serbestlik derecesi ile birleşerek sistemi zamana duyarlı hale getirmektedir. Kuvvetler türbin üzerindeki ivmeyi indükleyerek sistemin salımına sebep olur. Türbinin maruz kaldığı bu salınım ,özellikle kanat-iz etkileşimi sırasında, kolay bir şekilde kararsız hale gelmektedir. Bu durum ekstrem koşullar altında daha ciddi yaşanmaktadır. Yunuslama hareketi gibi önemli ölçüde yaşanan açısal hareketler, sistemi türbin ve pervane arasında geçiş durumuna zorlamaktadır. Bu geçiş durumu mevcut sayısal araçlarla modellenememektedir. Bu yüzden YRT dinamiğini anlamak için tüm parametrelerin ele alındığı deneysel çalışma yapılması gerekmektedir.

Bu tezin ana amacı ekstrem rüzgar ve dalga koşulları altında YRT dinamik davranışını deneysel olarak incelemektir. TÜBİTAK (217M451) projesinin bir parçası olarak Northel POYRA P36/300 referans türbini ile spar-tip yüzer platformun 1/40 Froude ölçekli tasarımı ve üretimi çalışma arkadaşlarım tarafından gerçekleştirilmiştir. Bu tezde, deneysel çalışmalar İYTE İnşaat Mühendisliği Bölümünde bulunan dalga kanalı ve rüzgar nozul'u kullanılarak gerçekleştirilmiştir. Atmosferik sınır tabaka, IEC standardı ve Froude benzerliğine bağlı kalınarak ölçeklendirilmiştir. Rüzgar nozul'u ve dalga yapıcı'nın karakterize edilmesi doğru sonuç alınması konusunda büyük önem taşımaktadır. Deneyde kullanılan sensörler bu karakterizasyonu en doğru şekilde yapabilmek için kalibre edilmiştir. Gerçek boyutlardaki YRT sisteminin dinamiğinin anlaşılabilmesi için çeşitli koşullar altında testler uygulanmıştır.

# TABLE OF CONTENTS

LIST OF FIGURES ..... vii

LIST OF TABLES ..... xi

CHAPTER 1. INTRODUCTION ..... 1
1.1. Problem Definition ..... 6
1.2. Thesis Outline ..... 8

CHAPTER 2. THEORETICAL BACKGROUND ..... 10
2.1. Scaling Methodology ..... 10
2.2. Blade Element Momentum Theory ..... 12
2.2.1. Impact of Scaling on Aerodynamic Design ..... 18
2.3. Wave Theory ..... 20
2.3.1. Regular Wave ..... 21
2.3.2. Irregular Wave ..... 24
2.4. Aerodynamic Effects of Floating Dynamics ..... 25

CHAPTER 3. LITERATURE REVIEW ..... 28
3.1. Full Approach ..... 28
3.2. Simplified Approach ..... 31

CHAPTER 4. EXPERIMENTAL SETUP OF IZTECH FOR SPAR-TYPE FOWT 36
4.1. Model Setup ..... 36
4.1.1. Wave Flume ..... 37
4.1.2. Wind Nozzle ..... 37
4.1.3. Traverse Mechanism ..... 40
4.1.4. Model Turbine ..... 40
4.1.5. Model Spar-Type Floating Platform ..... 43
4.2. Instrumentation and The Tools of Experiments ..... 47
4.2.1. Hot-wire ..... 48
4.2.2. Strain gauge ..... 51

4.2.3. Image processing tool ..... 53

CHAPTER 5. RESULTS ..... 56
5.1. Atmospheric Boundary Layer Reproduction ..... 56
5.2. Dynamic Tests ..... 66
5.2.1. Free Decay Tests ..... 66
5.2.2. Only Wind Tests ..... 68
5.2.3. Wind and Regular Wave Tests ..... 69
5.2.4. Wind and Irregular Wave Tests ..... 84

CHAPTER 6. CONCLUSION, DISCUSSION AND FUTURE STUDIES ..... 86
6.1. Conclusions ..... 86
6.2. Discussion and Limitation of the Tests ..... 87
6.3. Recommendation for Future Studies ..... 88

REFERENCES ..... 89

APPENDICES
APPENDIX A. SIGNAL ANALYSIS ..... 96
APPENDIX B. CALIBRATION PROCESS OF HOT-WIRE ANEMOMETER ..... 99
APPENDIX C. DECOMPOSITION CODE OF COUPLED MOTION ..... 103
APPENDIX D. WIND TURBINE'S MOTOR ..... 106

# LIST OF FIGURES


**Figure** **Page**

Figure 1.1 Installed wind energy capacity ..... 1

Figure 1.2 Configurations of commonly used bottom-fixed offshore support structure ..... 3

Figure 1.3 Offshore wind atlas of Europe ..... 4

Figure 1.4 Configurations of the main concepts of floating wind turbine platform . 5

Figure 1.5 Degree of freedoms of Floating offshore wind turbine ..... 6

Figure 1.6 Illustration of loads on the floating offshore wind turbine ..... 7

Figure 1.7 Transient state between turbine and propeller state during pitch motion 8

Figure 2.1 1D momentum analysis in control volume with actuator disc ..... 14

Figure 2.2 Blade element theory ..... 17

Figure 2.3 Scheme of iterative solution technique of BEM ..... 19

Figure 2.4 Sketch of the regular wave and boundary conditions ..... 23

Figure 2.5 Possibility of unsteadiness along the blade of NREL 5 MW ..... 27

Figure 3.1 (a) surge and (b) pitch response of spar-buoy floating platform under an $H_s = 10.5m$ wave and three different wind conditions ..... 29

Figure 3.2 RAOs derived from white-noise wave excitation with $H_s = 7.1m$ without and with wind at 21.8 m/s; the colored box indicates the wave frequency range ..... 29

Figure 3.3 Left : Comparison of $C_t$ vs $TSR$ curves of geometric-match model, thrust-match model, and NREL 5 MW prototype. Right: Adjustment of pitch angle of blade to match $C_t$ with prototype ..... 30

Figure 3.4 Comparison of the resuls of experiment and simulation with and without wind: $H_s = 4.14m$, $T_p = 0.94s$, $V_{rated} = 1.3m/s$ ..... 31

Figure 3.5 RAO of experiment and simulation with and without wind ..... 32

Figure 3.6 RAO of experiment and simulation with and without wind : $H_s = 2.64m$, $T_p = 7.3s$ ..... 33

Figure 3.7 Platform motion spectra outputs of experiment under the wind-wave,only-wave,and only-wind conditions : $H_s = 3.6m$, $T_p = 10.2s$, $V = 11m/s$ . 33

**Figure** **Page**

Figure 3.8 Various concepts used in scaled model tests ..... 34
Figure 3.9 HexaFloat robot developed at Politecnico di Milano ..... 35
Figure 4.1 Top-sketch view of the test setup ..... 36
Figure 4.2 The dissipating beach with 1/5 gradient placed at the end of the channel ..... 38
Figure 4.3 Exploded view of screens, and a contracting nozzle ..... 39
Figure 4.4 Nozzle Designs ..... 39
Figure 4.5 Traverse Mechanism ..... 40
Figure 4.6 The airfoil section used in the model study ..... 42
Figure 4.7 Geometric model of blade design parameters ..... 42
Figure 4.8 Illustration of metacenter and metacentric height ..... 44
Figure 4.9 Schematic view of spar platform ..... 45
Figure 4.10 Measurement of center of gravity ..... 47
Figure 4.11 Ping-pong balls that placed on the tower ..... 48
Figure 4.12 Calibration nozzle ..... 49
Figure 4.13 Dwyer Model M1430 Microtector U-manometer ..... 50
Figure 4.14 Calibration process of hot-wire ..... 51
Figure 4.15 Calibration curve of hot-wire ..... 51
Figure 4.16 Strain gauge sensor on the tower bottom ..... 52
Figure 4.17 Calibration curve of Strain gauge ..... 53
Figure 4.18 View from Tracker program ..... 54
Figure 5.1 Froude-scaled logarithmic wind profile ..... 58
Figure 5.2 Measured wind profiles at x= 0.5D ..... 59
Figure 5.3 Measured wind profiles at x= 1D ..... 60
Figure 5.4 Measured wind profiles at x= 2D ..... 60
Figure 5.5 Measured wind profiles at x= 3D ..... 61
Figure 5.6 Measured wind points on y-z plane at x= 1D ..... 62
Figure 5.7 Wind profile at z=190 cm (o = Each measurement, black solid line = Average of measurements) ..... 62
Figure 5.8 Wind profile at z=225 cm (o = Each measurement, black solid line = Average of measurements) ..... 63

**Figure** **Page**

Figure 5.9 Wind profile at z=260 cm (o = Each measurement, black solid line = Average of measurements) ..... 63
Figure 5.10 Experiment wind profile ..... 64
Figure 5.11 Turbulence intensity of wind profile ..... 65
Figure 5.12 Wind speed difference over rotor swept area ..... 65
Figure 5.13 Free decay tests result in time domain ..... 67
Figure 5.14 Free decay tests result in frequency domain ..... 68
Figure 5.15 Only wind test, from left to right : 1. Initial position, 2. Position under the wind, 3. Enhanced position by mooring lines, 4. Rotor starts to rotation, 5. Transient state between starting of rotation and max rpm, 6. Position when the rotor at max rpm. ..... 69
Figure 5.16 Time series and PSD of measured data from wave gauge during various wave experiments ..... 71
Figure 5.17 Power spectral densities and time series of surge, heave, pitch motions of D-H2-T02-Test ..... 72
Figure 5.18 Power spectral densities and time series of surge, heave, pitch motions of D-H4-T02-Test ..... 73
Figure 5.19 Power spectral densities and time series of surge, heave, pitch motions of D-H6-T02-Test ..... 74
Figure 5.20 Power spectral densities and time series of surge, heave, pitch motions of D-H8-T02-Test ..... 75
Figure 5.21 Power spectral densities and time series of surge, heave, pitch motions of D-H10-T02-Test ..... 76
Figure 5.22 Power spectral densities and time series of surge, heave, pitch motions of D-H12-T02-Test ..... 77
Figure 5.23 Power spectral densities and time series of surge, heave, pitch motions of D-H2-T04-Test ..... 78
Figure 5.24 Power spectral densities and time series of surge, heave, pitch motions of D-H4-T04-Test ..... 79
Figure 5.25 Power spectral densities and time series of surge, heave, pitch motions of D-H6-T04-Test ..... 80

**Figure** **Page**

Figure 5.26 Power spectral densities and time series of surge, heave, pitch motions of D-H8-T04-Test ..... 81
Figure 5.27 Power spectral densities and time series of surge, heave, pitch motions of D-H10-T04-Test ..... 82
Figure 5.28 Power spectral densities and time series of surge, heave, pitch motions of D-H12-T04-Test ..... 83
Figure 5.29 Power spectral densities of surge, heave, pitch motions of Irregular-H8-T04-Test ..... 85
Figure A.1 Frequency spectrum of data according to time series ..... 96
Figure A.2 Two different amplitude scale for same data ..... 97
Figure A.3 Condition of aliasing occurrence in the frequency domain ..... 97
Figure A.4 The smeared amplitude in the entire frequency range which is known as the leakage problem ..... 98
Figure B.1 Schematic view of the IFA 300 Constant Temperature Anemometer System ..... 99
Figure B.2 Calibration - Probe Data screen of the IFA 300 ..... 101
Figure B.3 Communications screen of the IFA 300 ..... 101
Figure B.4 Block diagram of LabVIEW for the calibration ..... 102
Figure D.1 The Pololu Jrk G2 Configuration Utility user interface ..... 108

# LIST OF TABLES


**Table** **Page**

Table 2.1 Scale factor table of the parameters ..... 12

Table 2.2 Reynolds dissimilitude under Froude scaling ($\lambda = \frac{1}{40}$) ..... 19

Table 4.1 Operational parameters of the turbine ($\lambda = 1/40$) ..... 41

Table 4.2 Mass values of model turbine components ..... 43

Table 4.3 Structural and hydrostatic properties of spar platform ..... 45

Table 4.4 Scaled parameters of spar platform ..... 46

Table 4.5 Weights and CoG of the FOWT ..... 46

Table 5.1 Roughness values according to landscape type ..... 56

Table 5.2 Full-scaled version of wave parameters of experiment ..... 66

Table 5.3 Initial displacement and angular values which applied in free decay test . 67

Table 5.4 Parameters of regular wave of the tests ..... 70

Table D.1 Details of instruments of wind turbine motor's ..... 106

Table D.2 Preliminary study outputs of wind turbine motor's ..... 107

# CHAPTER 1

# INTRODUCTION

The global warming crisis brings unprecedented environmental impacts due to carbon emissions. Global average temperature has risen 1.5°C-2°C since the last century, this increases number of occurrences and the level of hot extremes, droughtiness and marine heatwaves, also reductions are observed in sea of North and South pole, (permafrost and snow cover) (23). To provide an effective solution, wind energy -in recent years offshore wind energy- has gained lots of attention from governments and industry.

In the preceding year, 93.1 GW of new wind energy capacity was installed worldwide with the largest increase, growing approximately 13%, in renewable energy generation. Furthermore, new-deployment of offshore wind turbine exceeds previous increments with 21.31 GW, reaching 55.67 GW capacity (24). Figure 1.1 shows the accumulation of installed wind energy capacity of last decade.

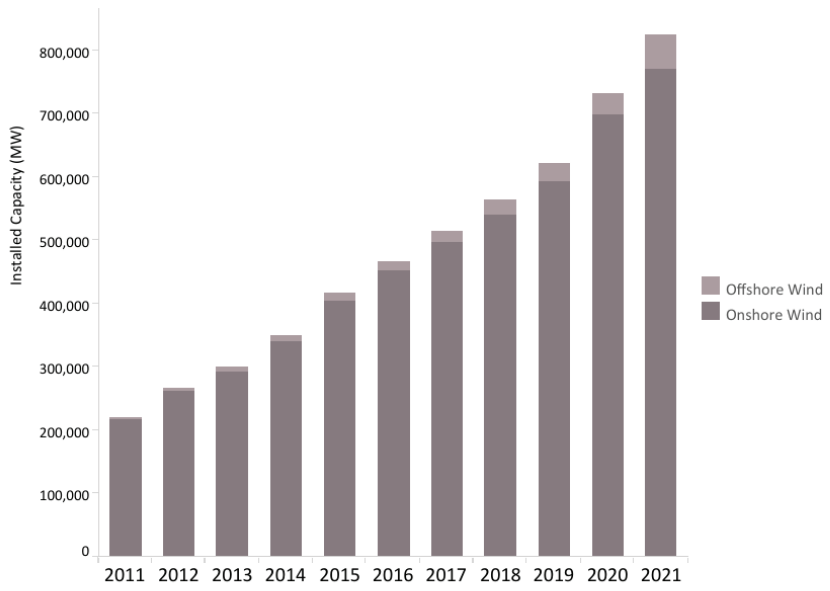


Figure 1.1. Installed wind energy capacity (1)

There are several reasons that makes the offshore wind energy ramp up significantly. Most of favorable onshore sites have already been used or are not economical anymore. For instance, the stakeholders in Northern Europe region tend to seize the opportunity of offshore wind energy in consequence of the lack of space. Moreover, there are countries that have mostly rugged, hilly, mountainous or forested terrains where the wind can not fully harvested (25).

Land-use regulations have been changing since the first installations (26). Size of the onshore wind turbines getting bigger year by year to efficiently harvest wind energy resource from the site, whereas transporting big components of the turbine is challenging in comparison to offshore and due to logistic issues wind turbine manufacturers try to achieve different technologies such as split blade, modular nacelle (27, 28). Additionally, noise produced by the turbine has become problematic for both society and governments. Therefore, less terrain are available for efficient wind power deployment.

According to recent statistics on the ordered wind turbines in 2021, the average nominal power of the onshore and offshore wind turbines were 4.9 MW and 11.2 MW, respectively (29). Meanwhile, dynamic surface of sea, without any obstacle, provides less turbulent and stronger wind which creates advantage in terms of power density. New installed bottom-fixed offshore wind turbines have a capacity factors ranging from 40-50%, while the onshore counterpart delivering capacity factor of roughly 40%. Furthermore, floating wind farm of Hywind Scotland reached highest average capacity factor of 57% with a record-breaking performance (23).

The Glasgow Climate Pact (COP 26) and the Russian invasion of Ukraine highlight the urgency of taking action about alternative energy sources; as a result, especially the European governments account to update their offshore wind energy capacity targets by 2030. The energy policy may be turned into a security policy in the near future (30).

The offshore turbine support structure technology in the wind energy industry comes from the oil and gas (O&G) industry (31). The support structures are mainly divided into bottom-fixed and floating platforms, which are derived from various mobile and fixed drilling platforms used in the O&G industry. The vast majority of current offshore wind power generation is provided by bottom-fixed wind turbines. Figure 1.2 shows five different bottom-fixed platforms commonly used in the offshore wind industry:

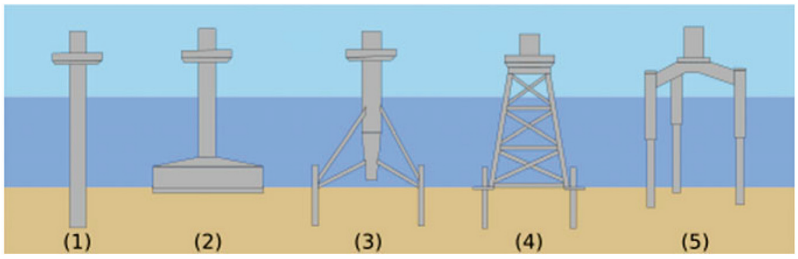


Figure 1.2. Configurations of commonly used bottom-fixed offshore support structure (2)

1. **Monopile:** The structure with cylindrical geometry, connected to the wind turbine tower with the help of a transition piece or directly, is called monopile. It is generally used at depths less than 20-30 m since its cost is susceptible to water depth.

2. **Gravity platform:** Gravity platforms provide stabilization with heavy concrete consisting of large dimensions on the seabed rather than large piles. It is generally used on a solid seabed less than 30 meters deep.

3. **Tripod:** The tripod support structure consists of a central cylindrical tower and steel frames connecting it to three piles. It has a combination of monopile and jacket structures.

4. **Jacket:** The jacket support structure consists of three or four main piles embedded in the seabed and braces connecting the steel legs extending from these piles in the form of a lattice.

5. **Tripile:** It is a 3-legged structure similar to a tripod. The central cylinder is shorter, with three legs fixed to the seabed. Tripod, jacket, and tripile structures are used at depths of 20-60 meters.

Bottom-fixed offshore wind turbines account for 99.8% of the installed capacity of the current offshore capacity. On the other hand, the installed capacity of the floating wind turbines has reached 121.4 MW, with a new installation of 57.1 MW in 2021 (32). Around 80% of the world's offshore wind energy resource potential is available where the sea is deeper than 50 m, and bottom-fixed offshore wind turbines are economically and technically unsuitable. European offshore wind energy potential is shown in Figure 1.3. For many countries in Europe, especially the Mediterranean countries, deep waters are

the norm on this country's coasts. Consequently, bottom-fixed wind turbines are neither option nor are potentially restricted (4).

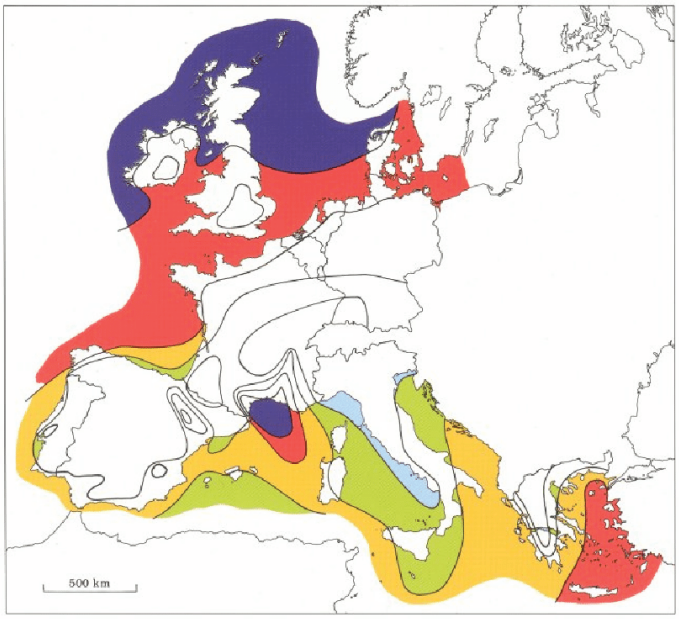


**Wind resources over open sea (more than 10 km offshore) for five standard heights**

| | 10 m | | 25 m | | 50 m | | 100 m | | 200 m | |
|---|---|---|---|---|---|---|---|---|---|---|
| | $m\,s^{-1}$ | $Wm^{-2}$ | $m\,s^{-1}$ | $Wm^{-2}$ | $m\,s^{-1}$ | $Wm^{-2}$ | $m\,s^{-1}$ | $Wm^{-2}$ | $m\,s^{-1}$ | $Wm^{-2}$ |
| | > 8.0 | > 600 | > 8.5 | > 700 | > 9.0 | > 800 | > 10.0 | > 1100 | > 11.0 | > 1500 |
| | 7.0-8.0 | 350-600 | 7.5-8.5 | 450-700 | 8.0-9.0 | 600-800 | 8.5-10.0 | 650-1100 | 9.5-11.0 | 900-1500 |
| | 6.0-7.0 | 250-300 | 6.5-7.5 | 300-450 | 7.0-8.0 | 400-600 | 7.5- 8.5 | 450- 650 | 8.0- 9.5 | 600- 900 |
| | 4.5-6.0 | 100-250 | 5.0-6.5 | 150-300 | 5.5-7.0 | 200-400 | 6.0- 7.5 | 250- 450 | 6.5- 8.0 | 300- 600 |
| | < 4.5 | < 100 | < 5.0 | < 150 | < 5.5 | < 200 | < 6.0 | < 250 | < 6.5 | < 300 |

Figure 1.3. Offshore wind atlas of Europe (3)

Floating offshore wind turbines (FOWTs) are a promising solution to harness this resource. Therefore, it is estimated that floating wind energy will constitute 6% of the total offshore wind energy capacity by 2030. For example, floating projects are increasing rapidly in countries such as France, the UK, the US, South Korea, and Japan, where sea conditions are suitable for the floating platform (32). Moreover, wind energy potentials are available far-offshore where deeper waters are encountered in Turkey.

Floating platforms are divided into three groups in terms of physical principle, shown in Figure 1.4. It provides stability for all systems (rotor-nacelle assembly, tower) under various conditions (2). An overview of the principles of floating platforms is given in the following part:

1. **Spar-type:** The Spar platform has a long cylindrical structure in the vertical direction. Since most of the system volume is submerged, the buoyancy force provides stability against external effects as a restoring force and returns the system to static

equilibrium. The lower center of gravity means, the more stable the system will be. The mooring lines mounted on the spar are embedded with the anchor to the seabed, keeping the platform stationary.

2. **Tension leg platform (TLP):** Tension leg platforms are stabilized by tensioned mooring lines and anchors well-positioned to the seabed. The taut mooring line allows for a shorter draft and lighter construction. The robustness of the mooring line and anchor is vital as they are subjected to higher loads. Tensioned lines pose a risk in the installation process and operational conditions.

3. **Barge :** Barge-type platform provides stabilization with a large waterplane area and shortest draft. Catenary lines are used to prevent it from getting dragged by the waves. However, the barge is more susceptible to the waves than other platforms. Therefore, semi-submersible is more widely used in sites. Semi-submersible, a combination of barge and spar, consists of three columns placed vertically into the water. It has a longer draft and higher weight than the barge. The columns at equal distances from each other reduce pitch and roll response compared to the barge (33).

Floating offshore wind energy is now at the beginning of the commercial phase. A comprehensive analysis was made in light of production, commercial innovation, and engineering studies carried out in recent years for cost reduction. As a result, it is predicted that the cost of offshore wind energy will decrease by 37-49% in 2050 (34). However, since it is not fully commercialized yet, there are many points that need to be developed and verified.

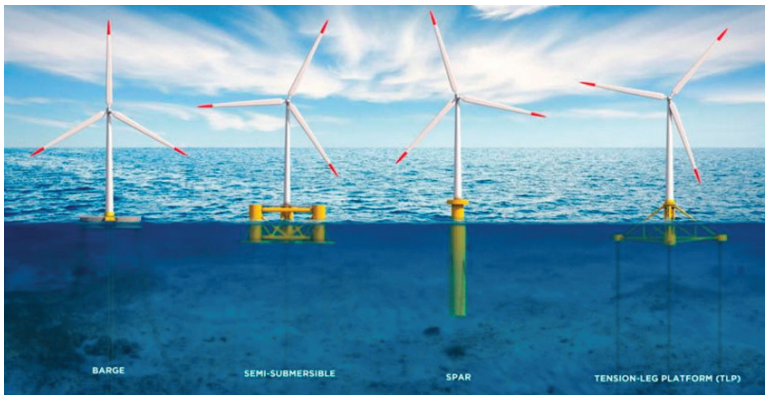


Figure 1.4. Configurations of the main concepts of floating wind turbine platform (4)

## 1.1. Problem Definition

FOWTs operate under the combined aerodynamic and hydrodynamic forces. Unlike onshore and bottom-fixed turbines, they have 6 degrees of freedom (DoF), three translational (surge, sway, heave), and three rotational (pitch, roll, sway). These DoFs, which cause a highly dynamic environment (35), are shown in Figure 1.5 .

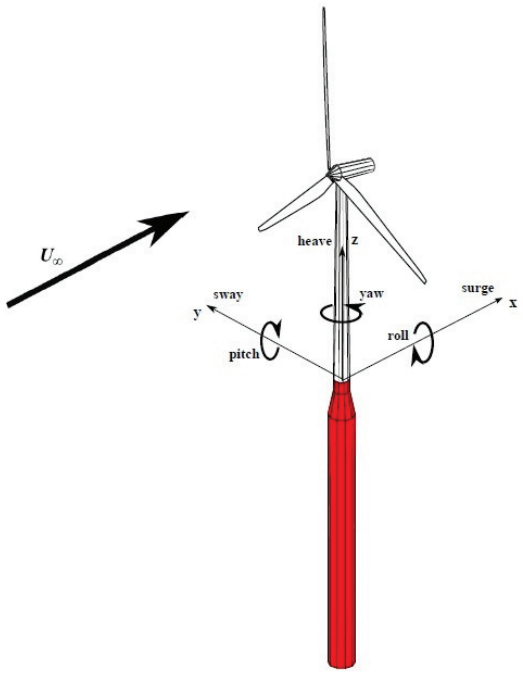


Figure 1.5. Degree of freedoms of Floating offshore wind turbine (5)

Various loads originating from wind, sea current and waves affect the FOWT system, as depicted in Figure 1.6. Hydrodynamic forces bring low frequency and high inertial loads to the tower and nacelle. These loads induce the acceleration of FOWT, and the system oscillates in different DoFs (7). The thrust force on the rotor causes an additional pitch angle which can be compensated by the pitch restoring stiffness of the floating platform and the mooring line. Depending on the platform type, this angle can be significant from an aerodynamic point of view. Dynamic inflow is the aerodynamic effect that occurs when the loads on the rotor change rapidly during blade pitching, wind gust, and platform motion. The rotor gradually reaches a new equilibrium state due to the new load condition, which causes an overshoot in the instant angle of attack and thrust force. There is

a delay in the load response of the blade element momentum (BEM) engineering model. Also, the model's assumption of momentum balance in its derivation causes deviation in the FOWT load analysis (10). In their work, Sebastian and Matha (36, 37) show that the BEM model cannot accurately model this lag response.

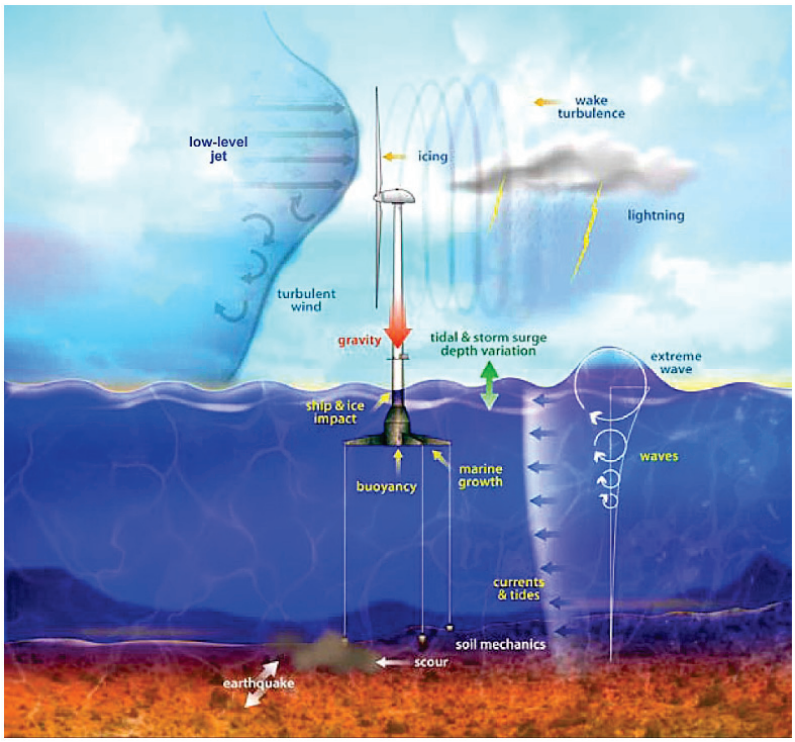


Figure 1.6. Illustration of loads on the floating offshore wind turbine (6)

The pitch and yaw motion of the floating platform affect the blades of the wind turbine through blade-wake interaction which causes transient flow on the rotor. The blades interact with their own wake whilst the rotor goes towards wake direction, and it creates highly unsteady aerodynamic around the rotor which called vortex ring state (7), illustrated in Figure 1.7. Furthermore, the platform's yaw and pitch rotational oscillations make the local wind speed on the rotor a motion-dependent variable and consequently invalidate the uniform wind speed assumption. Besides, it is difficult to model the non-axial flow on the rotor accurately (38).

In addition to the cases mentioned above, under the circumstances such as extreme waves and viscous forces, the effect of wave-current interaction on moored floating platform structures is challenging to model in numerical simulations. Therefore, scaled models and field experiments are essential in verifying nonlinear effects, extreme and complex

forces, and dynamic system behavior. Field experiments are not preferred because they require high cost, long installation, and validation period. Also, the damage it may take under extreme conditions poses a financial risk. On the other hand, scaled-down model experiments performed in a controlled laboratory environment are more time-efficient and have low risk (39).

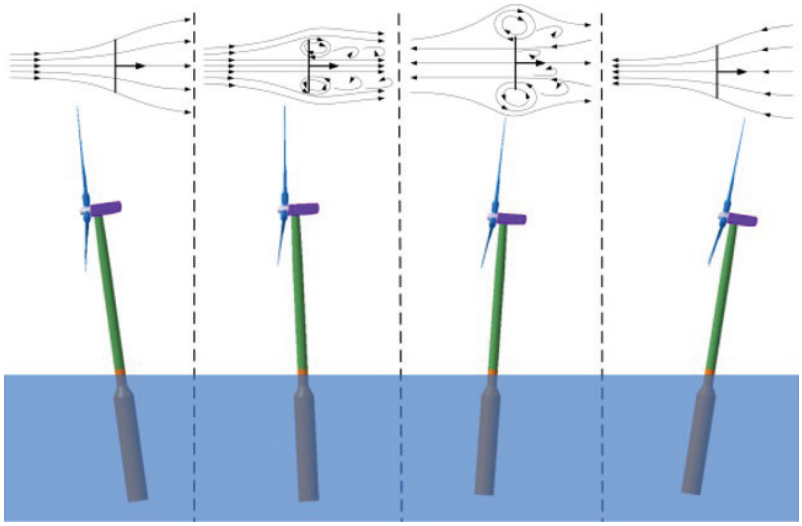

Figure 1.7. Transient state between turbine and propeller state during pitch motion (7)

Northel POYRA P36/300, suitable for the Izmir Institute of Technology wave flume conditions, is chosen as the reference turbine. The turbine has a rotor diameter of 36 meters and a nominal power of 320 kW. In order to examine the dynamic behavior of the wind turbine, mounted on the spar-type platform, under extreme wind and wave conditions, 1/40 scaling has been made based on the operational conditions at 20 m/s wind speed where the turbine operates. Unlike the multi-megawatt turbines, scaled-down testing is much more essential as the small-size FOWT system will exhibit more unstable behavior under the same extreme conditions.

## 1.2. Thesis Outline

This chapter explains the importance of floating wind turbines to achieve the carbon-zero goal by addressing several points. Besides the various advantages of the floating wind turbine, many technical points still need improvement. These problems are

addressed in the problem definition, and it is shown that scaled-down experiments can be employed as a solution to scrutinize these problems in the initial design of FOWT.

An appropriate scaling methodology has to be applied to accurately model the dynamic behavior of the floating wind turbine system under various fluid-based loads. The second chapter will present the necessary theoretical background to design a scaled-down wind turbine. In addition, the relationship between Reynolds and Froude, two dimensionless numbers used in fluids scaling, will be given. The effects of Reynolds number under Froude scale conditions will be discussed. Blade element momentum used in wind turbine rotor design will be explained, and the hydrodynamic forces acting on the floating wind turbine are briefly explained. Besides, the theoretical background of regular and irregular waves used in the experimental tests will be described with the linear wave theory. Last but not least, the aerodynamic effects of floating dynamics on the wind turbine will be explained and clarified why the scaled model test should be applied for the FOWT.

In chapter 3, the literature will be reviewed. The scaled model wind/wave basin tests will be divided into two groups and investigated. With the results of the first tests, various test methods will be presented to improve the performance of the scaled model.

In the 4th chapter, information about the experimental setup in the IZTECH Civil Engineering hydraulic laboratory and the scaling studies of the FOWT system will be explained, and the sensors employed during the experiment will be introduced.

In the Results chapter, the atmospheric boundary layer will be scaled according to the IEC standard and Froude-scaling. In order to get the desired wind characteristic from the wind nozzle, the comprehensive test study will be explained, and the results will be given. First, the natural frequency in each decay test for the individual degree of freedom will be calculated as a result of free decay tests. Then, the wave flume tests with and without wind conditions with the determined wave parameters will be introduced. Finally, the time-series and power spectral densities of each degree of freedom will be given.

Finally, in chapter 6, the experiment results will be scrutinized, the experimental system will be evaluated, and suggestions will be made for future studies.

# CHAPTER 2

# THEORETICAL BACKGROUND

Most physical systems can be investigated with a small-scale model that can achieve the same behavior as a full-scale prototype. A scaling law is required to simulate the entire physical concept behind the system adequately.

## 2.1. Scaling Methodology

In fluid mechanics studies, there are three basic scaling laws. First, geometric similarity: model and prototype geometry must have the same shape to achieve geometric similarity. All structure lengths used in the model experiment must be reduced by the same ratio as the prototype. The flow field must also provide similar requirements. The second is kinematic similitude: the ratio of velocities and accelerations between the model and the prototype must be the same. With a given geometric similarity, it is also necessary to satisfy the dynamic similarity, the third similarity, in order to provide kinematic similarity or similarity of motion. This is because five different forces act on the flow field around the structure, creating the fluid-structure interaction. These are surface tension, viscosity, gravity, pressure, and elasticity. In order to provide dynamic similarity, the similarity of forces, the ratio between the model and the prototype must be constant (40).

The system becomes too complicated to satisfy the scaling law if all parameters are included. Therefore, complete similarity cannot be achieved except for scaling ratios very close to one (40). For large offshore structures, surface tension and elasticity are often neglected. Buckingham's pi theorem, a parametric approach, establishes the relationship between the model and the prototype by deriving a set of dimensionless quantities from essential variables that affect the system dynamics. The Reynolds number, which represents the relationship between inertial and viscous forces, is widely used in wind tunnel tests for proper rotor scaling in wind turbines. On the other hand, the Froude number, which represents the ratio of inertial forces to gravitational forces, is employed to ensure the similarity of dominant hydrodynamic forces in floating structure tests. There-

fore, scaling laws can be satisfied by keeping Froude and Reynolds numbers constant. Reynolds number is defined in equation 2.1:

$$Re = \frac{\rho * V * L}{\mu} \tag{2.1}$$

where $\rho$ is the density of the fluid in which the structure is located, $V$ is velocity coming to the structure, characteristic length of the structure is $L$, and $\mu$ is dynamic viscosity of the fluid. If the relationship between the prototype and the scaled-down model is re-defined, after applying the geometric scale factor, using Reynolds number similarity:

$$V_M * L_M = V_M * L_P * \lambda = V_P * L_P \tag{2.2}$$

$$\lambda = \frac{L_M}{L_P} \tag{2.3}$$

Dynamic viscosity and density are not taken into account since it is the same fluid. If the equation is simplified concerning velocity:

$$V_M = \frac{V_P}{\lambda} \tag{2.4}$$

The $\lambda$ was chosen 1/40 for our scaled-down model. Then, 800 m/s is obtained from the above equation for Reynolds similitude. The model's speed causes supersonic flow environments, and correct flow modeling cannot be obtained. Since Reynolds similitude could not be achieved, Froude scaling was applied to create the model environment to represent the driver loads accurately. The Froude number, a measurement of bulk flow characteristics like the wave in free surface flows, is defined as follows:

$$Fr = \frac{V}{\sqrt{g * L}} \tag{2.5}$$

where g is the gravitational constant, L is hydraulic depth, and V is water velocity. The same procedure as the previous step is followed to obtain the wind speed employed on the FOWT.

$$\frac{V_M}{\sqrt{g * L_M}} = \frac{V_M}{\sqrt{g * L_P * \lambda}} = \frac{V_P}{\sqrt{g * L_P}} \tag{2.6}$$

If the equation is simplified for velocity:

$$V_M = V_P * \sqrt{\lambda} \tag{2.7}$$

Considering Equations 2.4 and 2.7, it can also be seen that it is not possible to utilize Froude and Reynolds numbers simultaneously to achieve similarity. The Froude-scaled velocity equation gives the time scale of $\lambda^{0.5}$ through unit analysis. For accurate dynamic

modeling, the structural and displaced water mass ratios between the prototype and the model should be preserved:

$$\frac{Mass_M}{\rho * Volume_M} = \frac{Mass_P}{\rho * Volume_P} \tag{2.8}$$

Since the volume scale is $\lambda^3$ from geometric scaling, this yields:

$$Mass_M = Mass_P * \lambda^3 \tag{2.9}$$

Result of the scaling between parameters defined by fundamental quantities, e.g., L, M, and T (mass, length, time). The scaling factor of each parameter is determined by making a unit analysis. Table 2.1 shows the scaling factor of essential parameters in the FOWT experiment.

Table 2.1. Scale factor table of the parameters

| **Parameters** | **Unit** | **Scaling Factor** |
|---|---|---|
| Length | $L$ | $\lambda$ |
| Mass | $M$ | $\lambda^3$ |
| Time | $T$ | $\lambda^{0.5}$ |
| Volume | $L^3$ | $\lambda^3$ |
| Density | $ML^{-3}$ | 1 |
| Velocity | $LT^{-1}$ | $\lambda^{0.5}$ |
| Acceleration | $LT^{-2}$ | 1 |
| Frequency | $T^{-1}$ | $\lambda^{-0.5}$ |
| Force | $MLT^{-2}$ | $\lambda^3$ |
| Moment | $ML^2T^{-2}$ | $\lambda^4$ |
| Power | $ML^2T^{-3}$ | $\lambda^{3.5}$ |

Froude-scaling in the model FOWT gives lower wind speeds than the prototype. As a result, the Reynolds number is significantly reduced with scaled-down characteristic length and wind speed. Therefore, how the effects of the rotor's aerodynamic performances are modelled will be explained in 2.2.1.

## 2.2. Blade Element Momentum Theory

Fundamentally, a wind turbine converts the kinetic energy from the wind to mechanical energy with the rotor, transfers the mechanical power to the generator with the

gearbox in the drivetrain, and converts it into electrical energy. The process of harvesting kinetic energy in the wind to produce mechanical energy at the rotor can be explained through momentum theory, which is a tool for understanding wind turbine aerodynamics (41). Conservation of mass, energy, and momentum laws are defined in a control volume by making steady, axisymmetric, inviscid, incompressible flow assumptions,

$$\oint_{CV} \rho \mathbf{V}.d\mathbf{A} = 0 \tag{2.10}$$

$$\oint_{CV} u\rho \mathbf{V}.d\mathbf{A} = T - \oint_{CV} pd\mathbf{A}.e_x \tag{2.11}$$

$$\oint_{CV} ru_\theta \rho \mathbf{V}.d\mathbf{A} = Q \tag{2.12}$$

$$\oint_{CV} \left[\frac{p}{\rho} + \frac{1}{2}||\mathbf{V}||^2\right] \rho \mathbf{V}.d\mathbf{A} = P \tag{2.13}$$

where $u, v, u_\theta$, axial, radial, and azimuthal velocity components of $\mathbf{V}$, respectively. $A$ represents area vector normal to the control volume, T is the thrust force acting on the rotor in the axial direction, p is the pressure. Torque and power of the rotor are represented with Q and P, respectively. The main dimensionless parameters used in characterizing the aerodynamic performance of the wind turbine are given below:

$$\text{Thrust coefficient :} \qquad C_T = \frac{T}{\frac{1}{2}\rho A U_0^2} \tag{2.14}$$

$$\text{Power coefficient :} \qquad C_P = \frac{P}{\frac{1}{2}\rho A U_0^3} \tag{2.15}$$

$$\text{Tip speed ratio :} \qquad \lambda = \frac{\Omega R}{U_0} \tag{2.16}$$

where $\Omega$ is the rotor's angular velocity, $A$ is the rotor's swept area, $R$ is the swept area's radius, and $U_0$ is the wind speed.

The rotor can be modeled using an ideal actuator disk, where there is a sudden pressure drop as the flow passes over it, while the wind speed decreases without discontinuity. The high pressure in front of the actuator disc is named $p^+$, while the low pressure just behind it is named $p^-$. The thrust force can be obtained by multiplying the pressure difference and area,

$$\Delta T = (p^+ - p^-).\Delta A \tag{2.17}$$

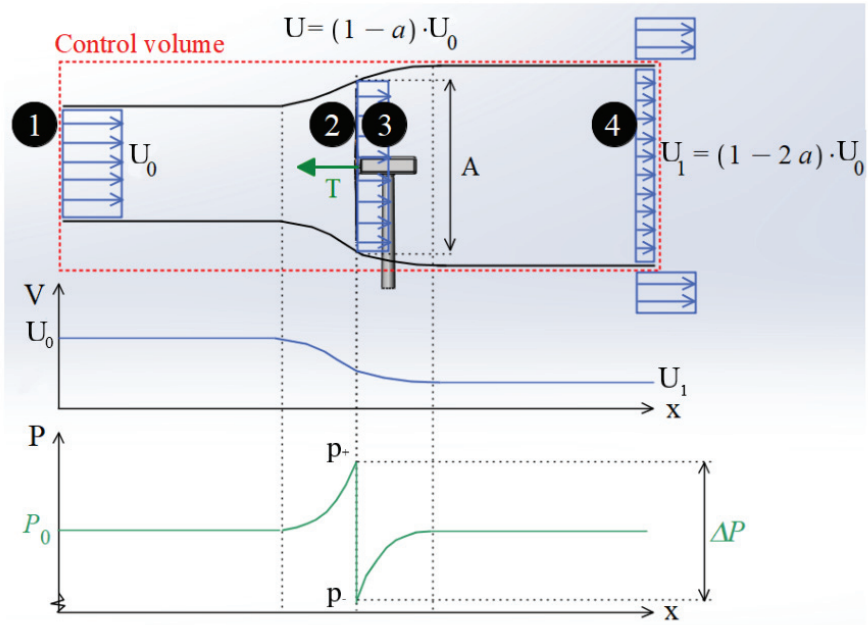


Figure 2.1. 1D momentum analysis in control volume with actuator disc (8)

According to the continuity equation ( eq. 2.10), each cross-section must have the same mass flow rate:

$$\dot{m} = \int \rho V dA = \rho U_0 A_0 = \rho U A = \rho U_1 A_1 \tag{2.18}$$

The following equation is obtained for thrust, where the axial momentum balance in Equation 2.11 is applied to the control volume:

$$T = \dot{m}(U_0 - U_1) = \rho U A(U_0 - U_1) \tag{2.19}$$

The assumptions made for the axial momentum allow the Bernoulli equation to be established between far upstream (1) and just in front of the rotor (2), and just behind the rotor (3) and far downstream (4), as seen in Figure 2.1,

$$p_0 + \frac{1}{2}\rho U_0^2 = p^+ + \frac{1}{2}\rho U^2 \tag{2.20}$$

$$p_1 + \frac{1}{2}\rho U_1^2 = p^- + \frac{1}{2}\rho U^2 \tag{2.21}$$

With the knowledge of the equivalency of pressures in the far upstream and downstream ($p_0 = p_1$), these two Bernoulli equations (2.20-2.21) are subtracted from each other:

$$(p^+ - p^-) = \Delta P = \frac{1}{2}\rho(U_0^2 - U_1^2) \tag{2.22}$$

If the thrust in Equation 2.17 is combined with the Equations 2.19-2.22 and simplified:

$$U = \frac{1}{2}(U_0 + U_1) \tag{2.23}$$

An axial induction factor (a) is introduced to appropriately define both the velocity on the rotor and the velocity downstream with the freestream velocity (42). The axial induction factor describes how much kinetic energy of air the rotor absorbs.

$$a = \frac{U_0 - U}{U_0} \tag{2.24}$$

$$U = (1 - a).U_0 \tag{2.25}$$

$$U_1 = (1 - 2a).U_0 \tag{2.26}$$

Thrust and power extraction can be rewritten in terms of axial induction:

$$T = 2\rho A U_0^2 a(1 - a) \tag{2.27}$$

$$P = U.T = 2\rho A U_0^3 a(1 - a)^2 \tag{2.28}$$

Considering the equations 2.14-2.15, the thrust and power coefficients can also be rewritten, respectively:

$$C_T = 4a(1 - a) \tag{2.29}$$

$$C_P = 4a(1 - a)^2 \tag{2.30}$$

In axial momentum theory, radial and azimuthal variations of the flow are not taken into account since the actuator disc that gives instant pressure drop is replaced, and rotational flow is ignored. On the other hand, in general momentum theory, where radial and azimuthal variations are included (9). The angular velocity ($\Omega$) of the blade, $u_\theta$ formed just behind the blade due to blade rotation, and the radial distance of the blade on the rotor are considered. The Bernoulli equation of both sides of the rotor is rewritten with the new parameters:

$$p^+ + \frac{1}{2}\rho(u^2 + v^2 + (\Omega r)^2) = p^- + \frac{1}{2}\rho(u^2 + v^2 + (\Omega r - u_\theta)^2) \tag{2.31}$$

When the above equation is simplified for instant pressure drop:

$$\Delta P = -\rho \Omega r u_\theta + \frac{1}{2}\rho u_\theta^2 \tag{2.32}$$

The local area is separated into annular segments in the radial direction ($\Delta A = 2\pi r \Delta r$). According to the axial momentum equation (eq. 2.11), the new thrust equation is given as follows:

$$\Delta T = (p^{+} - p^{-})\Delta A = \rho U(U_0 - U_1)\Delta A - (p_1 - p_0)\Delta A_1 + \Delta Y \tag{2.33}$$

where $\Delta A_1$ is the cross-sectional area in downstream volume and $\Delta Y = \int (p - p_0) dA.e_x$ is axial force contribution from lateral pressure. If Equations 2.32 and 2.33 are combined:

$$\rho U(U_0 - U_1) - (p_1 - p_0)\frac{\Delta A_1}{\Delta A} + \frac{\Delta Y}{\Delta A} = -\rho \Omega r u_\theta + \frac{1}{2}\rho u_\theta^2 \tag{2.34}$$

When induction factors are introduced, and the last equation is written in terms of these factors,

$$a = 1 - \frac{U}{U_0}, \qquad b = 1 - \frac{U_1}{U_0}, \qquad a^{'} = -\frac{u_\theta}{2r\Omega}, \tag{2.35}$$

$$2b(1-a) = \frac{p_1 - p_0}{\frac{1}{2}\rho U_0^2}.\frac{1-a}{1-b} + \frac{1}{\frac{1}{2}\rho U_0^2}.\frac{\Delta Y}{\Delta A} + 4\lambda^2 x^2 a^{'}(1 + a^{'}) \tag{2.36}$$

where $x = \frac{r}{R}$, Equation 2.36 is the most comprehensive version of the momentum equation as it includes all parameters. However, since it contains many unknowns, assumptions have been applied to solve this equation. For example, the contribution from the lateral pressure is neglected because it is both a small and a problematic effect to calculate. Glauert model is the most widely used model rotor design and analysis (43). Glauert has simplified the equation by making the assumptions given below,

$$p_0 \cong p_1, \qquad u_{\theta_1}^2 \cong u_\theta^2, \qquad b \cong 2a \tag{2.37}$$

Equation 2.36 is simplified with these assumptions and gives the relationship between axial and tangential induction factors depending on the radial position:

$$a(1-a) = \lambda^2 x^2 a^{'}(1 + a^{'}) \tag{2.38}$$

Under optimum operating conditions of the rotor, it is possible to set the closed system equations with this equation, allowing the rotor to reach its upper-performance limits. Besides, its combination with blade element theory forms the pillar of blade element momentum (BEM) theory (41).

In BEM theory (43), loads are calculated by two independent methods. 1-D momentum theory is employed with the 2-dimensional airfoil data of the local blade element. Consider the flow on the rotor with constant wind speed and direction. The flow around cross-section of the blade is vectorial sum of the free stream wind speed, the angular velocity of the rotor, and the induced velocities due to the presence of the blade. As shown

in Figure 2.2b, the angle between the incoming wind and the airfoil chord is called the local angle of attack. With the given Reynolds number, type of airfoil, and angle of attack, the lift and drag coefficients on each airfoil can be calculated, as seen in Figure 2.2a. With this airfoil characteristic, loads along the blade are calculated utilizing momentum theory, and induced velocities are determined.

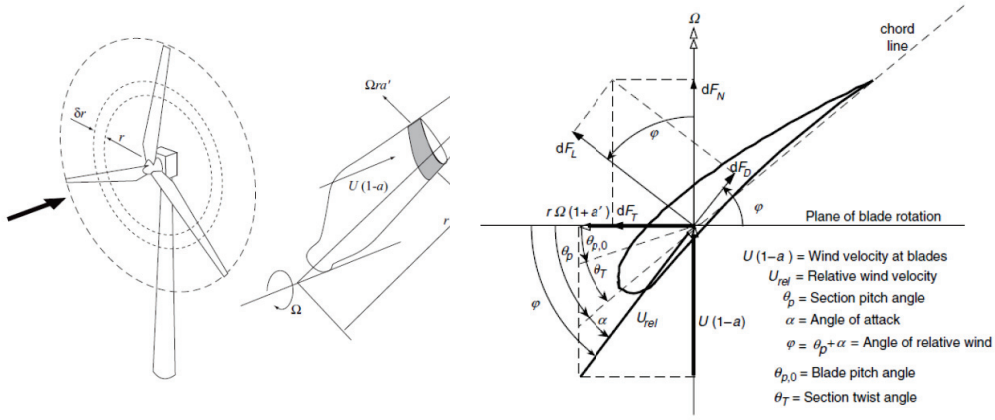


(a) Discretization of blade (44)

(b) Force diagram of blade element (9)

Figure 2.2. Blade element theory

The axial load and torque are defined as follows:

$$\frac{dT}{dr} = N_b F_n = \frac{1}{2}\rho c N_b U_{rel}^2 . C_n \tag{2.39}$$

$$\frac{dQ}{dr} = N_b r F_t = \frac{1}{2}\rho c N_b r U_{rel}^2 . C_t \tag{2.40}$$

where $N_b$ is the blade number, $V_{rel}$ is relative velocity, and $c$ is chord of the blade. $F_n$ and $F_t$ represent the axial and tangential loads, respectively. These forces can be defined with non-dimensional coefficients:

$$C_n = \frac{F_n}{\frac{1}{2}\rho c U_{rel}^2} \qquad \text{and} \qquad C_t = \frac{F_t}{\frac{1}{2}\rho c U_{rel}^2} \tag{2.41}$$

These coefficients constitute a combination of the airfoil's lift and drag coefficients depending on the flow angle ($\phi$),

$$C_n = C_l \cos\phi + C_d \sin\phi \qquad \text{and} \qquad C_t = C_l \sin\phi - C_d \cos\phi \tag{2.42}$$

The $C_l$ and $C_d$ coefficients, which depend on the geometry of the airfoil, are functions of Reynolds and angle of attack. Due to the material strength of the rotor, it goes from thick airfoil to thin from hub to tip. Since there is less angular velocity in the inner part of the blade, the incoming flow comes with a higher angle of attack. The blade has a locally varying twist angle to achieve maximum efficiency at the optimum angle of attack during the operation. As a result, the inner part of the blade has higher twist angle than the outer part of the blade. The sum of the twist angle and the pitch angle is defined by $\theta_p$, then the local angle of attack $\alpha = \phi - \theta_p$. The velocity triangle formed on the airfoil is defined as follows,

$$\cos\phi = \frac{\Omega r(1+a^{'})}{U_{rel}} \qquad \text{and} \qquad \sin\phi = \frac{U_0(1-a)}{U_{rel}} \tag{2.43}$$

When $U_{rel}^2$ is found from the above relationship and the thrust and torque equation is rewritten according to that,

$$U_{rel}^2 = \frac{U_0^2(1-a)^2}{\sin^2\phi} = \frac{U_0(1-a)\Omega r(1+a^{'})}{\sin\phi\cos\phi} \tag{2.44}$$

$$\frac{dT}{dr} = \frac{\rho N_b c U_0^2(1-a)^2}{2\sin^2\phi}.C_n \tag{2.45}$$

$$\frac{dQ}{dr} = \frac{\rho N_b c U_0(1-a)\Omega r^2(1+a^{'})}{2\sin\phi\cos\phi}.C_t \tag{2.46}$$

If the axial and angular momentum conservation equations are obtained in terms of induction factors; thrust, and torque:

$$\frac{dT}{dr} = \rho(U_0 - U_1)2\pi r U = 4\pi\rho r U_0^2 a(1-a) \tag{2.47}$$

$$\frac{dQ}{dr} = \rho r u_\theta 2\pi r U = 4\pi\rho r^3\Omega U_0 a^{'}(1-a) \tag{2.48}$$

Recall that $u_\theta = 2\Omega r a^{'}$. After combining the final thrust and torque equations and some algebra, the result is given:

$$a = \frac{1}{\frac{4\sin^2\phi}{\sigma C_n} + 1} \qquad \text{and} \qquad a^{'} = \frac{1}{\frac{4\sin\phi\cos\phi}{\sigma C_t} - 1} \tag{2.49}$$

The rotor's area, where it encounters the wind, is smaller than the actuator disc. Therefore, it is defined as $\sigma = N_b c/2\pi r$, which is called solidity. Although equations of 2.49 are explicit, the right side of the equations depends on two different variables (angle of flow and airfoil geometry). Therefore, the total of system equations is non-linear and implicit. These system equations are solved using non-linear solution techniques or the simple iterative loop technique seen in Figure 2.3.

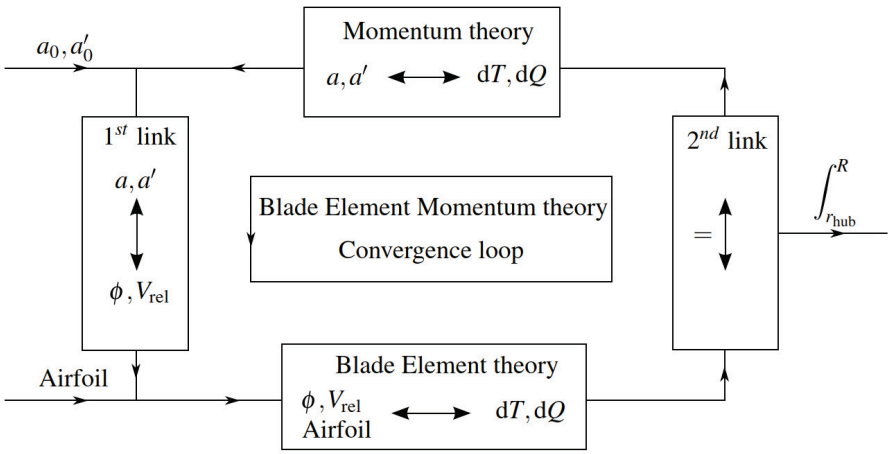


Figure 2.3. Scheme of iterative solution technique of BEM (9)

### 2.2.1. Impact of Scaling on Aerodynamic Design

In order to achieve aerodynamic similarity in a scaled-down model rotor, three scaling laws must be met. The kinematic similarity between the model and the prototype can be obtained by keeping the tip speed ratio ($TSR = \frac{\Omega R}{U_0}$) constant (45). Additionally, maintaining the scaled mass in the model rotor with the same center of gravity, which will provide the same mass distribution as the prototype, is very important to correctly match system dynamics, i.e., gyroscopic effect (46).

To consistently maintain kinematic similarity, maintaining dynamic similarity is needed for the loads on the rotor. As explained in the previous section, the lift and drag forces on the blade are the functions of the Reynolds number. Table 2.2 shows that using Froude scaling leads to a significant decrease in the Reynolds number.

Table 2.2. Reynolds dissimilitude under Froude scaling ($\lambda = \frac{1}{40}$)

| **Quantity** | **Prototype** | **Scaling Factor** | **Model** |
|---|---|---|---|
| Reynolds | $6.4 * 10^4$ | $\lambda^{\frac{3}{2}}$ | 252.98 |

At low Reynolds numbers, especially on the low-pressure side of the airfoil, the flow displacement thickness is much larger. As a result, the flow separates in the laminar

region close to the airfoil's leading edge, disrupting the optimal pressure distribution. This effect causes immense changes in the lift ($C_l$) and drag ($C_d$) coefficients of the airfoil sections.

One solution to this problem is to modify the blade geometry according to the low Reynolds number (12). However, the scenario where both thrust and power coefficients match perfectly is not possible. Therefore, prioritization is required between thrust and torque force, which is a function of power. Since the reaction force on the mooring lines connected to the floating platform due to the thrust force is much higher than the overturning due to torque, keeping the scaled thrust force has been given priority (47). Furthermore, there is a significant decrease in $C_l$ and an increase in $C_d$ at low Reynolds numbers. Since the lift coefficient contributes positively to the torque force (eq. 2.42), it is challenging to obtain scaled torque. In conclusion, even if the model thrust force is preserved, the dynamic similarity is not fully achieved since all aerodynamic forces cannot be scaled correctly (6). This imperfection in scaling is called scaling-effect or Reynolds-effect.

## 2.3. Wave Theory

This section considers linear wave theory that creates hydrodynamic loads acting on the FOWT. These are hydrostatic loads, loads from incident waves, radiation loads, and diffraction loads. Linear wave theory is defined by potential flow using incompressible, inviscid, and irrotational assumptions (48).

- Radiation load : The force generated on the floating platform as it oscillates in the sea in various modes without any incident wave. Moreover, it causes waves that reflect off the floating platform.

- Diffraction load : The load distribution occurs on the surface due to the incident wave, while the floating platform is stationary without movement.

- Hydrostatic load : The static load occurs perpendicular to the surface due to the pressure of the surrounding water on the surface of the submerged structure. The load on the structure is proportional to its draft.

$$F_i^{Hydro} = F_i^{Waves} + \rho g V_0 \delta_{i3} - C_{ij}^{Hydrostatic} q_j - \int_0^t K_{ij}(t-\tau)\dot{q}_j(\tau)d\tau \tag{2.50}$$

The combination of linear hydrodynamic forces is represented above as $F_{hydro}$. The fourth term on the right-hand side is the integral of the additional loads from wave radiation that are not accounted for in $A_{ij}$. $A_{ij}$ represents the impulsive hydrodynamic added mass; detailed information is available in Sarpkaya's "Wave Forces on Offshore Structures" book (48). The second and third terms on the right-hand side represent hydrostatic loads by the combination of buoyancy force, and center of buoyancy (CoB) change from the movement of the floating platform. The first term on the right-hand side is the total excitation load on the floating platform due to the incident wave and is closely related to the wave elevation (49). The following part will explain wave elevation in irregular and regular waves.

### 2.3.1. Regular Wave

The Navier-Stokes equations can describe all flows in nature. However, these equations are difficult to solve and often need computational calculations such as computational fluid dynamics (CFD) tools. Reynolds stresses from the viscid forces formed in the boundary layer are the main problem for these equations. While describing ocean waves in the study (50), friction's effects are ignored, simplified the Navier-Stokes equation, and obtained Euler equations. As a result of neglecting viscid forces, all external forces are conservative. Kelvin's theorem states that the flow will remain irrotational if it does not have initial vorticity ($\omega$),

$$\omega = curl(\vec{u}) = \nabla \times \vec{u} = \begin{bmatrix} \frac{\partial w}{\partial y} - \frac{\partial v}{\partial z} \\ \frac{\partial u}{\partial z} - \frac{\partial w}{\partial x} \\ \frac{\partial v}{\partial x} - \frac{\partial u}{\partial y} \end{bmatrix} = 0 \tag{2.51}$$

where $\vec{u} = [u, v, w]^T$ . Since the flow is irrotational, velocity potential ($\Phi(x, y, z)$) can be defined everywhere in the flow field as:

$$\vec{u} = [u, v, w]^T = grad(\Phi) = \nabla\Phi = \left[\frac{\partial \Phi}{\partial x}, \frac{\partial \Phi}{\partial y}, \frac{\partial \Phi}{\partial z}\right]^T \tag{2.52}$$

When the equations 2.51-2.52 are combined with Euler equations, the general version of Bernoulli's equation is obtained as follows,

$$gz + \frac{p}{\rho_w} + \frac{1}{2}\left(\left(\frac{\partial \Phi}{\partial x}\right)^2 + \left(\frac{\partial \Phi}{\partial y}\right)^2 + \left(\frac{\partial \Phi}{\partial z}\right)^2\right) + \frac{\partial \Phi}{\partial t} = 0 \tag{2.53}$$

where g is the gravitational acceleration, $\rho$ is the density of the water, and p is the pressure. In order to obtain pressure, the equation can be rewritten below:

$$p = -\rho_w g z - \underbrace{\frac{1}{2}\rho_w \left( \left(\frac{\partial \Phi}{\partial x}\right)^2 + \left(\frac{\partial \Phi}{\partial y}\right)^2 + \left(\frac{\partial \Phi}{\partial z}\right)^2 \right)}_{\text{=0 in linearized version}} - \rho_w \frac{\partial \Phi}{\partial t} \tag{2.54}$$

In the assumption of incompressibility, the continuity equation must be satisfied, which can also be preferred as the Laplace equation:

$$div(\vec{u}) = \nabla.\vec{u} = \frac{\partial u}{\partial x} + \frac{\partial v}{\partial y} + \frac{\partial w}{\partial z} = \nabla^2 \Phi = \frac{\partial^2 \Phi}{\partial x^2} + \frac{\partial^2 \Phi}{\partial y^2} + \frac{\partial^2 \Phi}{\partial z^2} = 0 \tag{2.55}$$

These equations complement potential flow theory. When appropriate boundary conditions are applied, the differential equation in equation 2.55 can be solved and $\phi$ can be found. The pressure can be calculated when the velocity potential ($\phi$) is substituted in equation 2.54.

Boundary conditions must be applied at an exact surface elevation, $z = \eta(x, y, z, t)$. Since there is no flow towards the bottom of the seabed with depth h, the kinematic bottom boundary condition is defined as:

$$\frac{\partial \Phi}{\partial z} = 0 \quad \text{for} \quad z = -h \tag{2.56}$$

The particle on the free surface has to remain there. In other words, the difference in material derivation between the free surface elevation ($\eta(x, y, z, t)$) and the instantaneous position ($z$) of the particle must cancel each other out. This state creates the second boundary condition, the kinematic free surface,

$$\frac{D}{Dt}(z - \eta) = \frac{\partial \Phi}{\partial z} - \frac{\partial \eta}{\partial t} - \cancelto{0}{\frac{\partial \Phi}{\partial x}\frac{\partial \eta}{\partial x}} - \cancelto{0}{\frac{\partial \Phi}{\partial y}\frac{\partial \eta}{\partial y}} - \cancelto{0}{\frac{\partial \Phi}{\partial z}\frac{\partial \eta}{\partial z}} = 0 \quad \text{for} \quad z = 0 \tag{2.57}$$

Higher-order terms can be ignored since the free surface elevation derivative is small if one assumes small wave amplitudes. The dynamic boundary condition expresses that the free surface's pressure must equal the atmospheric pressure ($p = 0$). The Bernoulli's equation is rewritten according to this expression:

$$gz - \cancelto{0}{\frac{1}{2}\left( \left(\frac{\partial \Phi}{\partial x}\right)^2 + \left(\frac{\partial \Phi}{\partial y}\right)^2 + \left(\frac{\partial \Phi}{\partial z}\right)^2 \right)} - \frac{\partial \Phi}{\partial t} = \quad \text{for} \quad z = 0 \tag{2.58}$$

Since $z = \eta$, the equations 2.57-2.58 can be combined to form a single boundary condition,

$$\frac{\partial \Phi}{\partial z} + \frac{1}{g}\frac{\partial^2 \Phi}{\partial t^2} = 0 \quad \text{for} \quad z = 0 \tag{2.59}$$

Lastly, a periodic boundary condition is defined in regular waves with constant form and period. It states that the flow at two different points with a difference in length L (wave length) is the same,

$$\left.\frac{\partial \Phi}{\partial x}\right|_{x=x} = \left.\frac{\partial \Phi}{\partial x}\right|_{x=x+L} \tag{2.60}$$

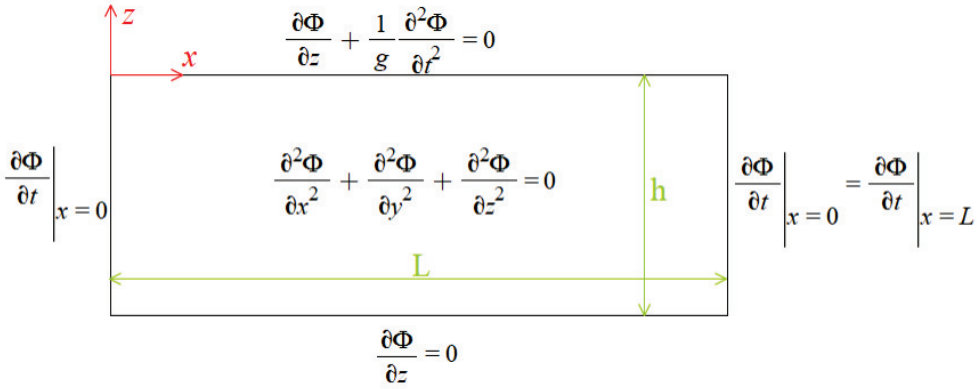


Figure 2.4. Sketch of the regular wave and boundary conditions (8)

The sketch formed as a result of the defined boundary conditions can be seen in Figure 2.4. Below equation can be obtained for the incident wave ($\Phi_0$); after solving the potential flow problem with given boundary conditions,

$$\Phi_0 = \mathbb{R}\left[\underbrace{\frac{igA}{\omega}\frac{\cosh(k(z+h))}{\cosh(kh)}\exp\{i(-kx\cos(\theta_{waves}) - ky\sin(\theta_{waves}))\}\exp\{i\omega t\}}_{\Phi_0(x,y,z)}\right] \tag{2.61}$$

$$\Phi_0 = \frac{gA}{\omega}\frac{\cosh(k(z+h))}{\cosh(kh)}\sin(\omega t - kx\cos(\theta_{waves}) - ky\sin(\theta_{waves})) \tag{2.62}$$

$\mathbb{R}$ : Real part of equation

$\omega = \frac{2\pi}{T}$ : Wave frequency with period of T

$k = \frac{2\pi}{L}$ : Spatial wave frequency or wave number

$A$ : Wave amplitude

$\Phi_0$ : Complex incident wave potential

$\theta_{waves}$ : Angle between waves and reference frame of floating structure

$\theta_{waves}$ is chosen as 180 degrees according to the wave flume case in the IZTECH hydraulic laboratory that results in $e^{i(-kx\cos(\theta_{waves}) - ky\sin(\theta_{waves}))} = e^{ikx}$ .The relationship between time and spatial frequency can be explained by dispersion:

$$\omega^2 = gk\tanh(kh) \tag{2.63}$$

After calculating the velocity potential, the first order wave elevation can be found through dynamic free surface boundary condition,

$$\eta = -\frac{1}{g}\frac{\partial \Phi_0}{\partial t}\bigg|_{z=0} = \mathbb{R}\big(Ae^{i(\omega t - kx\cos(\theta_{waves}) - ky\sin(\theta_{waves}))}\big) \tag{2.64}$$

$$\eta = A\cos\big(\omega t - kx\cos(\theta_{waves}) - ky\sin(\theta_{waves})\big) \tag{2.65}$$

### 2.3.2. Irregular Wave

The actual sea state in nature is irregular and cannot be represented by a single regular wave (48). Nevertheless, the linearity in potential flow allows for superposition. Therefore, the irregular wave can be defined as the sum of N regular waves with randomly shifted phases ($\psi_j$). Surface elevation can then be defined at $x = y = 0$ as:

$$\eta(x=0, y=0, t) = \mathbb{R}\left(\sum_{j=1}^{N} \underbrace{A_j e^{i\psi j}}_{\overline{A}_j} e^{i\omega_j t}\right) = \sum_{j=1}^{N} A_j \cos(\omega_j t + \psi_j) \tag{2.66}$$

$\overline{A}$ is the complex amplitude. The waves are stochastic due to their random phases. When examining a floating structure exposed to stochastic force, the statistical properties of the stochastic force must be constant over time. Pedersen et al. (51) state that the sea state is considered stationary for over 3-4 hours period. For stationary processes, the mean square of surface elevation is constant. When applying it to the wave with no phase at x=y=0 in the T period, the surface elevation is defined as equal to its variance:

$$\overline{\eta^2} = \sigma_n^2 = \frac{1}{T}\int_0^T \eta^2 dt = \frac{1}{2}A^2\frac{\big(\cos(T\omega)\sin(T\omega) + T\omega\big)}{T\omega} = \frac{1}{2}A^2 \tag{2.67}$$

Since $\omega = \frac{2\pi}{T}$, the equation is simplified with $\sin(2\pi) = 0$. It is also proof that these waves contain mean energy per unit area,

$$\overline{E_{tot}} = E_{potential} + E_{kinetic} = 2.\frac{1}{2}\rho g\sigma_n^2 = \frac{1}{2}\rho g A^2 \tag{2.68}$$

It is seen that there is a relationship between the amplitude of the wave and its energy. The discrete version of the spectral density function $S_\eta(f_j)$, which represents the frequency of

each wave ($f_j = \frac{\omega_j}{2\pi}$) in terms of energy contribution, can be defined as:

$$\sum_{j=1}^{N} S_\eta(f_j)\Delta f = \sigma_n^2 = \sum_{j=1}^{N} \frac{1}{2} A_j^2 \tag{2.69}$$

Both $S_\eta(f_j)$ and $A_j$ can be rewritten according to each other,

$$S_\eta(f_j)\Delta f = \frac{1}{2} A_j^2 \qquad \text{and} \qquad A_j = \sqrt{2 S_\eta(f_j)\Delta f} \tag{2.70}$$

The wave's amplitude can be found with a given spectrum, and the irregular sea state can be defined using equation 2.66. The JONSWAP spectrum, which is widely used to represent ocean waves, is defined as follows:

$$\begin{aligned} S_\eta(f_j)\Delta f = 0.3125 H_s^2 T_p \left(\frac{f}{f_p}\right)^{-5} \exp\left\{-1.25\left(\frac{f}{f_p}\right)^{-4}\right\} \\ .\left[1 - 0.287\ln(\gamma)\right]\gamma^{\exp\left\{-0.5\left(\frac{\frac{f}{f_p}-1}{\sigma}\right)^2\right\}} \end{aligned} \tag{2.71}$$

where the frequency with the most energy is called peak frequency ($f_p = \frac{1}{T_p}$). $H_s$ is named significant wave height, the mean of the highest 1/3 of the waves, and $H_s = 4\sigma_n$ in conjunction with a standard deviation. If $f =< f_p$, $\sigma = 0.07$ else $\sigma = 0.09$. $\gamma$ is the peak shape parameter that expresses how fully developed the sea state is. $\gamma = 1$ represents the fully developed sea state, in which the JONSWAP spectrum would be the same as the Pierson-Moskowitz spectrum.

## 2.4. Aerodynamic Effects of Floating Dynamics

As a result of the motion of the FOWT system in 6 DoF, there are instantaneous changes in the wind coming to the rotor, especially during the pitch motion. These instantaneous changes, combined with the tilt angle of the shaft, directly affect the angle of attack of the wind coming to the blade sections. This effect affects aerodynamic performance with phenomena called dynamic stall and violates the basic assumptions of the BEM model (7). Although advanced turbine control systems and certain DoF have active damping applications, FOWT systems have high speeds and accelerations at the rotor blade sections.

The thrust force acting on the rotor is balanced by the pitch restoring stiffness of the floating platform and the forces by mooring lines connected to the platform. Therefore, depending on the floating platform configuration, significant additional pitch angles

can occur on the platform. Active damping systems are also used to mitigate this additional angle. In the study carried out on the NREL 5 MW turbine (10), the reference turbine of the National renewable energy laboratory (NREL), a decrease of less than 1% is observed in the annual production of the turbine until the floating platform angle of $\theta_{pitch} \approx 4.5°$. When an onshore wind turbine with a capacity factor of $C_{p,onshore}$ is used as a FOWT, the effect of the pitch angle of the system on power production is approximated as follows,

$$P_{FOWT} = \frac{1}{2} C_{p,onshore} \rho A (U_0 . \cos(\theta_{pitch}))^3 \tag{2.72}$$

As mentioned in the problem definition, the interaction of the blade with the wake created by itself, which is called blade-wake-interaction, creates unsteadiness in the flow. Reduced frequency analysis evaluates the unsteadiness created by the platform movement at a specific frequency ($\omega_{platform}$ $[rad/s]$) on the blade (38),

$$k = \frac{\omega_{platform} c}{2U} \tag{2.73}$$

where $k$ represents the regime of the flow around the oscillating airfoil and $c$ is the chord length of the airfoil. When $k$ is less than 0.05, the flow is steady, and the circulatory contributions to the airfoil to lift dominate. When $k$ is greater than 0.05, the flow is unsteady, and the mass contribution from the acceleration effects drives the flow. The local relative wind speed over the blade section, which is the combination of the free stream wind speed and the rotational speed of the blade, without taking into account the induction factors, is as follows:

$$U = \sqrt{U_0^2 + (r\Omega)^2} \tag{2.74}$$

When the local velocity equation is placed in the reduced frequency equation, the flow regimes formed on the blade are defined by the following equation,

$$k = \frac{\omega_{platform} c(r)}{2\sqrt{U_0^2 + (r\Omega)^2}} \tag{2.75}$$

Figure 2.5 shows the possibility of NREL 5 MW turbine unsteadiness, depending on different floating platform configurations and operational conditions. The grey areas represent unsteadiness, and it is inferred from the Figure 2.5 that the inboard sections of the blade are sensitive to unsteadiness at lower wind speeds.

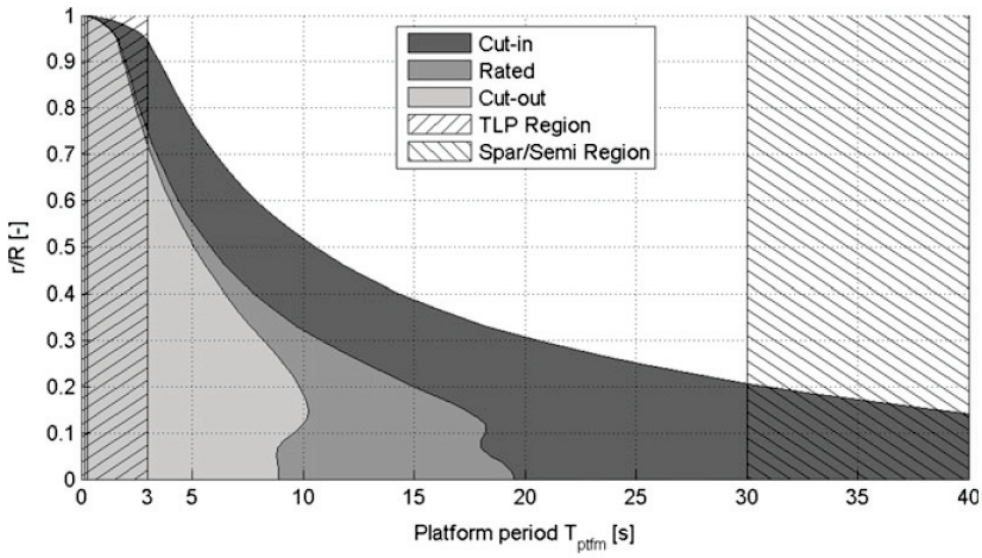


Figure 2.5. Possibility of unsteadiness along the blade of NREL 5 MW (10)

Last but not least, the axial movement of the platform ($U_{platform}$) affects the blade tip region. It creates recirculation at the blade tip due to high speeds, known as the vortex ring state. This recirculation breaks the momentum balance assumption by creating a highly unsteady transient flow, and the rotor acts as a propeller. Therefore, the following equation must be satisfied for the BEM model to be valid (10),

$$U_0 - U_{platform} => 2|aU_0| \tag{2.76}$$

Under extreme wave loads, the FOWT movement highly depends on the frequency and height of the wave. Especially a small turbine that tends to exhibit highly unsteady behavior is considered in this thesis. In order to understand the dynamics of the system, experimental studies should be carried out to obtain accurate results by taking into account all parameters.

# CHAPTER 3

# LITERATURE REVIEW

There are two main approaches in the scaled testing of FOWTs, which are backbones of the scaled model testing, full approach and simplified approach. These approaches have separate ways to represent loads coming from wind or wave. The first one is full approach which deals with a scaled model of whole wind turbine (i.e., rotor, nacelle, floating platform) with all its complexity. The second one is simplified approach which includes the minimum number of components to obtain accurate dynamic behavior of the FOWT. In simplified approach, one or more actuators are used instead of rotor or floating platform. Based on measured motion of the floating platform, the turbine loads are calculated by a software and the software runs the actuators instantaneously during the tests which is called software-in-loop (SIL) (52). In this study, full approach is considered for scaled model testing of the reference turbine with spar-type platform.

## 3.1. Full Approach

The first work in this field is done by testing a 5 MW turbine with the Hywind spar-buoy concept at the Froude-scale factor of 1/47 (53). In the test, which is performed to verify the numerical simulation results, active pitch control and active pitch control with active damping are compared under the above-rated wind speed operating conditions.

The second Froude-scaled FOWT model with a full-approach approach is developed by Goupee A. et al. (54), known as test campaign of DeepCwind (2010-2013). The NREL 5 MW reference turbine (55) with a rotor diameter of 126 meters is modeled at a 1/50 scale, and details can be found in Martin's thesis (6). The model wind turbine is mounted on three floating platforms: a tension-leg platform, a semi-submersible, and a spar buoy (56). Wind speed is not Froude-scaled to capture the overall thrust that contributes to the motion of the FOWT. The platform's motion and tower load responses are investigated in various wave and wind conditions, one of the test results can be seen in Figure 3.1 where it can be seen that the wind speed changes the response at the natural frequency of the surge. On the other hand, the amplitude in the wind speed frequency

range ($< 0.02\ Hz$) raised with increasing wind speed in the pitch response.

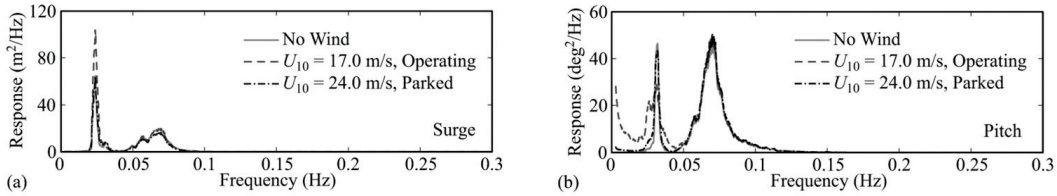


Figure 3.1. (a) surge and (b) pitch response of spar-buoy floating platform under an $H_s = 10.5m$ wave and three different wind conditions (11)

Second phase of DeepCwind experimental test campaign (57), is performed to validate and calibrate NREL 5 MW wind turbine simulated with FAST (aero-hydro-servo-elastic code). Froude-scaled wind is not used in this study as well. The discrepancy between simulation and experiment gets large when the second-order effects of the wave and dynamic mooring forces are present in the tests.

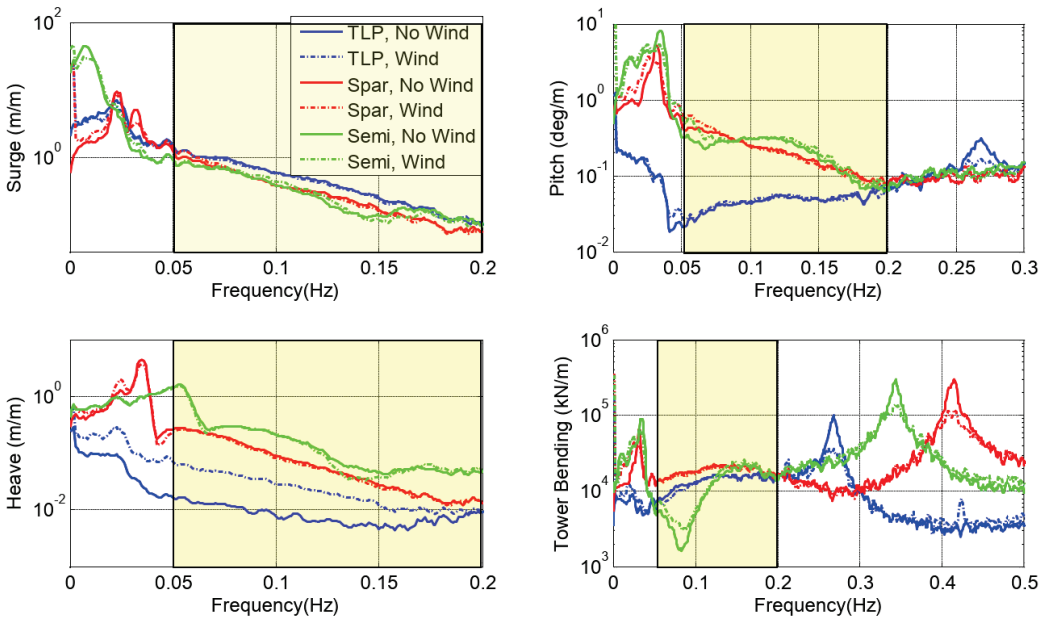


Figure 3.2. RAOs derived from white-noise wave excitation with $H_s = 7.1m$ without and with wind at 21.8 m/s; the colored box indicates the wave frequency range (12)

Summary of the DeepCwind results (12) show that the TSR must remain constant to get the correct damping effect from the wind in the Froude scale environment. Therefore, Martin et al. (58) proposed two ways to achieve the desired overall thrust with the

turbine Froude scale wind in the study. These options are roughened leading edge and redesigned blade for low Reynolds. With unpredictable results through roughened leading edge, Martin has shown that the better way is the thrust-matched redesigned blade. According to that study, Fowler et al. (46) demonstrated that the thrust-matched blade could capture full-scale overall thrust at Froude-scale wind speeds in the study.

The NREL 5MW turbine utilized in the DeepCwind project is revised for Froude-scaled wind and named as Marin Stock Wind Turbine (MSWT) by using CFD and BEM tools, as well as wind data from the first experiments (59). In addition, the system is integrated to enable active blade pitch control during the experiment. It is shown in wind/wave basin tests that MSWT performs much better than the geometric-matched model in emulating the behavior of the full-scale prototype (13), as shown in Figure 3.3. The thrust-matched blade, which has approximately three times longer chord length than the geometric-match blade, reaches 98.1% of the desired $C_T$ value at TSR of nearly 7, which is rated wind speed operating condition. Four different pitch angles are tried in the model to obtain the prototype $C_T$ value under various operating conditions. Ultimately, with $+3.5$ degrees pitch angle, it is achieved at a TSR of $5$.

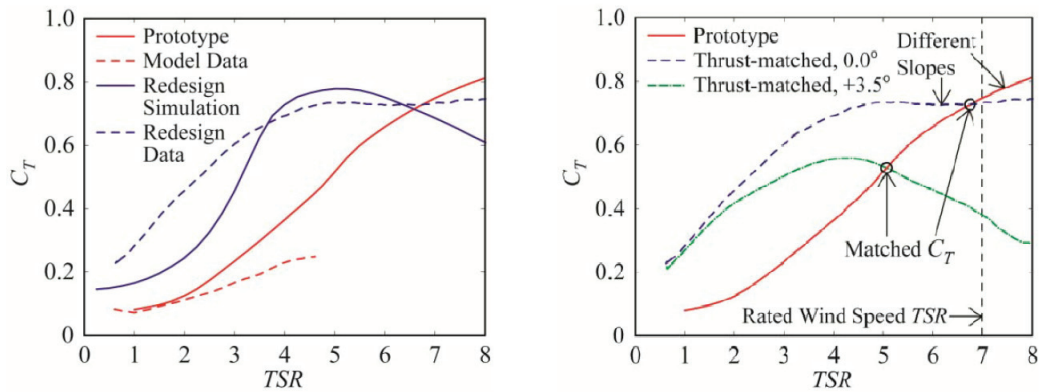


Figure 3.3. Left : Comparison of $C_t$ vs $TSR$ curves of geometric-match model, thrust-match model, and NREL 5 MW prototype. Right: Adjustment of pitch angle of blade to match $C_t$ with prototype (13)

The WINDFLO project operates the 1 MW two-bladed Vergnet turbine mounted on a semisubmersible with two thrust-matched blades in the Froude scale factor of 1/40 for hydrodynamic tests and 1/25 for aero-hydro tests (60). The test is carried out to verify the FastHydro code, which is developed to make numerical simulations in which second-order wave and dynamic mooring effects are considered. Rotational motions, especially

pitch motion, of the model FOWT are investigated under various conditions.

Within the scope of the INNWIND.EU project (61), the 1/45 scale OC4-DeepCwind semisubmersible floating platform with a 5 MW turbine is scaled up to 10 MW, represented by Robertson et al.(62), and the thrust-matched rotor is produced using a 1/60 Froude-scaled factor based on that design. Adjustments are made to catch the overall weight and center of gravity to achieve the same dynamic behavior. Numerical simulation is validated according to the experimental tests under various conditions at Ecole Centrale de Nantes (ECN) (63).

1/60 Froude-scale DTU 10 MW reference wind turbine (64) mounted on TLP platform is tested in Danish Hydraulic Institute (DHI) as part of the INWIND.EU project. The model was performed under various wave and wind conditions to validate the numerical model (65) implemented in the Flex 5 tool, which is based on unsteady BEM. The results increased the confidence in the numerical simulation (14). The probability of exceedance curves with and without wind are given in Figure 3.4; the mean value is subtracted from the whole signal. According to the experimental results, while the amplitude slightly decreased in the surge through wind, it increased slightly in pitch. It is seen that the wind increases the heave motion at a high rate.

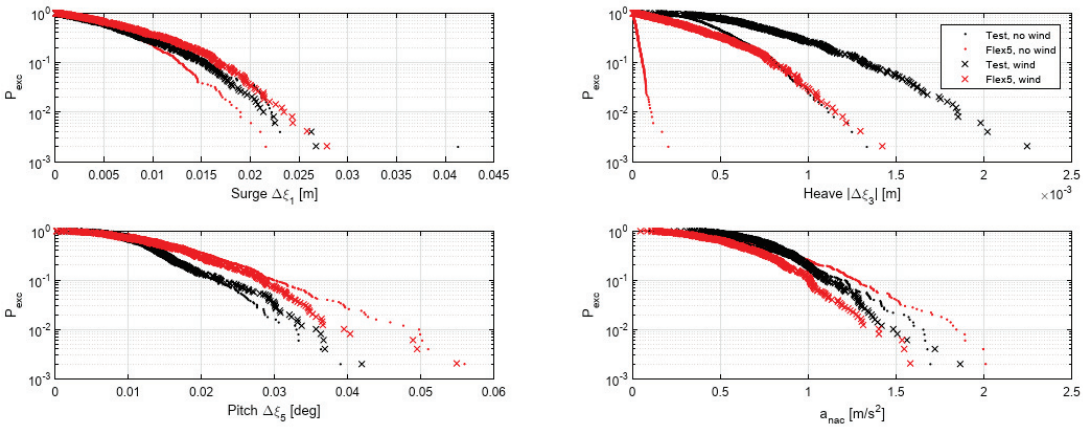


Figure 3.4. Comparison of the resuls of experiment and simulation with and without wind: $H_s = 4.14m$, $T_p = 0.94s$, $V_{rated} = 1.3m/s$, (14)

## 3.2. Simplified Approach

Roddier et al. (66) introduce an innovative version of semisubmersible as a new floating platform to mitigate pitch motion. All technical details about the early stage of the product (such as design, site assessment, fabrication, installation, and commissioning) are assessed in detail. After the aerodynamic simulation is solved with FAST, it is coupled with the hydrodynamic software TIMEFLOAT (TF) to compute the dynamics and kinematics of the FOWT. A 1/105 scale model of the prototype is produced and tested in the wave basin at UC Berkeley to validate this simulation (15). The drag disc, consisting of a foam board, is used instead of a rotor, and an electric motor rotates an aluminum rod with weights to emulate the gyroscopic effect created by the rotor during operation. The simulation and experiment results are shown in Figure 3.5 where it is seen that the wind does not affect the heave, the surge response of the system has slightly decreased through the wind with the increasing wave period. In addition, the pitch response decreased to about 12 seconds with the wind, then increased almost linearly with the increase in the period.

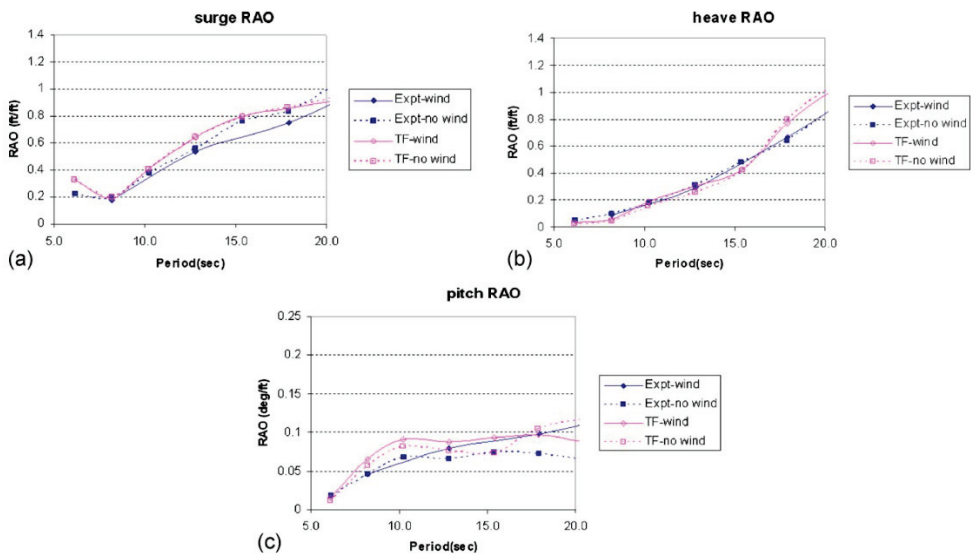


Figure 3.5. RAO of experiment and simulation with and without wind (15)

As an alternative way, Azcona et al. (16) employ a ducted fan to provide thrust force from the rotor during testing. The semisubmersible platform with a 6 MW wind turbine is modeled at a 1/40 scale, and several tests are performed at the wave tank of

ECN. In order to introduce variable thrust force by the fan, FAST is utilized to provide real-time feedback with a controller, known as hybrid testing with SIL. The results are given in Figure 3.6 where peak frequencies are formed at the natural frequency of surge and pitch. The second peak is occurred by the frequency of the wave. Moreover, it can be said that the wind increases the system energy at low frequencies, according to the wind frequency of 0-0.1 Hz in the experiment.

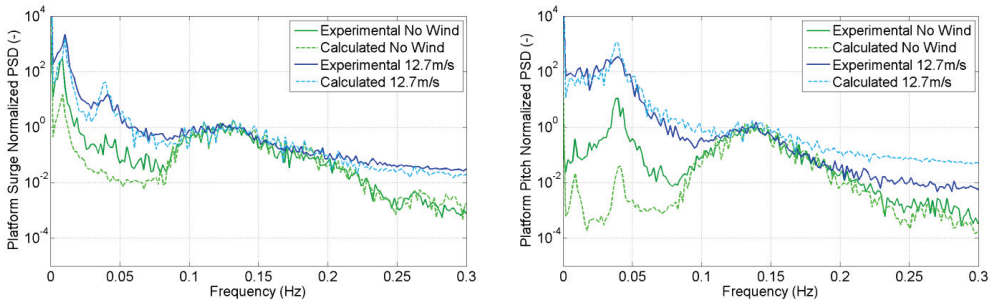


Figure 3.6. RAO of experiment and simulation with and without wind : $H_s = 2.64m$, $T_p = 7.3s$, (16)

Sauder et al. (67) propose a new way for wind/wave model testing of FOWT, called the real-time hybrid model (ReaTHM). While the aerodynamic forces are emulated by cables connected to the actuator and a frame placed on the tower top, the hydrodynamic parameters are measured from the physical test at MARINTEK's ocean basin . A 5MW-CSC wind turbine and braceless semisubmersible floating platform are scaled at 1/30 for basin testing. The measured data from sensors is given as input to the FAST code, and the full-scale simulation outputs are first converted to model scale, then fed to the actuators for the cable tensions. The results in Figure 3.7 show that the presence of wind only slightly affects pitch motion (17).

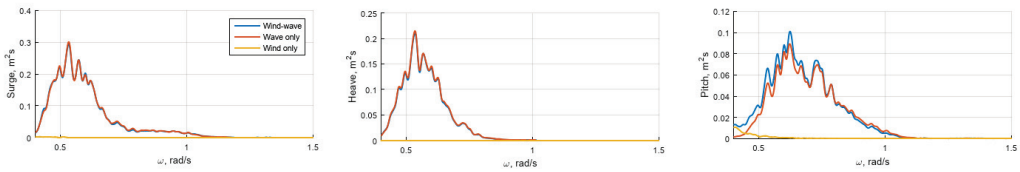


Figure 3.7. Platform motion spectra outputs of experiment under the wind-wave,only-wave,and only-wind conditions : $H_s = 3.6m$, $T_p = 10.2s$, $V = 11m/s$, (17)

Connecting actuators with many cables is a complex and challenging system to implement. In addition, since the ducted fan and drag disc cannot cover rotational and stall effects, they cannot fully represent the prototype rotor. Therefore, Meseguer and Raul (68) proposed a multi-fan system consisting of 6 motors to provide a rapid aerodynamic response to floating dynamic motion and rotational effects. While four fans only work in the wind direction to produce thrust, the other two fans create roll moment to mimic the effects of torque. The same SIL scheme in the ReaTHM is used in this study to feed the multi-fan actuators. Tested with a 1/40 scale NREL 5 MW turbine, the system catch the desired aerodynamic forces with a 1.5% deviation and show almost the same performance as the full-scale prototype.

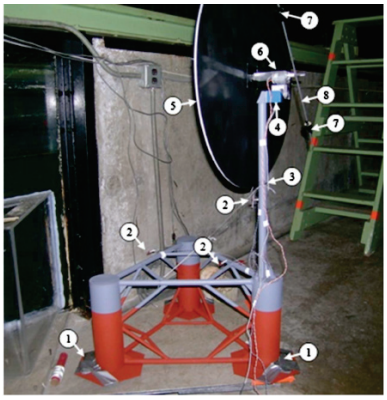

(a) Scaled model of the WindFloat model (15)

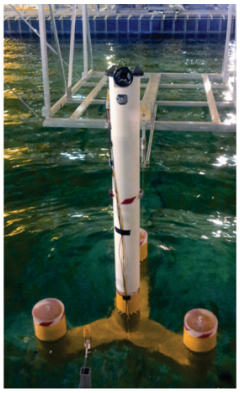

(b) Scaled model test with the ducted fan at ECN (16)

(c) The multi-fan actuator system (68)

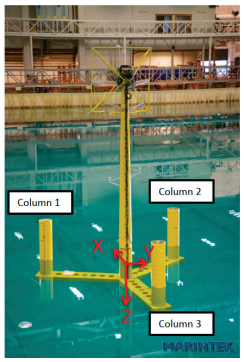


(d) Scaled model with the actuator-cable system for ReaTHM test (17)

Figure 3.8. Various concepts used in scaled model tests

Aerodynamic and mechatronic designs are considered for a 1/75 scaled model of DTU 10 MW at Politecnico di Milano in the study of Bayati et al. (69). Due to the lack of a wave basin facility that creates gravity-based wave loads, length and velocity scale factors are considered separately instead of Froude-scaling. Applying a higher velocity scale factor (such as 2,3) with an individual pitch control system reduces Reynolds dissimilitude. The results show good aggregation between the desired and the measured aerodynamic forces. A 6-DOFs HexaFloat robot is developed in the following work to simulate aerodynamic performance under floating motion (18). The tests are carried out in the atmospheric boundary layer wind tunnel. With SIL, measured data or hydrodynamic simulation data or hydrodynamic simulation based on measured data is given as input to the system, resulting in global motion output being physically reflected by the robot.

Figure 3.9. HexaFloat robot developed at Politecnico di Milano (18)

# CHAPTER 4

# EXPERIMENTAL SETUP OF IZTECH FOR SPAR-TYPE FOWT

The generation of a high-quality wind and wave environment in a model flume experiment is crucial for the correct coupling between the aerodynamic and hydrodynamic forces on the floating wind turbines. In this study, aerodynamic and hydrodynamic design are considered for a 1/40 Froude-scaled model of Northel Poyra P36/300 turbine with spar-type platform. An experiment campaign is used to investigate the dynamic behavior of the spar-type floating offshore wind turbine (FOWT) under various wave loads and extreme wind condition. The spar platform's, wind nozzle characteristics and effect of the wind on the FOWT motion have been investigated. Experimental study are carried out in the wave flume in the hydraulic laboratory of IYTE Civil Engineering Department. A sketch of the flume's is provided in Figure 4.1.

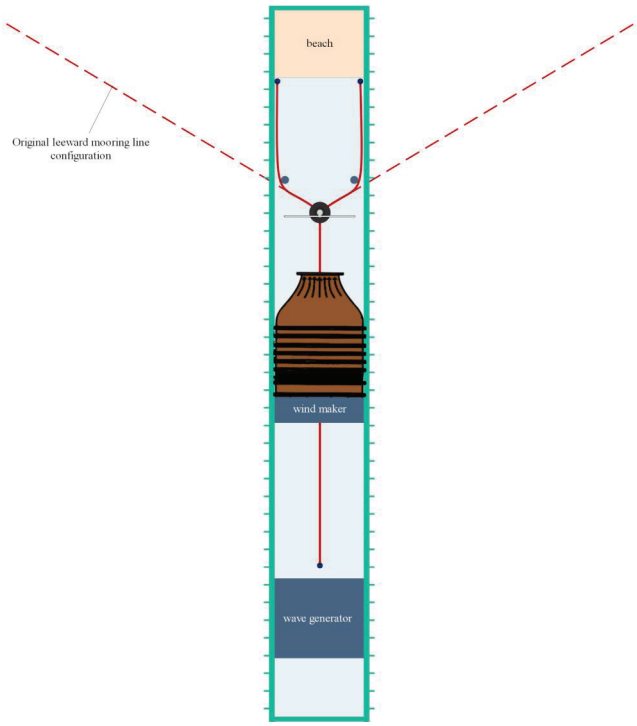


Figure 4.1. Top-sketch view of the test setup (19)

## 4.1. Model Setup

Physical and numerical models are used to investigate the stability and aero-hydrodynamic responses of floating offshore wind turbines. There are many different numerical tools on this subject and it is stated in the literature that they give very good results (70). However, since numerical models are created by considering certain assumptions and simplifications, they must be validated with physical model experiments. On the other hand, the field experiment with very large dimensions of the systems is usually financially prohibited. Duration of the tests, uncontrollable and unrepeatable environmental conditions, and the product rights of full-scale commercial prototype are some of the constraints of the field experiments (71). For these reasons, one of the preferred methods in experimental studies is scaling in a controlled environment. It can still be seen as an fundamental validation step in the system behavior.

### 4.1.1. Wave Flume

Dimensions of the wave flume of IZTECH Hydrodynamics Laboratory is 40 m (length) × 1 m (width) × 1.4 m (depth). The wave flume was constructed from steel except middle section of one side, which is 8-m-long thick glass. The glass section helps to observe the dynamics of the FOWT during the experiment. A piston type wave-maker with a 5kW servo motor drives the wave maker which is aimed to generate sea states with irregular (variable period and wave height) waves that observed in nature as well as regular (sinusoidal, constant height and period) waves to be used in basic experiments. A dissipation beach, which is made of rocks of various sizes with a 1/5 gradient, is placed at the opposite end to absorb the waves that otherwise reflect backward, as shown in Figure 4.2. Moreover, the waves propagate to the back of the piston, creating splashes and the risk of damaging the motor when the generated and reflected waves interfere. For this reason, a steel cage filled with absorbent material (plastic sponge) were placed to damp the waves in this area.

Figure 4.2. The dissipating beach with 1/5 gradient placed at the end of the channel

### 4.1.2. Wind Nozzle

The constraint that must be complied with in the design of the wind nozzle is the width of the wave flume which is equal to $1$ meter. The wind nozzle was designed with intentions of maintaining air flow for the wind turbine considering its motion under the waves (as explained in section 2.1). In this study, the length scale factor was chosen as $40$, therefore the velocity scale factor must be around $6.5$ according to Froude scaling. Since the primary goal is to accurately capture motion of the turbine under the extreme conditions, the range of $15 - 25m/s$ -which is close to cut-out wind speed- are mainly examined. Accordingly, the wind speeds generated by wind nozzle are between $2.3 - 3.8m/s$. Analytical studies often rely on potential flow theory for the design of contraction nozzle curves. On the other hand, numerical simulation gives more realistic results because of modelling the boundary layer. Moreover, in contraction regions of small wind tunnels, it has been seen that 5th or 4th order polynomials give very good results (72). For this reason, 4th order polynomials were used in the design of the nozzle, considering the simplicity of fabrication process.

To reduce turbulence intensity and obtain uniform flow, the contraction nozzle is commonly used in wind tunnel applications. Turbulence intensity, the simplest form of turbulence measurement, is obtained by dividing the standard deviation of the wind speed

by the mean wind speed.

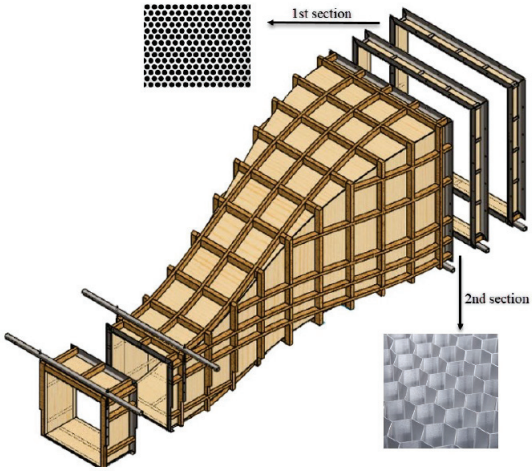


Figure 4.3. Exploded view of screens, and a contracting nozzle

Two different designs of the nozzle ( as shown in Figure 4.4) were manufactured with the purpose of creating model wind flow. The first nozzle was manufactured in 2018 as part of the M.Sc. thesis of Serkan EROL (73), Figure 4.3. The nozzle is 3.6 m long and has a cross-sectional inlet area of 1.8x1.8$m^2$ and outlet area of 0.9x0.9$m^2$ (0.25 contraction ratio). Honeycomb and perforated were placed between fans and inlet section of the nozzle to obtain low turbulence flow by decomposing large eddies. To characterize its real performance, someintensive experimental measurements have been conducted using hot wire anemometer and pitot tube with U-tube micro manometer. The results shows that the range of generated wind speed is not enough to meet the expectations when heave motion of the FOWT -due to the wave- is taken into account.

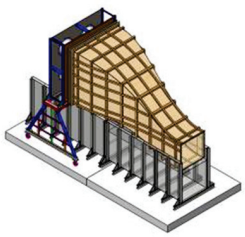

(a) First contraction nozzle design

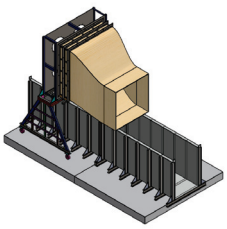

(b) Second contraction nozzle design

Figure 4.4. Nozzle Designs

Therefore, a new nozzle was designed by switching length, outlet area based on outcome of the experiment. In addition, the contraction curve was re-defined with new dimensions. A contraction ratio of 1/2 has been chosen, resulting in an outlet area of 1.2x1.4 $m^2$ and 1.8 m long, Figure 4.4b.

### 4.1.3. Traverse Mechanism

Positioning precision is only required along height of the wave flume to acquire air flow properties accurately with measurement sensors. The translational movement are provided automatically by a stepper motor with precision of 0.1 mm and motor is controlled using LabVIEW software. Schematic of the traverse mechanism shown in Figure 4.5. On the other hand, to reduce the cost of the traverse mechanism, it is moved along the wave flume direction(x) and in the horizontal (y) axis manually with sigma profiles. 45x45x1700mm heavy sigma profiles called ”A” shown in Figure 4.5 are fixed to the carrier frame through brackets. Along the wave flume axis, 45x45x1800mm heavy sigma profiles named as ”C” were connected with the same 300mm long heavy sigma profiles called ”B”. The connection bolts are tightened when positioning is done. In the same way, the 45x180x500mm heavy sigma profile called ”D” was moved in a similar way and manual positioning was made on the horizontal axis of the wave flume.

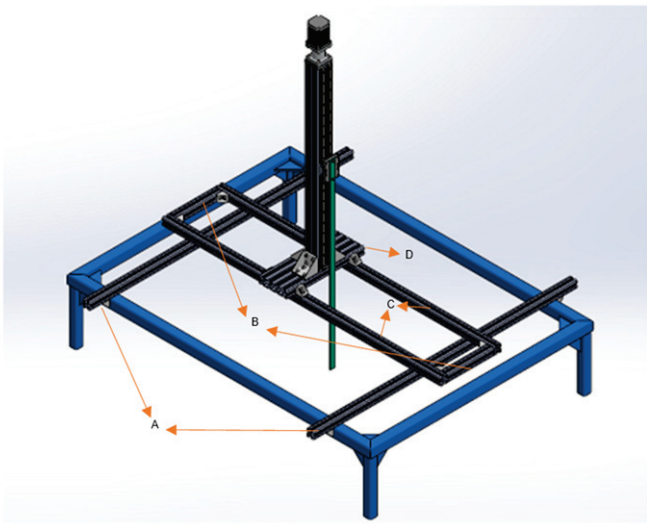


Figure 4.5. Traverse Mechanism

### 4.1.4. Model Turbine

The wind turbine is a 1/40 scaled version of Northel Poyra P36/300 reference wind turbine and due to the Reynolds dissimilitude and dynamic scaling issues, the blades of the wind turbine were redesigned to preserve drag coefficient and obtain max torque. All details about the model turbine design and manufacturing are given in Serkan Erol's master thesis (73). Some important information from the reference above is summarized below for completeness.

Although the study is novel in terms of turbine nominal power and size, this novelty brings important constraints to fabrication of the components and instrumentation. It is extremely difficult to make a mold for a blade of this size since the thickness becomes lower than 1 mm at the tip region of blade. A hollow and light blade structure is required to satisfy desired moment of inertia. For these reasons, 3D printing method was chosen to produce the blades.

Low Reynolds number drastically reduces the aerodynamics performance of blades, thus, the blades were redesigned to match overall thrust coefficient. Due to the open jet flow generated by the nozzle on the wave flume, the unsteady aerodynamic behavior of the scaled rotor is not the main interest of the experiment unlike the wind tunnel tests. When the scaled thrust is obtained under the Froude scaled wind conditions and operation, the rotor is said to perform at model scale which is called performance-scaled rotors. Furthermore, motor was employed to reach desired rotational speed due to inadequate torque generated by rotor. The motor is controlled instantaneously by a PID controller.

Table 4.1. Operational parameters of the turbine ($\lambda = 1/40$)

| **Parameters** | **Reference** | **Scaling Factor** | **Model** |
|---|---|---|---|
| Wind Speed | 20 $m/s$ | $\lambda^{0.5}$ | 3.16 $m/s$ |
| Rotor Speed | 50 rpm | $\lambda^{-0.5}$ | 316.22 rpm |
| Power | 320 kW | $\lambda^{3.5}$ | 0.79 W |
| Power Coefficient | 0.064 | 1 | 0.064 |
| Thrust | 18.9 kN | $\lambda^{3}$ | 0.296 N |
| Thrust Coefficient | 0.076 | 1 | 0.076 |

Both Computational Fluid Dynamic (CFD) and Blade Element Momentum The-

ory (BEMT) simulations were performed for the specified operational conditions given in Table 4.1, during the rotor design stage, to select best design in terms of performance. Results shows that Ishii airfoil (Figure 4.6) with a given configuration in Figure 4.7, creates thrust force of 0.303 N, 0.32 N in BEMT and CFD respectively while the scaled thrust is 0.296 N. These values considered to be close enough for our experimental purposes.

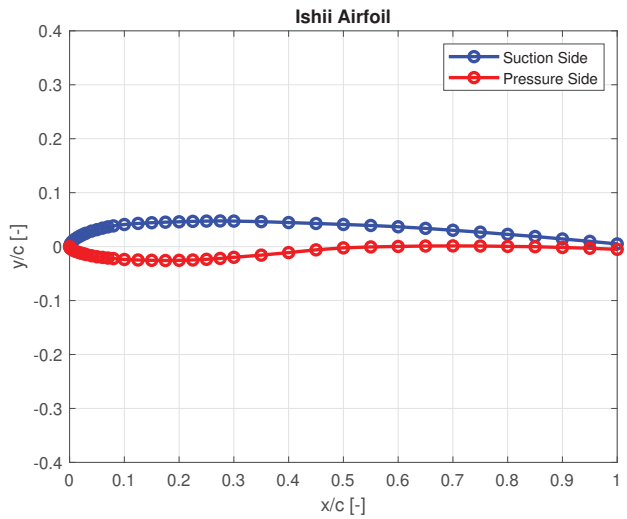


Figure 4.6. The airfoil section used in the model study

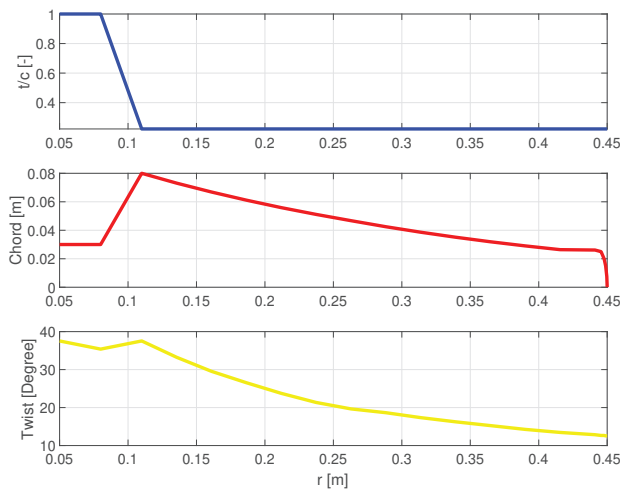


Figure 4.7. Geometric model of blade design parameters

Center of gravity (CoG) of the reference turbine at 26.24 meters high on tower. To model the dynamic behavior of the reference turbine, model turbine must have the same

scaled mass and center of gravity (0.65 m) as well. Therefore, each component have to be designed respecting the mass reduction of the scaling. Table 4.2 shows that, although total mass was obtained correctly, desired individual masses were not achieved for each component.

Table 4.2. Mass values of model turbine components

| **Components** | **Reference [kg]** | **Desired Mass[gr]** | **Manufactured Mass[gr]** |
|---|---|---|---|
| 3x Blade mass | 5322 | 83.15 | 112.52 |
| Tower mass | 34900.7 | 545.32 | 495.65 |
| Hub mass | 4420 | 69.06 | 105.47 |
| Nacelle mass | 21796 | 340.56 | 321.76 |
| Total mass | 66438.7 | 1038.10 | 1035.4 |

### 4.1.5. Model Spar-Type Floating Platform

The spar-type floating platform, which is well-known ballast-stability scheme in the literature, was chosen since it is a suitable type of platform in terms of geometry for using in wave flume of IZTECH and also there are plenty of data in the open literature. There are two forces which drives the spar platform stability in water during its static state. One of them is downward gravity forces (weight of system) acting at center of gravity and the other one is buoyancy force which is equal to weight of water displaced by immersed volume of spar, acting at centroid of the immersed volume. Rotational motion changes the center of volume, and buoyancy force act as a restoring force to return the floating platform it's first equilibrium position. This only happens if metacentric height is positive, which is defined as the distance between metacenter and the center of gravity, and by the following equation (4.1), and shown schematically in the Figure 4.8 . Otherwise, metacentric height provoke unstable condition.

$$\overline{GM} = M - G \tag{4.1}$$

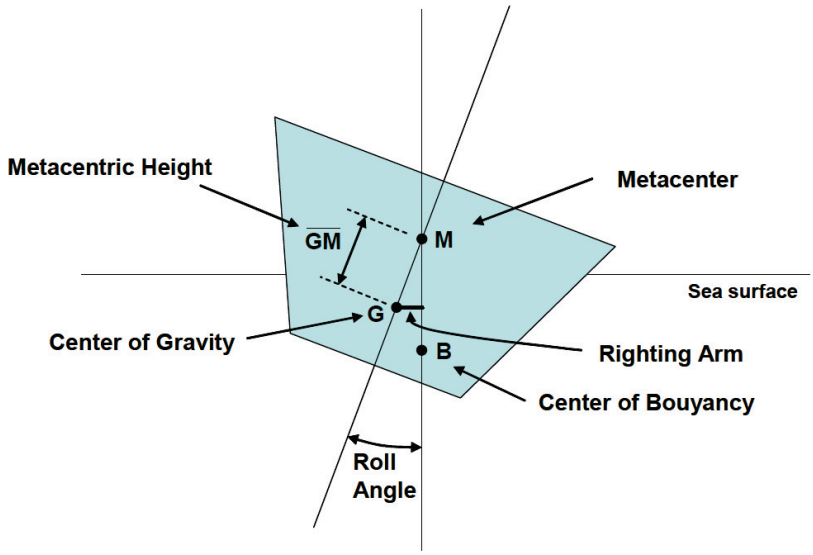


Figure 4.8. Illustration of metacenter and metacentric height (20)

A parametric analysis was performed considering mass, inertia, mooring lines, hydrodynamic and aerodynamic forces on the reference turbine. Since water depth is 1 meter in the setup, numerical studies were done with 40 meters depth and scaled down for 1/40 Froude-scaled model. The dimensions of the scaled model are shown in Table 4.4 and 4.3, with parameters given in Figure 4.9.

In the production process, to satisfy the dynamic similitude, stainless steel material was used to fabricate mooring lines and the shell (thickness of 2 mm) of the spar platform. A cap on the spar platform was designed for adjustment of the ballast weight. The balance between buoyancy and weight must be accurately matched to preserve platform stability (71). There is a material difference between practice and theory, which case a shift in the CoG. Ballast of the model is adjusted by adding sand and pebble mix. Density calculations of the mixture were made and the necessary density was obtained as $1.6gr/cm^3$. According to this calculation, 5430 grams of mixture was placed in the spar which creates a height of $10.4cm$ . However, in the calculations, it was seen that more weight should be added to ensure the total weight and center of gravity met the requirements, for this purpose, a 2 cm thick iron plate was mounted under the spar model.

Table 4.3. Structural and hydrostatic properties of spar platform

| **Parameter** | **Value** |
|---|---|
| Mass | 17.565 kg |
| Draft | 0.6336 m |
| The volume of displaced water | 0.0176 $m^3$ |
| Roll inertia | 1.919 $kgm^2$ |
| Pitch inertia | 1.919 $kgm^2$ |
| Yaw inertia | 0.04 $kgm^2$ |
| Center of mass below SWL | 0.411 $m$ |
| Center of buoyancy below SWL | 0.363 $m$ |
| Metacentric height $GM$ | 0.0481 $m$ |
| Static buoyancy force | 172.936 $N$ |
| Heave hydrostatic stiffness | 31.068 $N/m$ |
| Roll hydrostatic stiffness | 0.145 $N.m/°$ |
| Pitch hydrostatic stiffness | 0.145 $N.m/°$ |

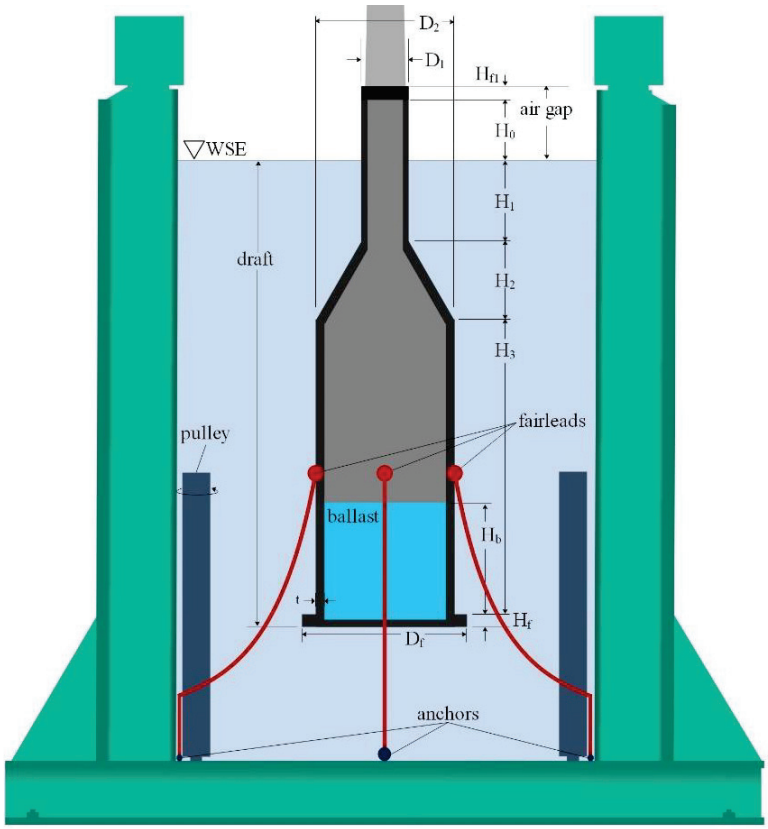


Figure 4.9. Schematic view of spar platform (19)

Table 4.4. Scaled parameters of spar platform

| **Parameter** | **Value [mm]** |
|---|---|
| $D_f$ | 204 |
| $D_2$ | 204 |
| $D_1$ | 63.5 |
| $H_f$ | 4 |
| $H_b$ | 125 |
| $H_3$ | 504.5 |
| $H_2$ | 50 |
| $H_1$ | 75 |
| $H_0$ | 50 |
| $H_{f1}$ | 25 |
| t | 2 |

The weight and center of gravity information of all components in the FOWT system which is employed in the experiment are given in Table 4.5.

Table 4.5. Weights and CoG of the FOWT

| **Parameter** | **Weight [gr]** | **CoG on Z-axis [mm]** |
|---|---|---|
| Turbine + Turbine-Spar Connection Part | 1243.5 | 617.37 |
| 3 x Ping pong ball | 10.33 | 475.33 |
| Empty spar | 6484 | -432.6 |
| Ballast Mix (Sand+Pebble) | 5430 | -648.7 |
| Iron plate (under the spar) | 4088 | -714.6 |
| Mooring lines (attached the fairled) | 310 | -486 |
| Total mass | 17565 | -491.13 |
| Center of mass below SWL | | -416.13 |

After the weights measurement process, first the center of gravity of the empty spar and the turbine were both numerically calculated and experimentally measured for validation of the center of gravity. The measurement of the center of gravity was made by hanging the empty spar and turbine model with the wire, parallel to the ground, as shown in Figure 4.10, and location was recorded during balance state. The center of gravity is 262.5 mm below from the connection surface of turbine and spar which origin point of

the coordinate system. Secondly, the FOWT was put into the water, draft was measured. The draft was 63 cm, the result is very close to the target value of 63.3 cm which given in Table 4.3.

Figure 4.10. Measurement of center of gravity

According to the results, there are very small differences between design and model, hence it is assumed that the model satisfies the requirements.

## 4.2. Instrumentation and The Tools of Experiments

An accurate measurement is an essential part of an experiment. It helps to quantify conditions before and during the test. Characterization of wave maker and wind nozzle were performed through measuring the wave height, wave period, outlet air velocity at different positions from the nozzle, and turbulence intensity of the air profile before the test. Moreover, wave probes were also used in wave measurement, a strain gauge for the thrust measurement, Go-Pro Hero 5 camera with three ping pong balls, as seen in Figure 4.11, were used to capture the 2-dimensional motion of the FOWT during the test. In this study, main interest are wind, thrust and motion thus, interested reader can find more information in the study of Kadir (74). Following paragraphs will give information about

the calibration of sensors. The sensors are as follows: hot-wire, strain gauge and image processing tools.

Figure 4.11. Ping-pong balls that placed on the tower

### 4.2.1. Hot-wire

The hot-wire anemometer was used to measure the velocity of the wind nozzle at different distances and the velocity differences, such as wind shear, that occur around the

model wind turbine. Hot-Wire anemometer gives precise and fast results. In order to use the hot wire anemometer, it is necessary to calibrate the sensor against a known velocity. The tools which were needed for the calibration: calibration nozzle, DC motor, DC power supply, hot-wire probe, pitot tube, micro U-manometer, computer and anemometer system.

The reference flow for the calibration is needed to be laminar steady flow. In order to obtain such a flow, a nozzle as shown in Figure 4.12, is used. The grid and wire mesh was employed to obtain a lower turbulent flow at the nozzle exit.

Figure 4.12. Calibration nozzle

The anemometer system is a constant temperature type, more information about it can be found in the reference (75) . This voltage is measured with the help of a 16-bit DAQ card and recorded on a computer.

The working principle of the hot-wire can be explained simply as the heat transfer between the heated wire and the cold air flow around it. This heat transfer is a function of the air velocity. A relation is defined between the air velocity and the electrical voltage through this principle. The main purpose of the hot-wire electronic circuit is to provide a controlled amount of electric current to the wire part (75).

The wind speed given to the anemometer was measured against a High Wycombe L type pitot tube connected to the Dwyer Model M1430 Microtector U-manometer seen in Figure 4.13. Before the calibration, the consistency of the pitot tube at very low $(0-2m/s)$ wind speeds was measured at outlet of the calibration nozzle. The height value ”h” of the

Dwyer manometer, which shows the pressure difference between the two outlets of the pitot tube, was taken many times for the same condition, and the wind speed at the nozzle outlet was calculated with the Bernoulli equation given at Eqn 4.2 .

$$p_1 + \frac{1}{2}\rho_{air}V_1^2 = p_2 + \frac{1}{2}\rho_{air}V_2^2 \tag{4.2}$$

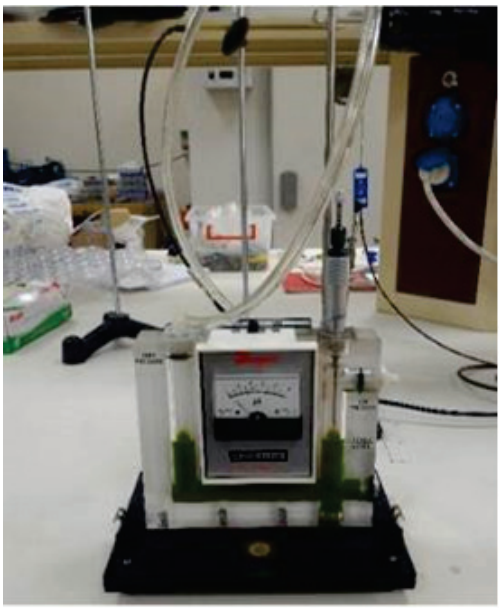

Figure 4.13. Dwyer Model M1430 Microtector U-manometer

When the static pressure is accepted as the 1st state and the stagnation pressure as the 2nd state, it is simplified as the equation 4.3 and the velocity is found by calculating the pressure difference with the height ”h” which is measured in the U-manometer. It has been observed that the Pitot tube gives very high consistency results until the minimum (0.72 m⁄s) wind speed.

$$\Delta P = \rho_{fluid} * g * h \Longrightarrow V_2 = \sqrt{\frac{2\Delta P}{\rho_{air}}} \tag{4.3}$$

A calibration curve with high consistency was obtained between the voltage value that changes according to the wind speed and measured manometer data, through 4th order polynomial fit, Figure 4.15.

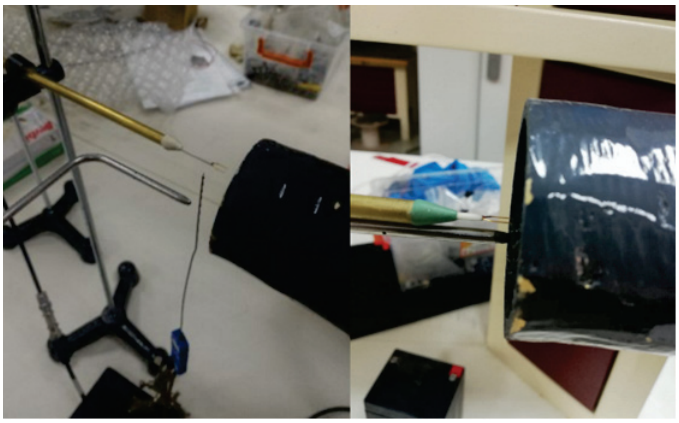

Figure 4.14. Calibration process of hot-wire

$$Velocity(V) = -0.0003559 * V^4 + 0.002151 * V^3 + 0.07404 * V^2 + 0.8124 * V + 4.196 \tag{4.4}$$

Changing environmental conditions affect the sensitivity of the hot-wire anemometer, and therefore it needs to be calibrated regularly.

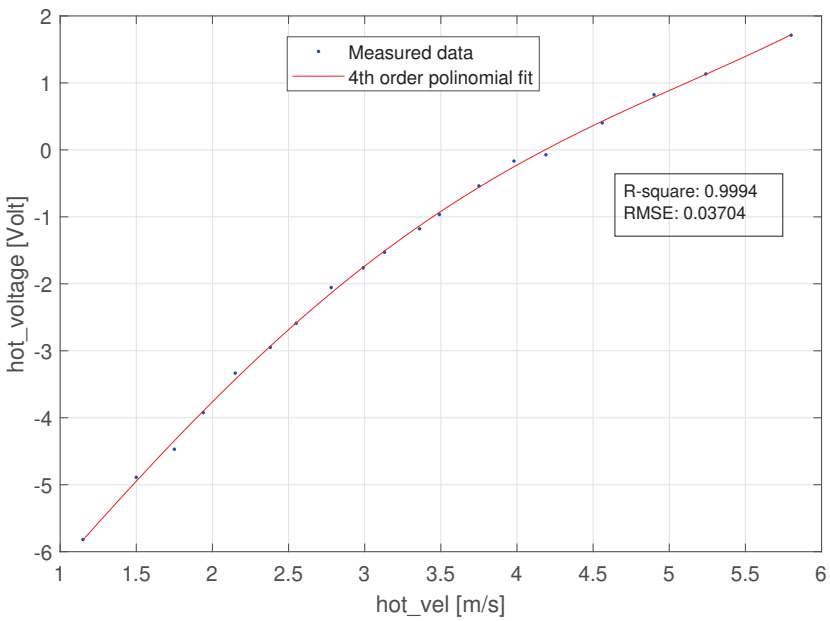


Figure 4.15. Calibration curve of hot-wire

### 4.2.2. Strain gauge

The measurement of the thrust on the turbine tower ca not be obtained directly, but instead total dynamic force on the tower was obtained by measuring the strain at the bottom part of the tower by means of a strain gauge. In this application, it is aimed to measure all the forces on the turbine first and to find only the thrust force coming from the wind. In this study, BF350-3AA / 1.5AA model strain gauge module, which consists of 1 gauge and 1 amplifier, were used. This module provides analog output voltage between 0-3.5 V. The gauges are placed on the tower at angle of 90 ° as shown in Figure 4.16.

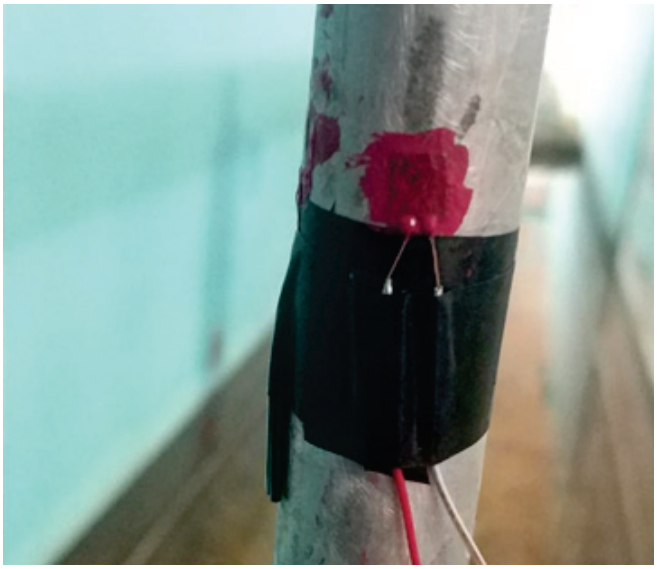

Figure 4.16. Strain gauge sensor on the tower bottom

In order to read the resistance change in the strain gauges, these gauges were first connected to the Wheatstone-bridge and the amplifier. The signals at the output of the amplifier were sent directly to the computer via a 16 bit data acquisition card (PCI-1710HGU) and record at 100 Hz.

Since the resistance change in the strain gauge is converted to voltage with the whitstone-bridge, the device must be calibrated in order to understand the force that causes the voltage change. The calibration measurement was made by recording the voltage values obtained by applying a known forces to the tower. A trendline was created with the voltage values and a curve fitting equation was derived as seen in Figure 4.17.

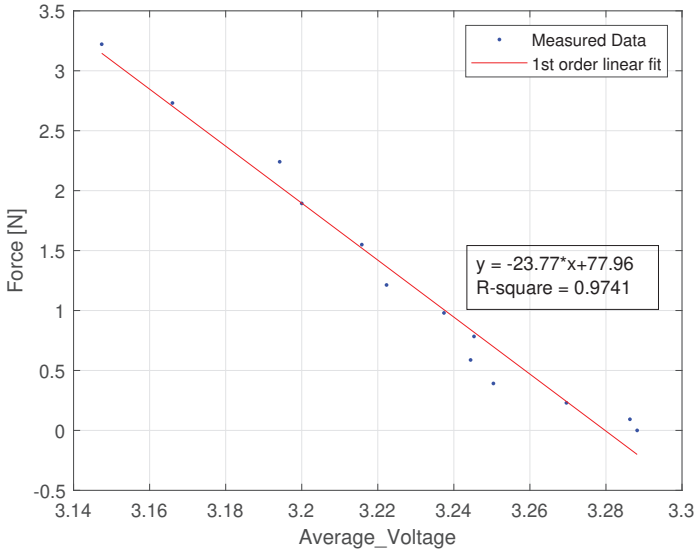


Figure 4.17. Calibration curve of Strain gauge

### 4.2.3. Image processing tool

Image processing technique was employed to analyze the motion of the floating wind turbine model in wave and wind conditions over time. For this purpose, colored ping pong balls were glued on the turbine tower and video recorded at 120 frame per second with a high resolution camera (GoPro Hero 5) during the experiments. The processing of recorded videos is carried out with an open source program called **Tracker** (76). Tracker receives the video and process it as successive frames. For example, a 60-second video with a 120Hz camera consists of 120x60=7200 frames. In the Tracker program, steps are as follows:

- The first frame of the video is chosen as a reference and an origin point is defined in this frame.
- A calibration line is drawn from the top reference point (red ball) to the bottom reference point, and the length of this line is defined as the real distance between the balls, 0.725 meter. The program calibrates itself by proportioning the length in pixels of the calibration line in the first frame to the length in defined meters.
- Then, by following these balls in each frame of the video, the horizontal and vertical (time-dependent) distances with respect to the origin point are recorded by the

program.

The Tracker GUI shown in Figure 4.18. Here, the intersection of the purple lines represents the origin, and the blue line represents the calibration line. The graph of ball's positions depend on time in the horizontal and vertical planes, as it is shown in the upper right window, and the same values are shown as a table in the lower right window. The processed position data is then decomposed into surge, pitch, and heave movements with a written Matlab code which will explained following part.

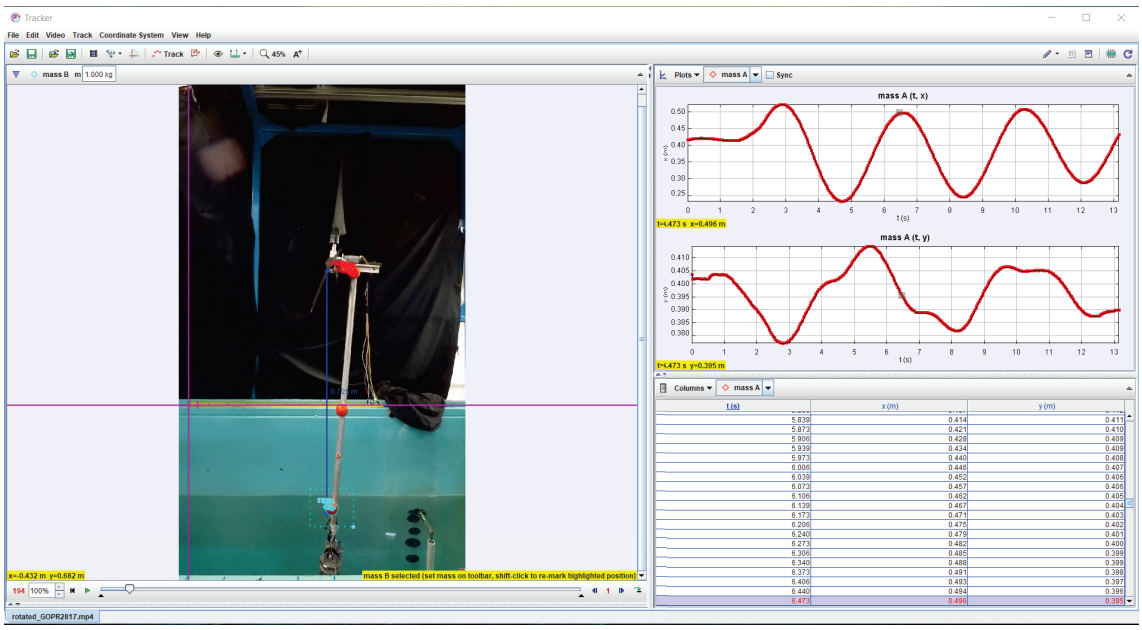


Figure 4.18. View from Tracker program

The distance (1446 mm) of the center of gravity from Point 1 (red reference point in the Figure 4.18) is used to separate translation from rotation. Point 1 is the point close to the nacelle, Point 2 (white reference point in the Figure 4.18) is the point close to the water level. The coordinates obtained as a result of image processing and the center of gravity can be created virtually with the following equations.

$$Angle_i = atan(\frac{Y_i^{Point-1} - Y_i^{Point-2}}{X_i^{Point-1} - X_i^{Point-2}}) \tag{4.5}$$

$$Distance = 1446mm$$

$$CoG_i^X = X_i^{Point-1} + (Distance * cos(Angle_i)) \tag{4.6}$$

$$CoG_i^Y = Y_i^{Point-1} + (Distance * sin(Angle_i)) \tag{4.7}$$

Since the center of gravity is also the center of rotation. If CoG motion is calculated and subtracted from entire motion, the difference will only give the rotational motion. When each time step is specified in $i$:

$$Surge_i = CoG_{i+1}^X - CoG_i^X \tag{4.8}$$

$$Heave_i = CoG_{i+1}^Y - CoG_i^Y \tag{4.9}$$

$$Pitch_i = atan(\frac{Y_{i+1}^{Point-1} - Heave_i - Y_i^{Point-1}}{X_{i+1}^{Point-1} - Surge_i - X_i^{Point-1}}) \tag{4.10}$$

Summation of all these instantaneous surge and heave motions will give the total translational motion.

# CHAPTER 5

# RESULTS

## 5.1. Atmospheric Boundary Layer Reproduction

The lowest layer of the troposphere, which is directly affected by the presence of the Earth's surface, is defined as the atmospheric boundary layer. The surface layer (a.k.a. atmospheric boundary layer), where the forces occur due to the turbulent motions of the air. The height of the layer is about 100 meters, and the wind speed increases rapidly with height. The wind profile in the surface layer is approximated by the logarithmic equation as follows (77):

$$u(z) = \frac{u_*}{\kappa} ln(\frac{z}{z_0}) \tag{5.1}$$

where z is the mean height above ground level, u is the time average wind speed at that height , $u_*$ is the friction velocity ($u_* = \sqrt{\frac{\tau}{\rho}}$) and $\kappa$ is the Von-Karman constant, which is taken as 0.40 in boundary layer meteorology. Due to the no-slip condition attached to the wall, the wind speed in the surface boundary layer should decrease and become zero as it approaches the surface. The $z_0$ height ,where the wind speed is zero, is defined as the roughness or aerodynamic roughness and its value is not equal to zero.

Table 5.1. Roughness values according to landscape type (22)

| **Landscape Type** | **Water** | **Snow** | **Grass** | **Farmland** | **Forest** | **City** |
|---|---|---|---|---|---|---|
| Roughness [m] | $2 * 10^{-4}$ | $10^{-3}$ | 0.03 | 0.1 | 0.8 | 1.0 |

Over 2/3 of the earth's surface consists of water surfaces such as oceans, seas and lakes, and the marine boundary layer plays major role in small-scale air-sea interaction. There are great differences between the soil and sea surface due to thermodynamic and dynamic characteristics. Roughness of sea is calculated as $2 * 10^{-4}$ meter as seen in Table

5.1. This is acceptable for long-term climate events. When calm and stormy sea states are compared, it is seen that the roughness depends on the wind speed. It has been observed that in severe stormy weather conditions over the open oceans, waves reach frightening dimensions of 20-30 meters (78). For terrains where air interacts with sea, the Charnock roughness equation is defined based on friction velocity (79):

$$z_0 = a\frac{u_*^2}{g} \tag{5.2}$$

where ”a” is the Charnock constant, and g is gravity acceleration. In the absence of any field data regarding turbulence, IEC 61400-3 “Design requirements for offshore wind turbines” standard recommends that the roughness and standard deviation of the turbulence should be calculated by the Charnock equation with the following equations (80):

$$z_0 = \frac{a}{g}\left[\frac{\kappa * V_{hub}}{ln(\frac{z_{hub}}{z_0})}\right]^2 \tag{5.3}$$

The turbulence intensity above the sea is higher at low speeds and decreases with increasing wind speed, reaching a minimum value at 8 m/s – 12 m/s and continues to increase slowly for speeds higher than 12 m/s (81).

According to the operational conditions of the reference turbine ($20m/s$ ) wind speed and 1/40 scaling factor, the desired wind speed at the hub height of the model turbine (36 meters) was calculated to be ($3.16m/s$). The hub height is 41 meters together with the height above still water level of the floating platform.

For neutral atmospheric conditions, Wang et al. (82) presented a new model using the Charnock constant based on the IEC standard. The study divides the sea state into three groups in terms of friction velocity:

- $u_* < 0.11m/s \Longrightarrow$ aerodynamically calm sea surface
- $0.11m/s < u_* < 0.26m/s \Longrightarrow$ transient sea state from calm to rough
- $0.26m/s < u_* \Longrightarrow$ completely rough sea state

In the study, the Charnock constant is set at 0.011 for calm sea, $0.016$ for transient sea, and $0.072$ for completely rough sea. Considering the extreme conditions, the constant was taken $0.072$. Equation 5.3 was solved implicitly with given inputs, and the

roughness was found to be $0.006$ meter. According to Equation 5.2, friction velocity ($u_*$) was calculated as $0.9066m/s$, and this value proves the completely rough sea state.

The relationship between the friction velocity and the longitudinal variance of the wind speed was defined by Stull (83) as follows:

$$\sigma_u^2 = 6.25 * u_*^2 \tag{5.4}$$

Turbulence intensity is found correspondingly by dividing the longitudinal variance by the mean wind speed,

$$TI = \frac{\sigma_u}{u} \tag{5.5}$$

The longitudinal variance and turbulence intensity were found 2.266 m/s, 11.33% respectively. Target Froude-scaled atmospheric boundary layer was obtained theoretically, can be seen in Figure 5.1, for our experiment.

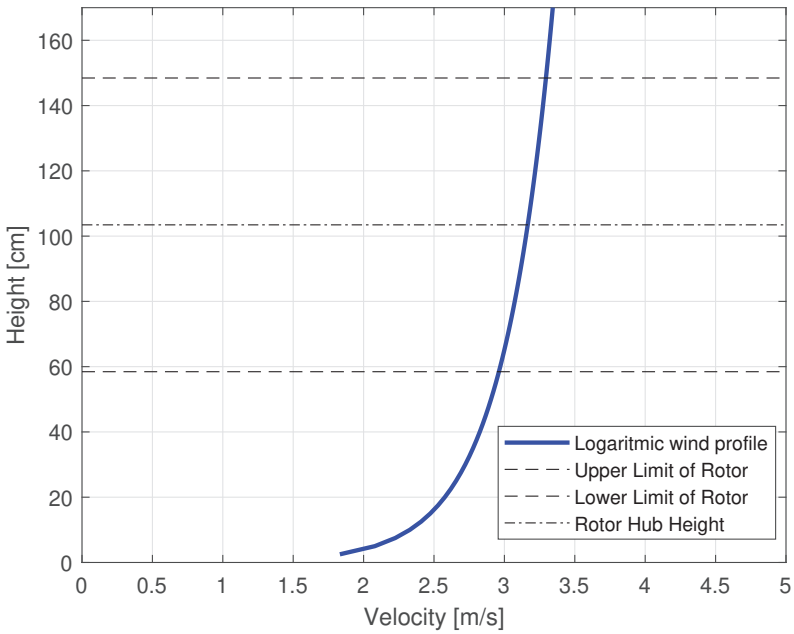


Figure 5.1. Froude-scaled logarithmic wind profile

**Performance Test of Wind Nozzle :** In order to understand the wind characteristics and to find optimum position for the FOWT, measurement tests were performed. D = 120 cm characteristic length was taken from the nozzle exit in the wind direction axis.

Three different fan performances for each position in 4 different positions were considered and data collected with the pitot tube. The origin point moved from sea level of the FOWT to sea level of the nozzle exit plane, and it is accepted as the origin point for this test.

The nozzle was placed at height of 155 cm from the ground. It has a length of 120 cm in the y-axis (y = -60: +60) and a length of 140 cm in the z-axis (z =155:295). The result of the measurements are given in the Figures below.

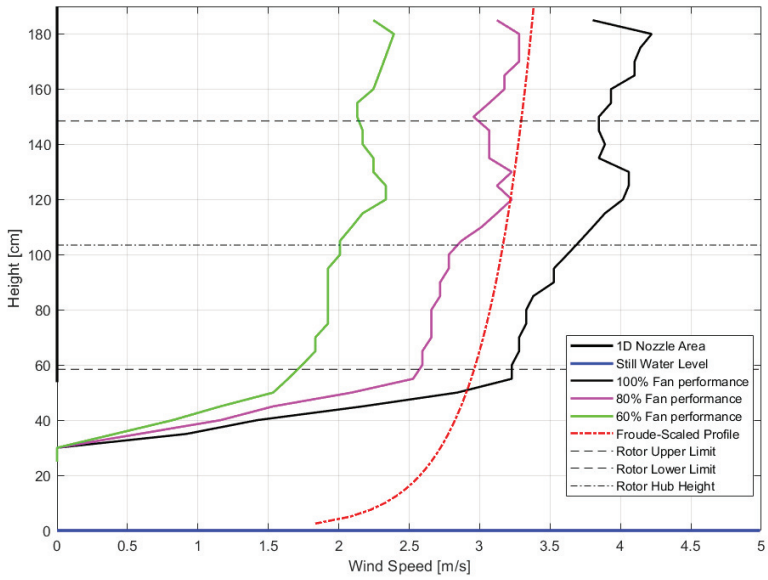


Figure 5.2. Measured wind profiles at x= 0.5D

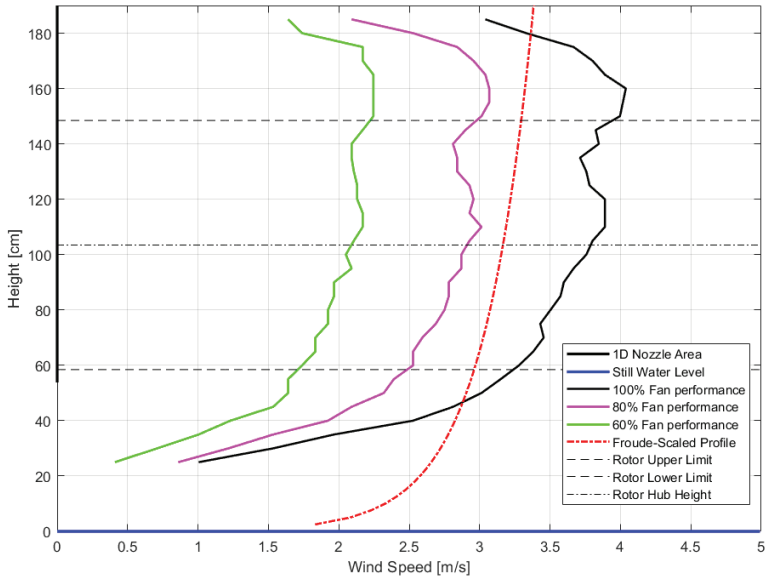


Figure 5.3. Measured wind profiles at x= 1D

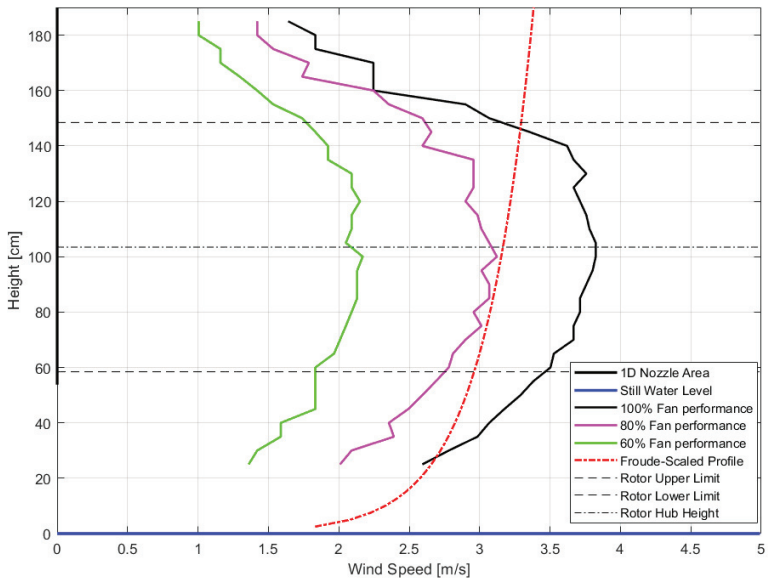


Figure 5.4. Measured wind profiles at x= 2D

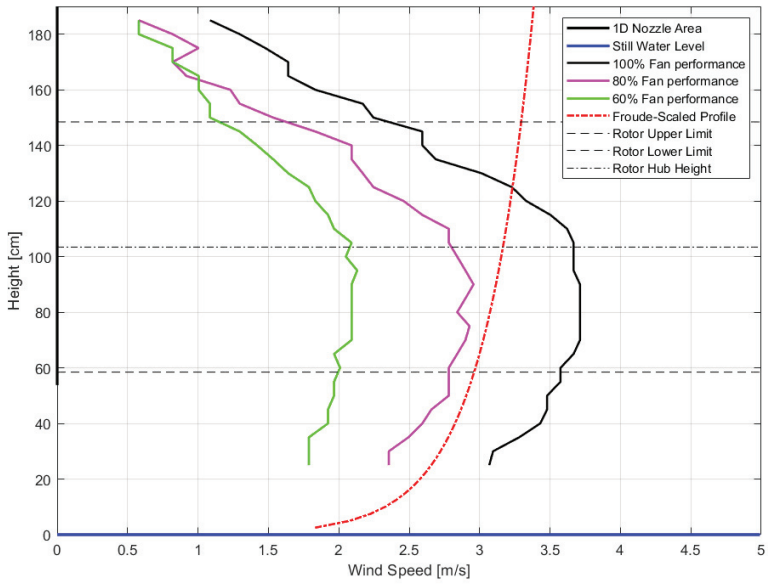


Figure 5.5. Measured wind profiles at x= 3D

As a result of the test, it was decided that the position at x=1D is the most suitable position for the wind turbine system. In order to bring this profile closer to the atmospheric boundary layer profile, different tests were considered as well.

A separate experiment was conducted to observe how homogeneously the flow on the turbine is distributed when looking in the direction of flow from the wind turbine. The Figures given below help to understand how homogeneous the flow is, especially in the Y axis. The experiment was carried out with the upper fans at 80% and the lower fans at 100% performance.

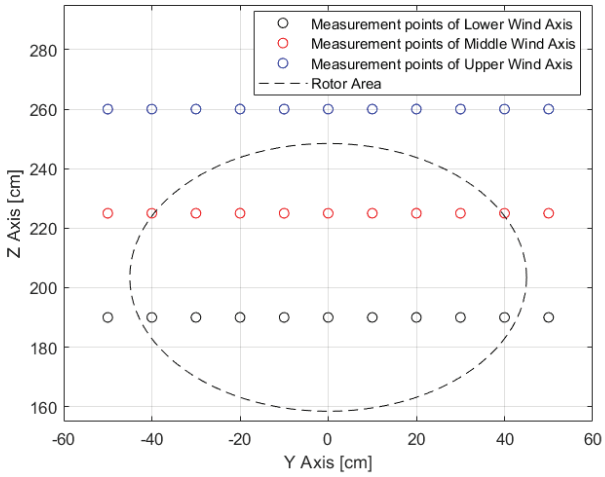


Figure 5.6. Measured wind points on y-z plane at x= 1D

In Figure 5.6, the coordinates of the points where measurements were taken from 120 cm (1D) away from the x-axis of the nozzle exit area are given. In addition, the rotor area projection on the nozzle exit plane is seen as circular. Wind speed measurements were taken at 11 points (-50:+50) at 10 cm intervals on the y-axis at z=190,225,260 cm heights. Measurements were taken 6 times in succession for each point.

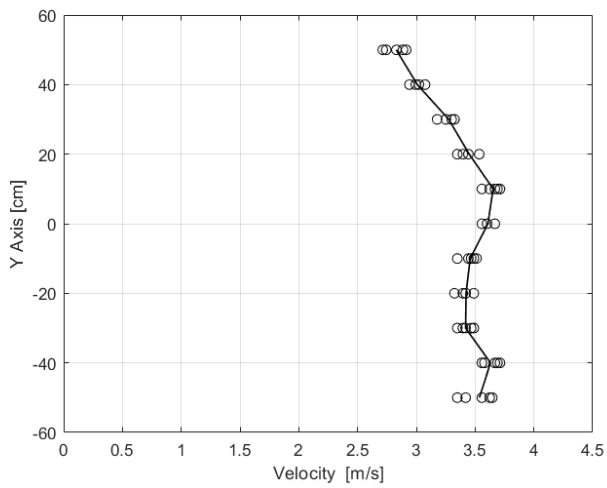


Figure 5.7. Wind profile at z=190 cm (o = Each measurement, black solid line = Average of measurements)

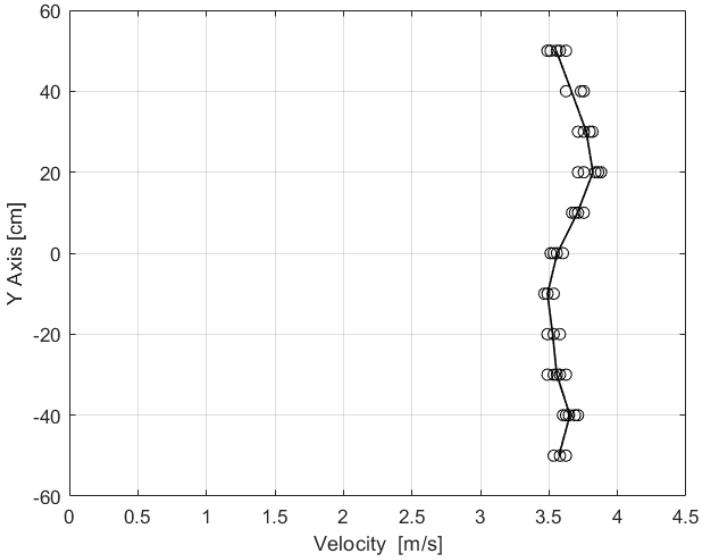


Figure 5.8. Wind profile at z=225 cm (o = Each measurement, black solid line = Average of measurements)

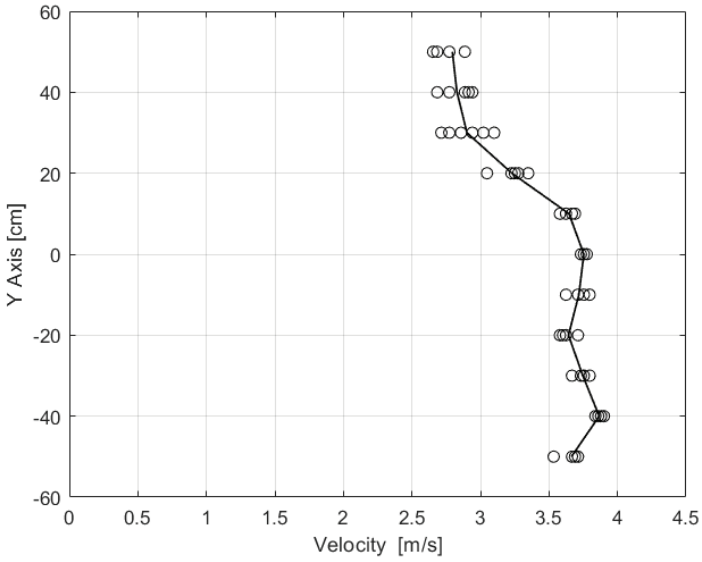


Figure 5.9. Wind profile at z=260 cm (o = Each measurement, black solid line = Average of measurements)

In Figure 5.7 and Figure 5.9, a decreasing trend in wind speed from y=+10cm to +50 is seen. In Figure 5.8 there is an almost homogeneous flow, except for the higher-than-average velocity profile between y=+10:+40. To solve this problem, three identical wing are placed in the nozzle.

As a result of the optimization studies, the profile closest to the desired wind profile was obtained when the lower fans and the upper fans were operated at 80.5% and 83% performance, respectively. The wind speed distribution in the rotor swept area is shown in Figure 5.10.

Atmospheric boundary layer is very important in terms of observing dynamic events such as overturning moment of the floating platform. The realistic case for the wind turbine can be achieved by using ABL.

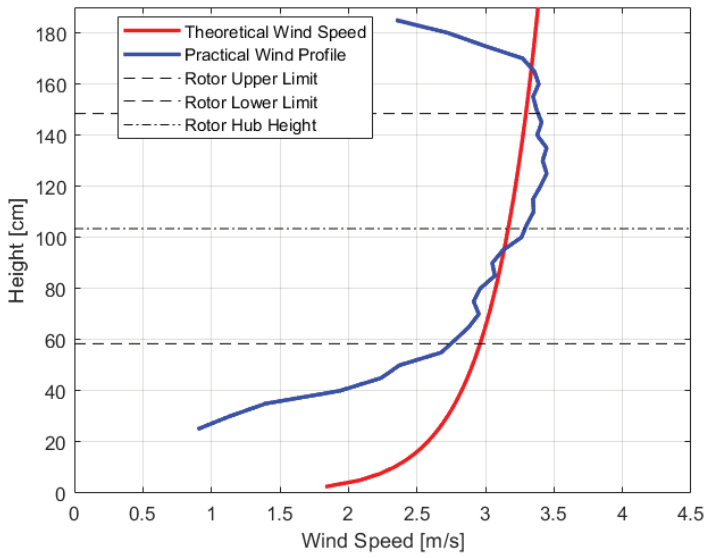


Figure 5.10. Experiment wind profile

The turbulence intensity was calculated, Figure 5.11, based on the hot-wire data which has 500 Hz sampling rate and 120 seconds long data were collected for each point. Figure 5.12 shows the difference between the wind profile that will create the rotor thrust and the desired wind profile. The maximum wind speed difference over the rotor sweep area was 0.213 m/s, the average wind speed difference was 0.03 m/s, and the average turbulence intensity was 14.78%. Although the in-homogeneous wind difference affects the moment of the system, as it can be understood from the average wind speed difference, the total thrust force coming from the rotor was provided with high accuracy.

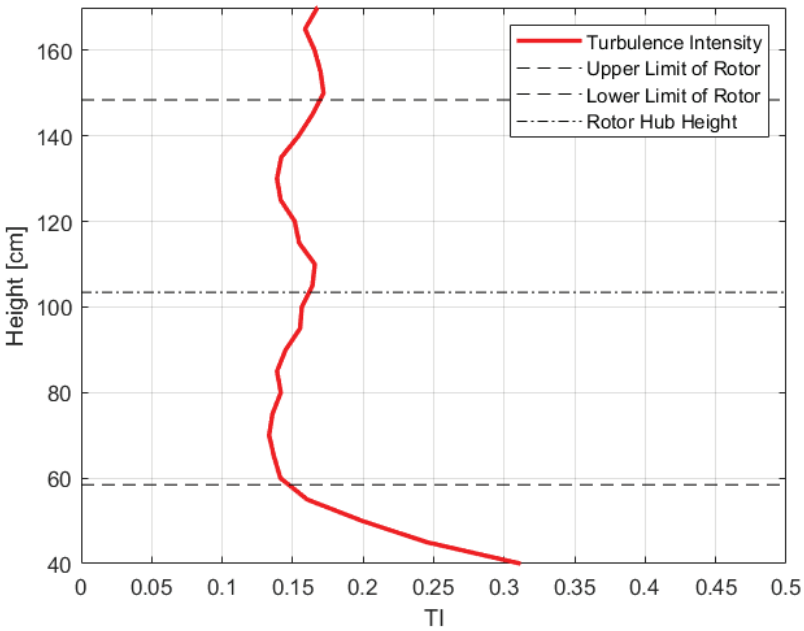


Figure 5.11. Turbulence intensity of wind profile

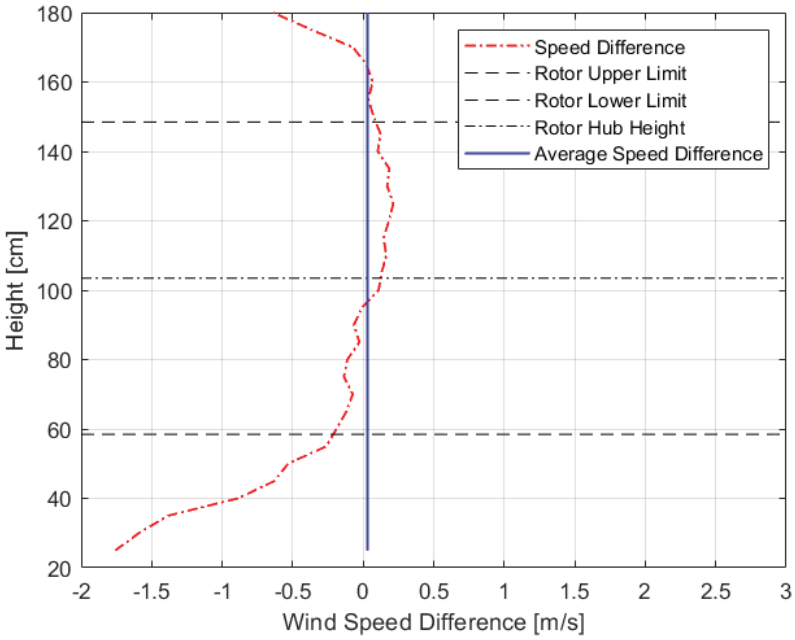


Figure 5.12. Wind speed difference over rotor swept area

## 5.2. Dynamic Tests

In the experiments, it was planned to take the wave height from 2 m to 12 m in the prototype, taking into account the wave height range that may occur in reality. To find the wave period corresponding to these wave heights, the wave steepness ”s”, which gives the relationship between the wave height and the wave period, was used. The wave steepness is given in Equation 5.6:

$$s = \frac{H}{gT^2/2\pi} \tag{5.6}$$

H is the wave height, T is the wave period, and g is the gravitational acceleration. As the wave steepness increases, the wave period gets shorter. Two different wave steepnesses of 0.02 and 0.04 were taken in the experiments. The steepness of 0.02 was used to see the effect of long-period waves, and the more encountered periods in nature was represented with 0.04 in the experiments. Increasing the wave steepness further was not considered since it causes wave breaks in the channel. The wave parameters and value ranges used in the experiments are given in Table 5.2.

Table 5.2. Full-scaled version of wave parameters of experiment

| **Parameter** | **Range** |
|---|---|
| Wave Height | 2 - 12 m |
| Wave Steepness | 0.02, 0.04 |
| Wave Period | 5.69 - 19.6 s |

Regarding the wave parameters, tests were carried out in the wave channel for wave-wind,only wind and only wave conditions. During the tests, the motion was captured by camera and post-processed through Tracker for the heave, pitch and surge degrees of freedom. The motion was decomposed with in-house MATLAB code. Thrust data was collected from the strain gauge which was attached to the bottom of tower. The results are given in next subsections.

### 5.2.1. Free Decay Tests

Free decay tests are performed by giving a certain initial translational or rotational displacements to the model in the wave flume and releasing the model. The model oscillates with gradually decreasing amplitude until it reaches the static equilibrium state. This set of experiments is important in terms of providing information about the damping characteristics of the model. Within the scope of these experiments, free decay tests with 3 degrees of freedom were applied (surge, pitch, and heave). Since the wave and wind come from one direction, the movement in other degrees of freedom is neglected in this study. The initial translational distances and rotational degree which applied in free damping tests are given in Table 5.3. The results are given in Figure 5.13.

Table 5.3. Initial displacement and angular values which applied in free decay test

| Degree of Freedom | Value |
|---|---|
| Surge | 23 cm |
| Pitch | 14° |
| Heave | -36 cm |

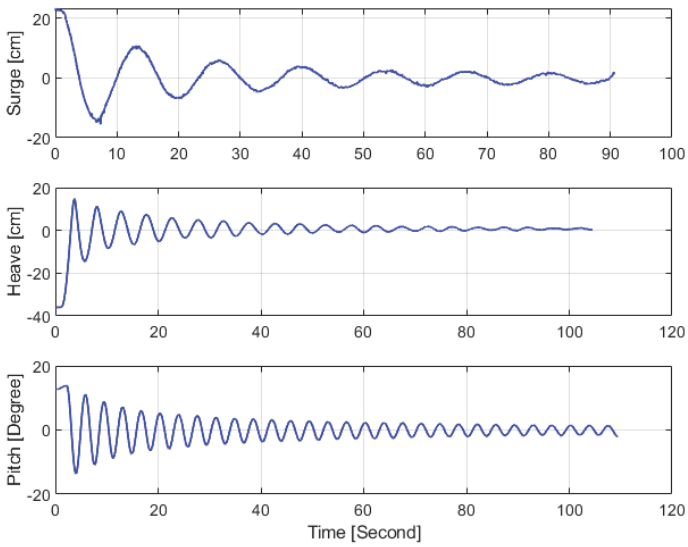


Figure 5.13. Free decay tests result in time domain

Fast Fourier Transform analysis was performed to find the natural frequency in each decay test for the individual degree of freedom. Since moored floating platforms are highly coupled systems, it is impossible to measure only one mode. Hence it contains the frequencies of other DoFs. Figure 5.14 shows single and coupled responses formed from surge, heave and pitch free decay tests. In the middle subfigure, it is seen that the heave response is coupled with pitch

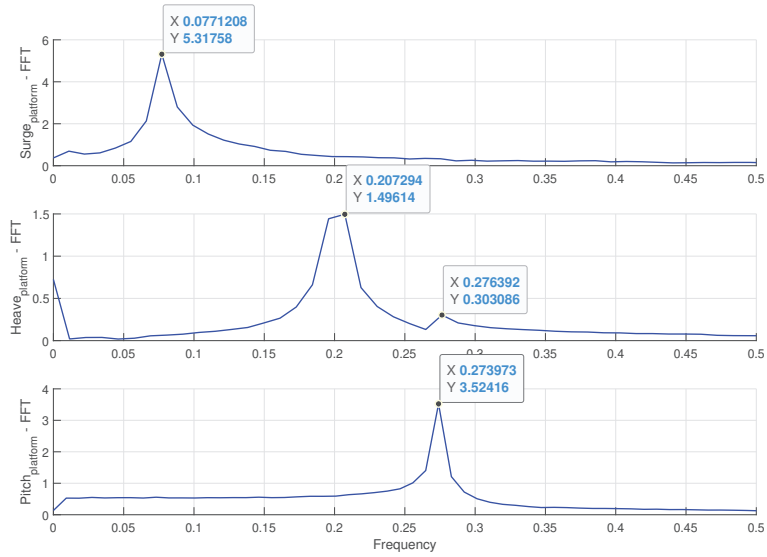


Figure 5.14. Free decay tests result in frequency domain

As a result of free decay tests, surge, heave, and pitch natural frequencies were calculated as 0.077 Hz, 0.2 Hz, and 0.276 Hz, respectively.

### 5.2.2. Only Wind Tests

In floating platforms, the aerodynamic thrust acting on the rotor gives the average additional pitch angle depending on the platform concept. Although this effect is diminished by the stability of the platform itself, secondly, the mooring lines tends to return to their initial state, it can result in a significant additional average pitch angle (47). In order to observe the dynamics created by these effects on the system, experiments were carried out under the atmospheric boundary layer.

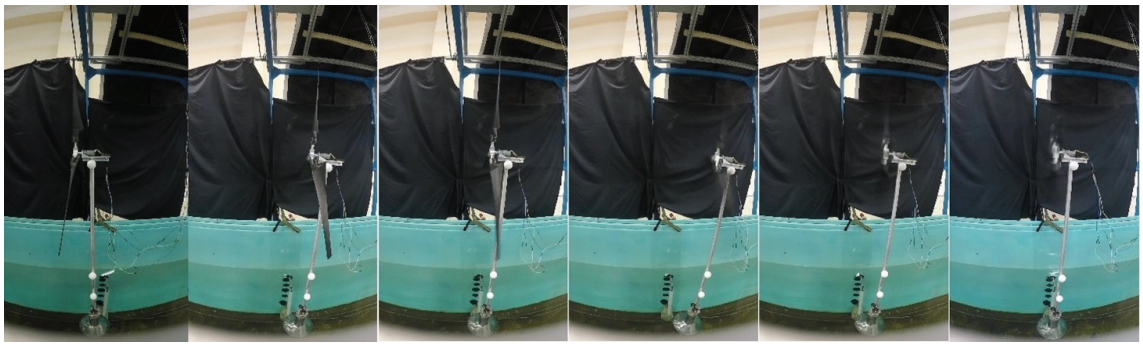

Figure 5.15. Only wind test, from left to right : 1. Initial position, 2. Position under the wind, 3. Enhanced position by mooring lines, 4. Rotor starts to rotation, 5. Transient state between starting of rotation and max rpm, 6. Position when the rotor at max rpm.

The behavior of the system can be seen step by step during the experiments in Figure 5.15. With occurrence of the wind, the drag force causes the surge. The logarithmic profile exerts more force on the upper half of the rotor,thus, the pitch angle and draft of the system was increased. The longitudinally shifted platform tended to return to its initial state by tension of mooring lines. The working moment of the rotor creates transient state, instead of extracting energy from the flow, it gives energy to the flow. Hence, maximum surge and pitch angle were occurred. The rotor was accelerated gradually until it reaches the desired rpm value, and steady state. In the final state, there were +3 cm surge, -1.2 cm heave, +1.35° pitch angle differences from the initial position. The strain gauge results shows that the thrust force values acting on the tower vary between -0.2 N and 0.9 N. However,the average thrust force was found to be 0.29 N.

### 5.2.3. Wind and Regular Wave Tests

The wave parameters of model were determined by preliminary tests in regular wave experiments. The wave heights and periods used in the experimental tests are given in Table 5.4. The test are named according to the full-scaled value of the wave height and the wave steepness. For example, the experimental condition of wave height of 4 m and wave steepness of 0.02 is called D-H4-T02.

Table 5.4. Parameters of regular wave of the tests

| Test name | Height [cm] | Period [s] | Steepness |
|---|---|---|---|
| D-H2-T02 | 4.88 | 1.22 | 0.2128 |
| D-H4-T02 | 10.16 | 1.79 | 0.2058 |
| D-H6-T02 | 15.66 | 2.19 | 0.2119 |
| D-H8-T02 | 19.77 | 2.53 | 0.2004 |
| D-H10-T02 | 24.98 | 2.82 | 0.2038 |
| D-H12-T02 | 29.8 | 3.1 | 0.2012 |
| D-H2-T04 | 5.17 | 0.9 | 0.4142 |
| D-H4-T04 | 9.65 | 1.26 | 0.3945 |
| D-H6-T04 | 14.82 | 1.55 | 0.4003 |
| D-H8-T04 | 19.79 | 1.77 | 0.4099 |
| D-H10-T04 | 24.92 | 2 | 0.4043 |
| D-H12-T04 | 29.5 | 2.09 | 0.4383 |

The regular wave that propagate along the flume loses most of its energy by breaking at the dissipation beach, but as determined by the preliminary studies, about 12% is reflected back from the end of channel. The waves which reflected from the end are directed towards the end of the channel by reflecting again from the wave maker. This event continues for each wave until the wave loses its energy completely, and leads to distorted wave propagation. Therefore, duration time for regular wave experiments was determined as about 60 seconds at most.

The measurements collected from the wave gauge sensor during regular wave experiments are given in Figure 5.16, where it is seen that harmonic frequencies occur in the wave flume at multiples of the incident wave frequency during the regular wave experiment. Consequently, this situation appears as harmonic frequencies in the results of regular wave experiments.

After turned on the fans of the nozzle, regular wave tests were repeated under the extreme wind. The experiments were carried out by rotating the blades at 316 rpm. The positions obtained by processing the video recordings were separated into surge, heave and pitch movements. The results are given in Figures 5.17-5.28.

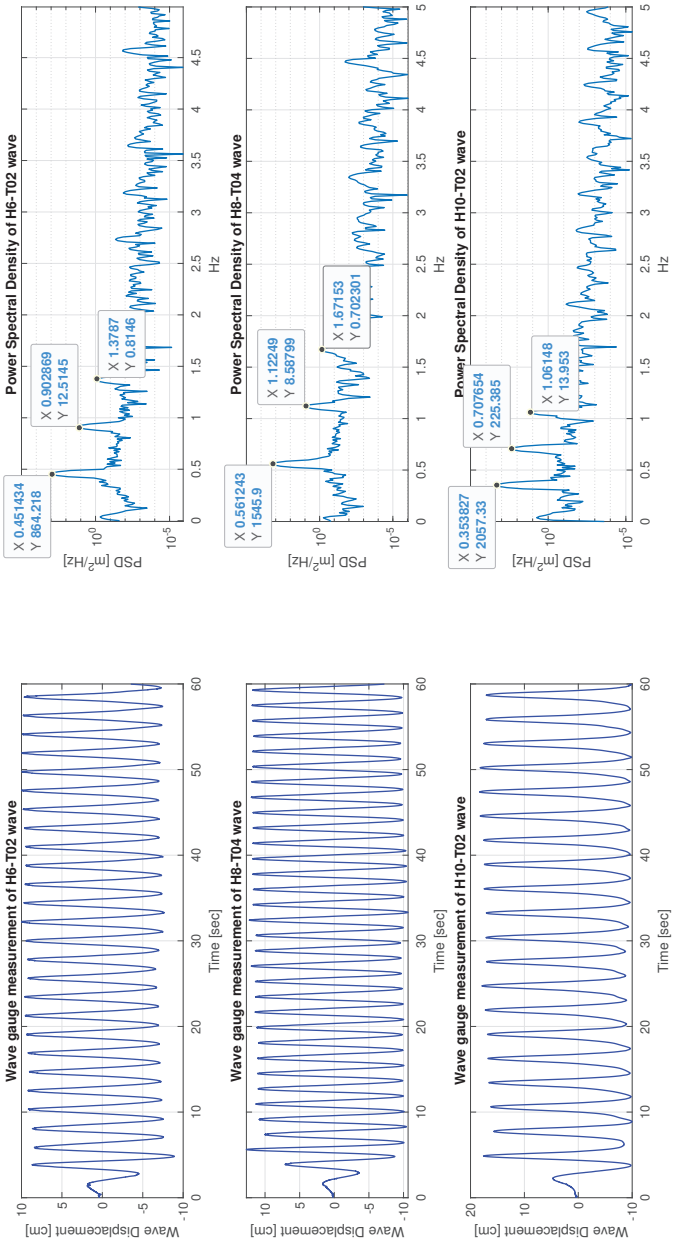


Figure 5.16. Time series and PSD of measured data from wave gauge during various wave experiments

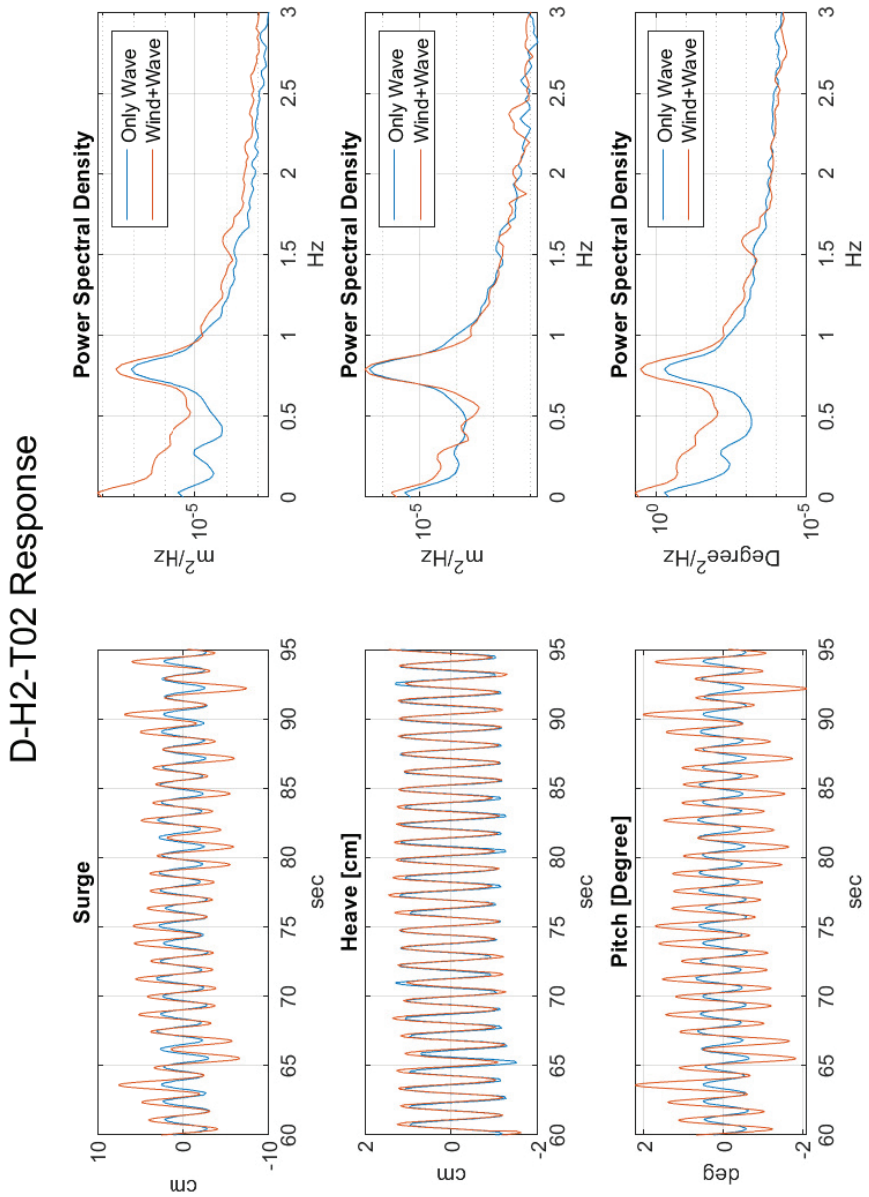


Figure 5.17. Power spectral densities and time series of surge, heave, pitch motions of D-H2-T02-Test

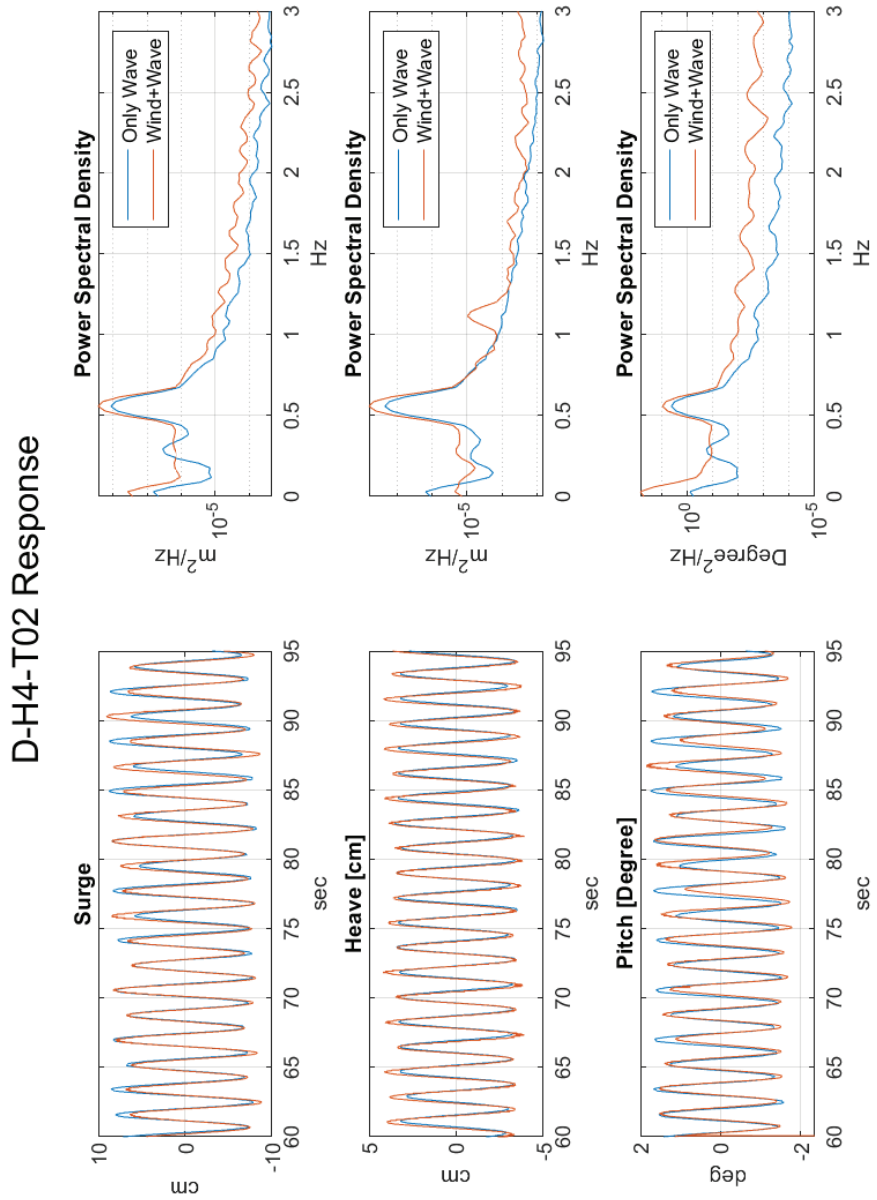


Figure 5.18. Power spectral densities and time series of surge, heave, pitch motions of D-H4-T02-Test

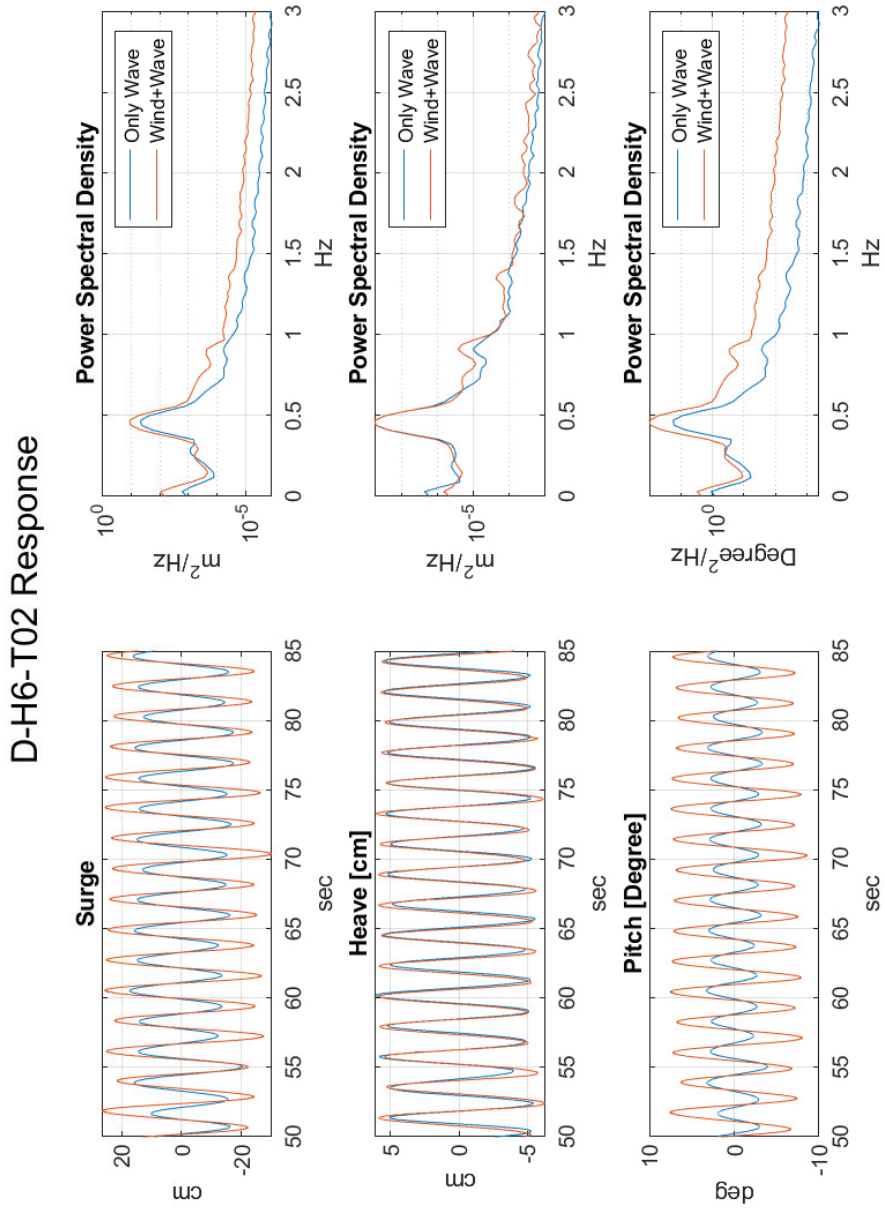


Figure 5.19. Power spectral densities and time series of surge, heave, pitch motions of D-H6-T02-Test

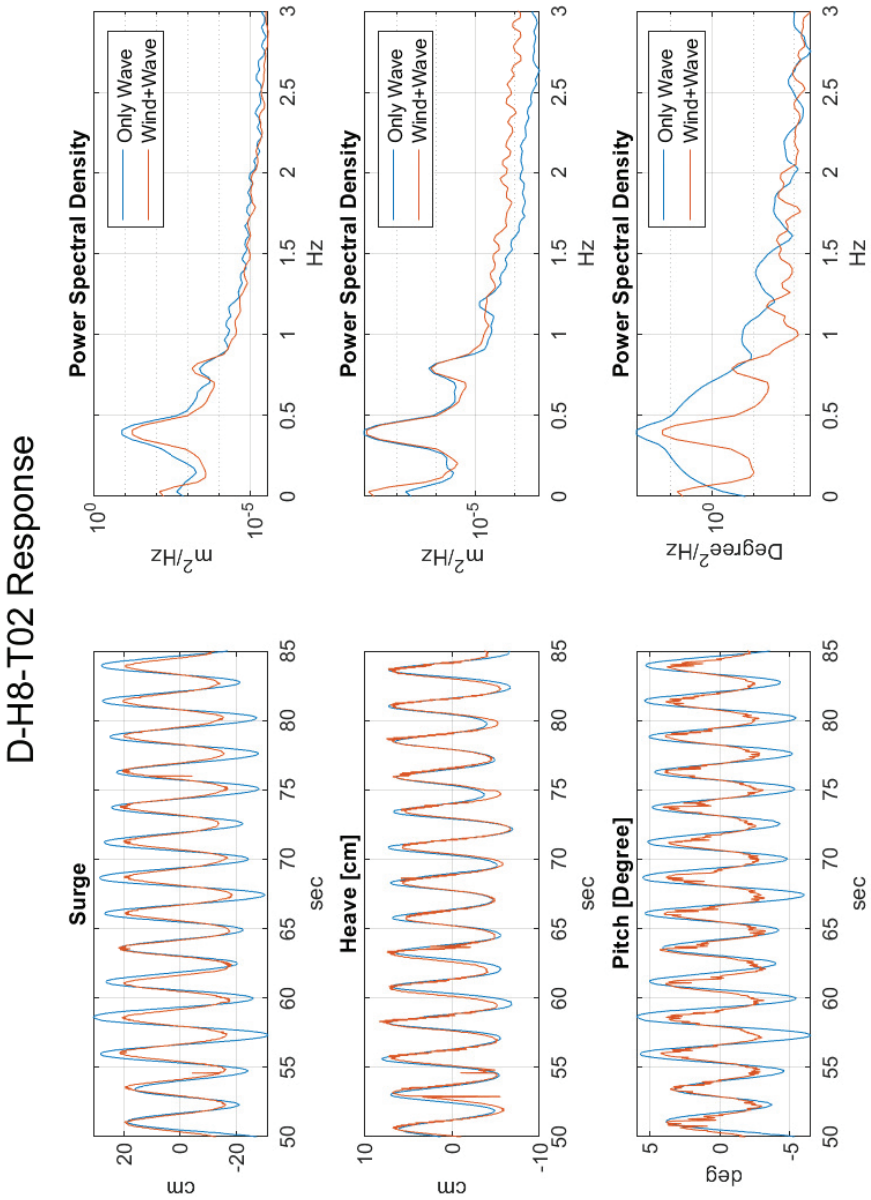


Figure 5.20. Power spectral densities and time series of surge, heave, pitch motions of D-H8-T02-Test

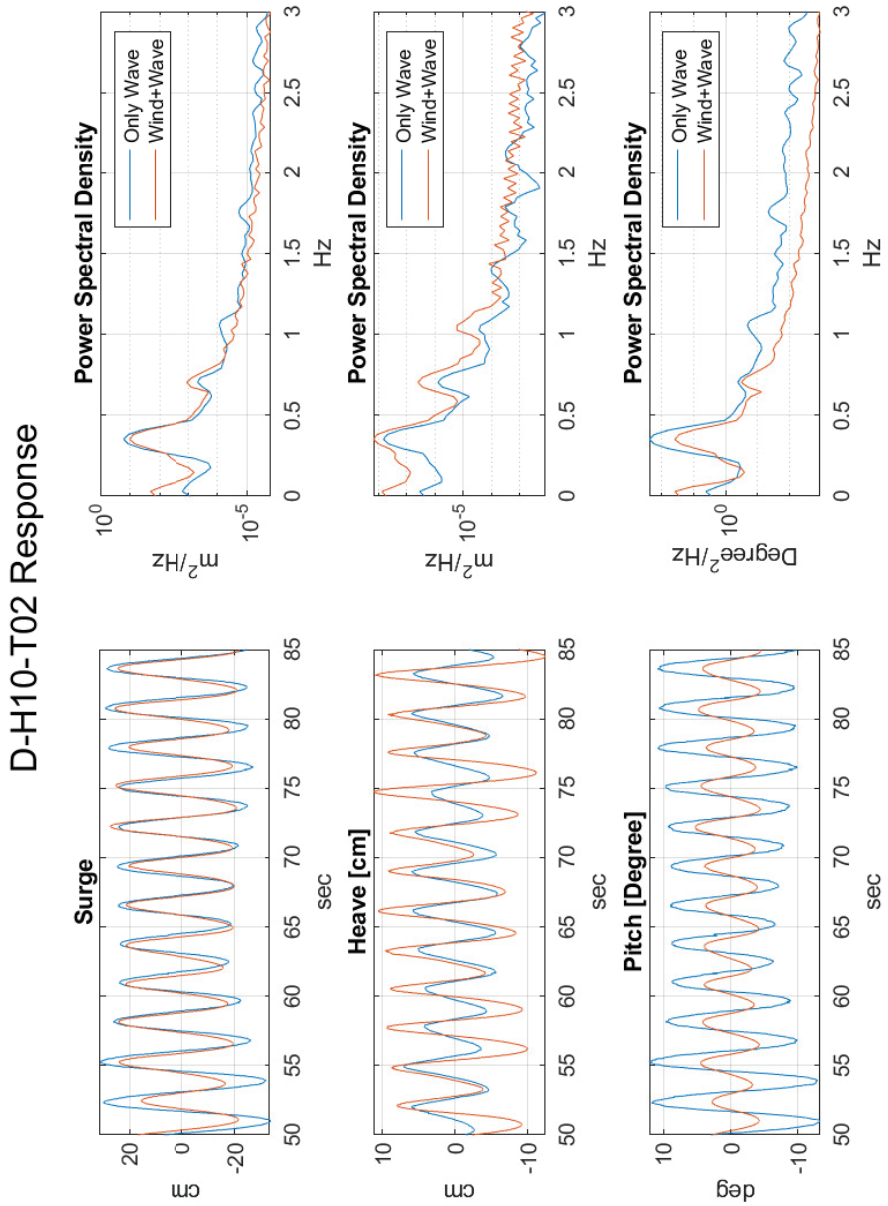


Figure 5.21. Power spectral densities and time series of surge, heave, pitch motions of D-H10-T02-Test

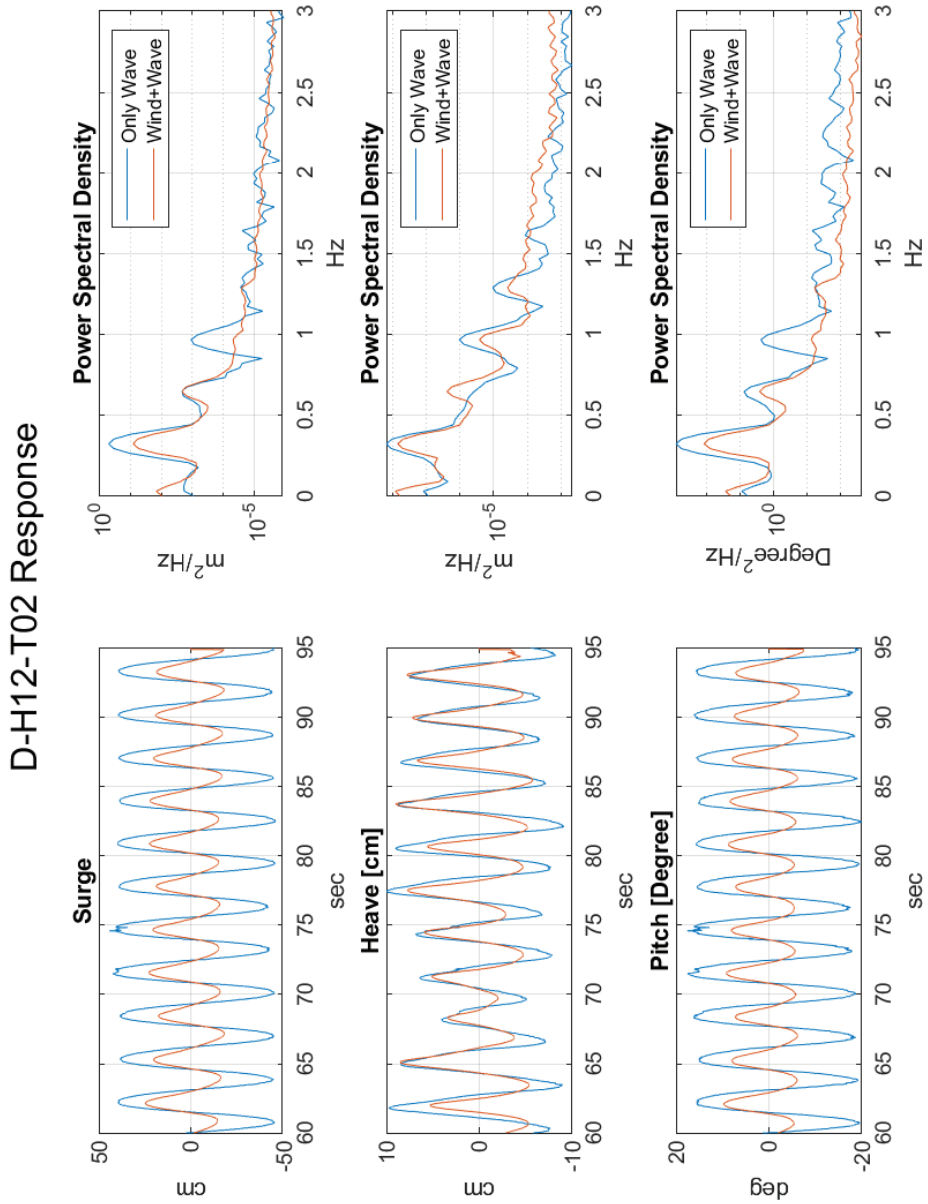


Figure 5.22. Power spectral densities and time series of surge, heave, pitch motions of D-H12-T02-Test

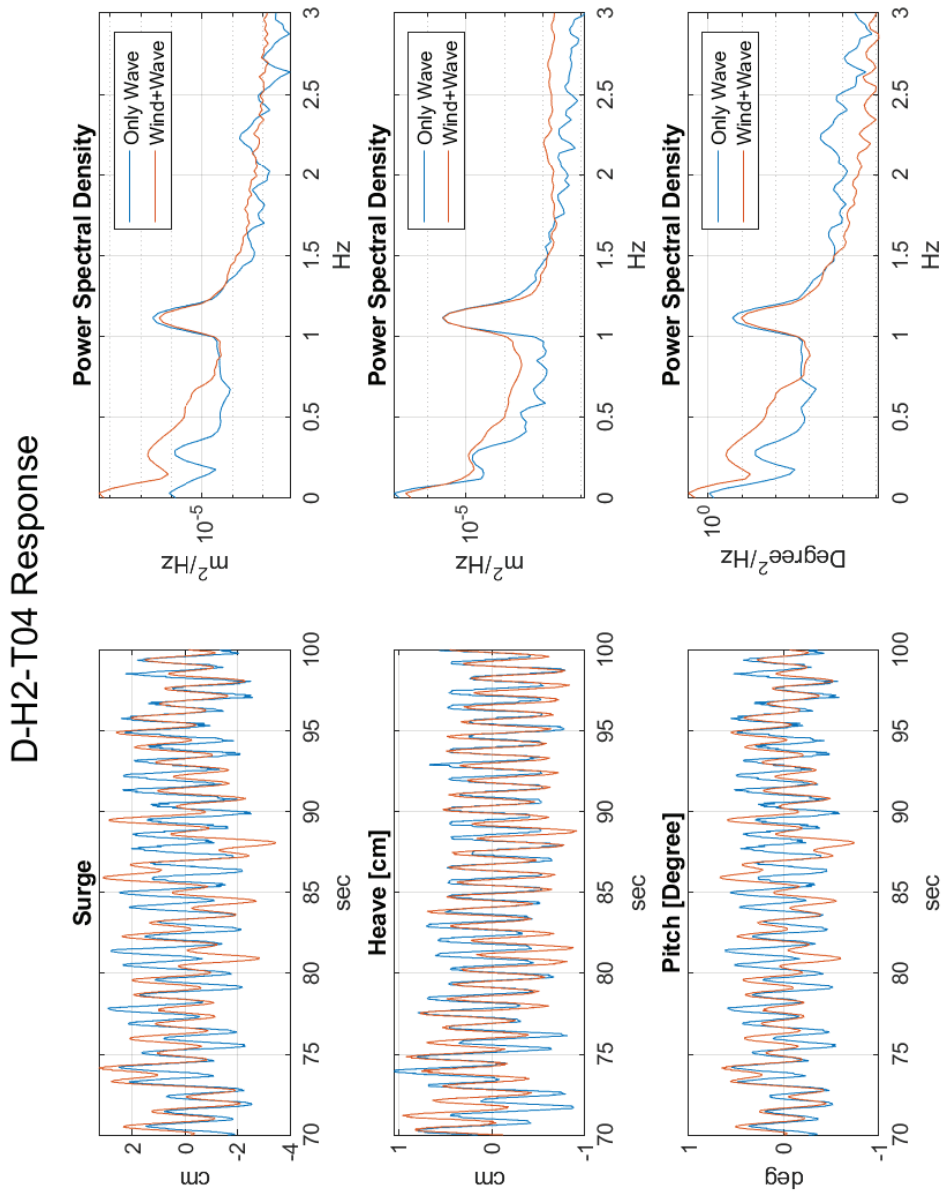


Figure 5.23. Power spectral densities and time series of surge, heave, pitch motions of D-H2-T04-Test

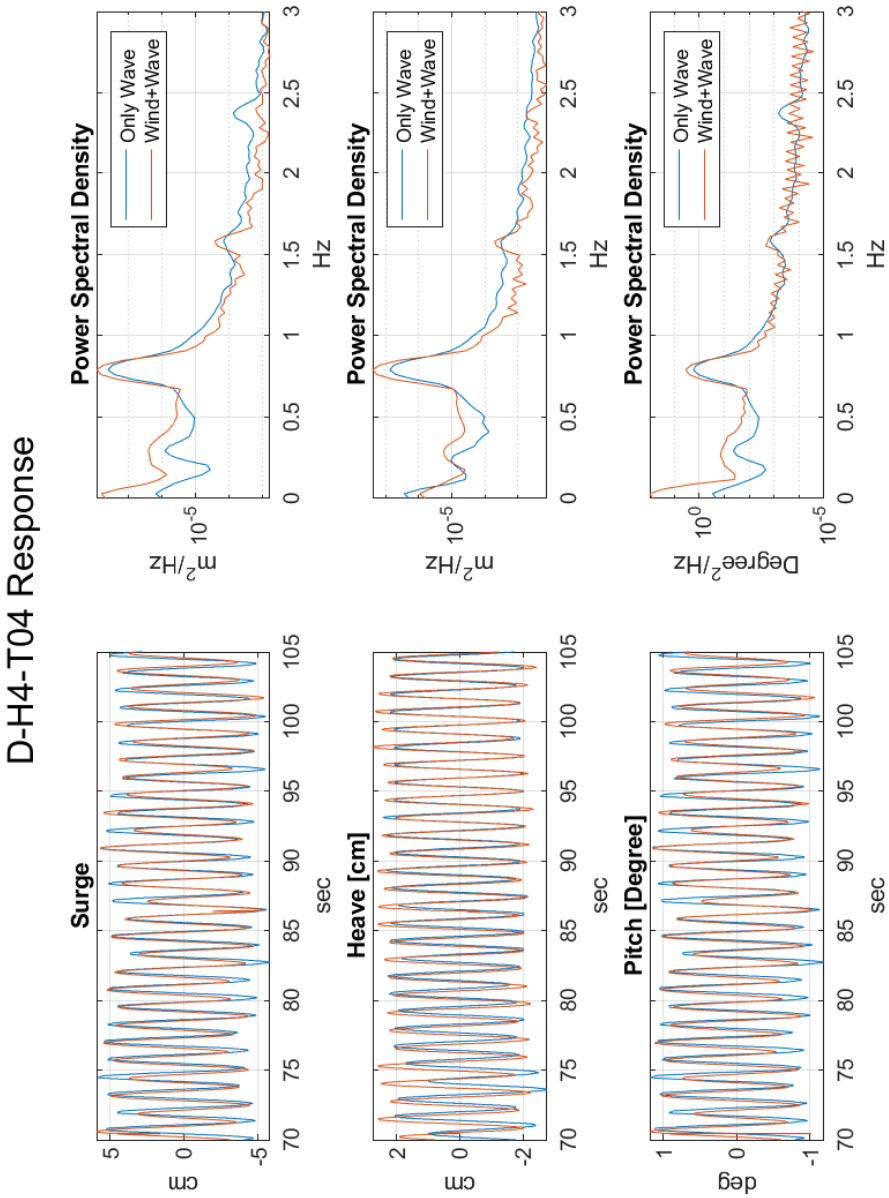


Figure 5.24. Power spectral densities and time series of surge, heave, pitch motions of D-H4-T04-Test

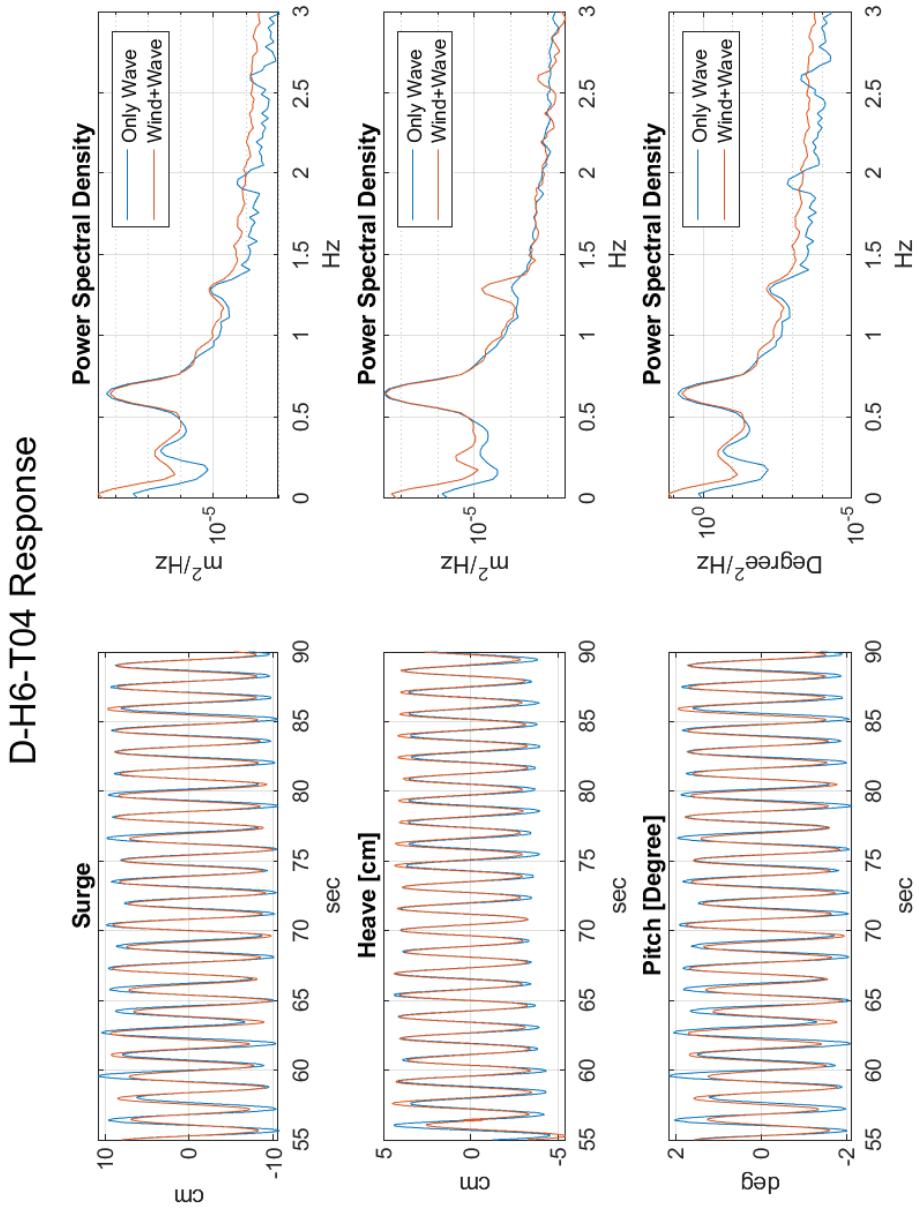


Figure 5.25. Power spectral densities and time series of surge, heave, pitch motions of D-H6-T04-Test

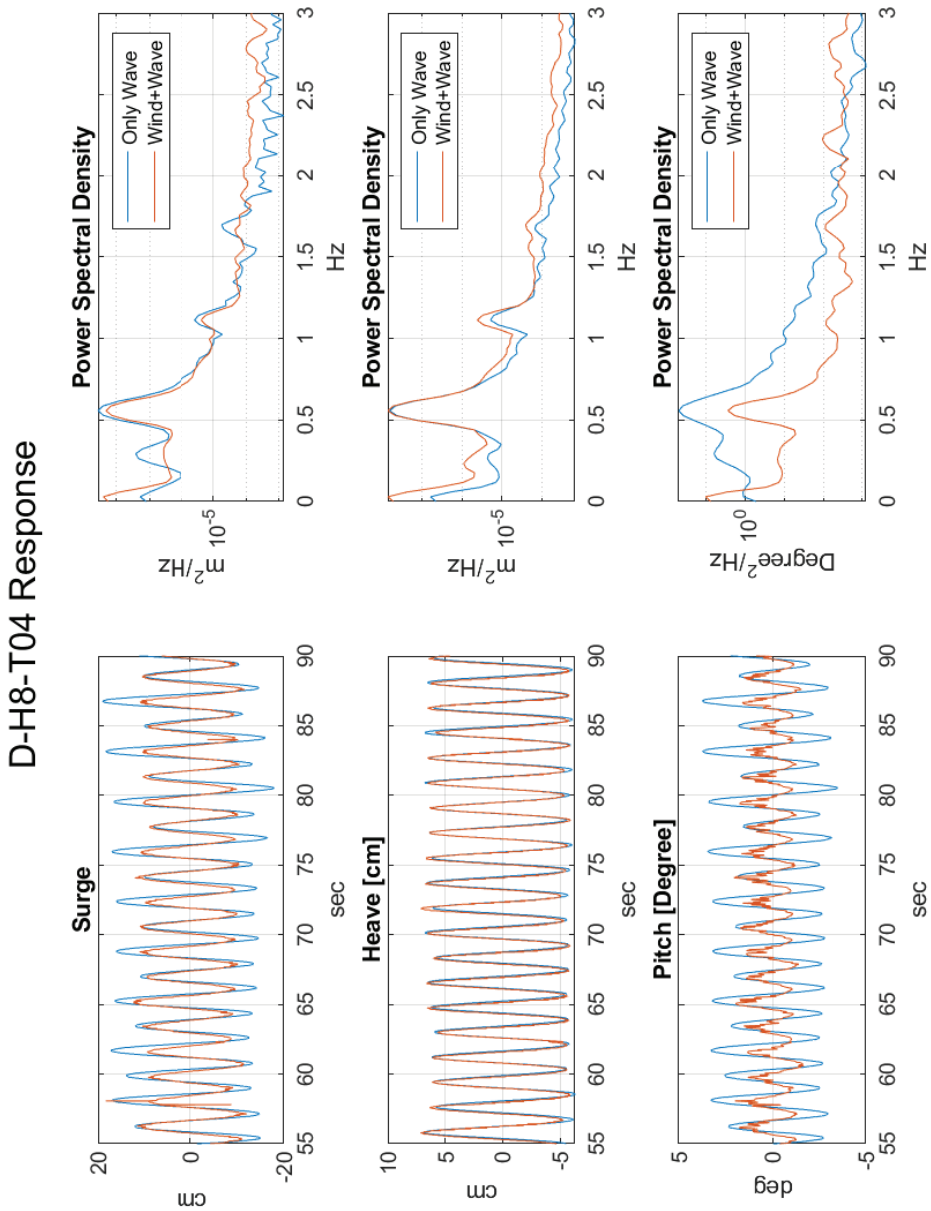


Figure 5.26. Power spectral densities and time series of surge, heave, pitch motions of D-H8-T04-Test

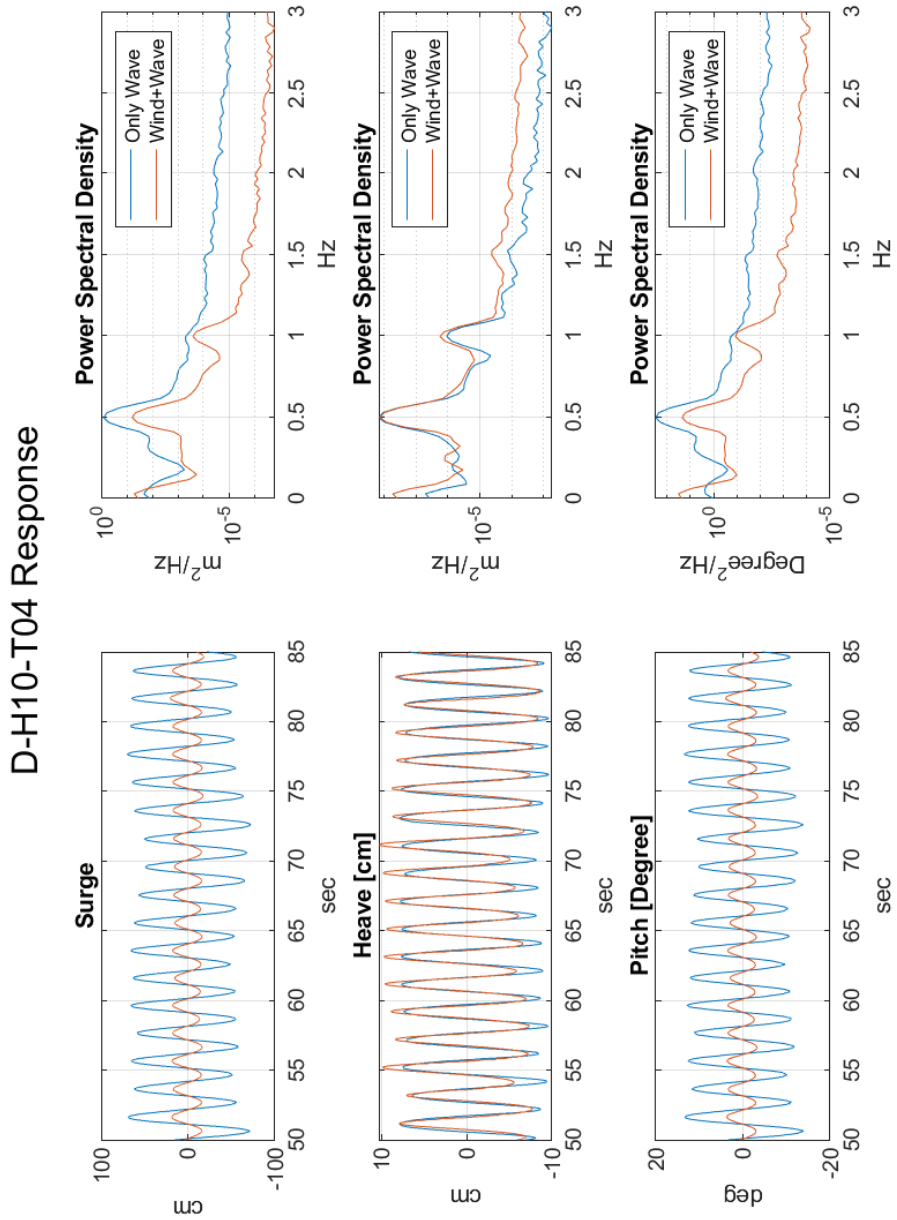


Figure 5.27. Power spectral densities and time series of surge, heave, pitch motions of D-H10-T04-Test

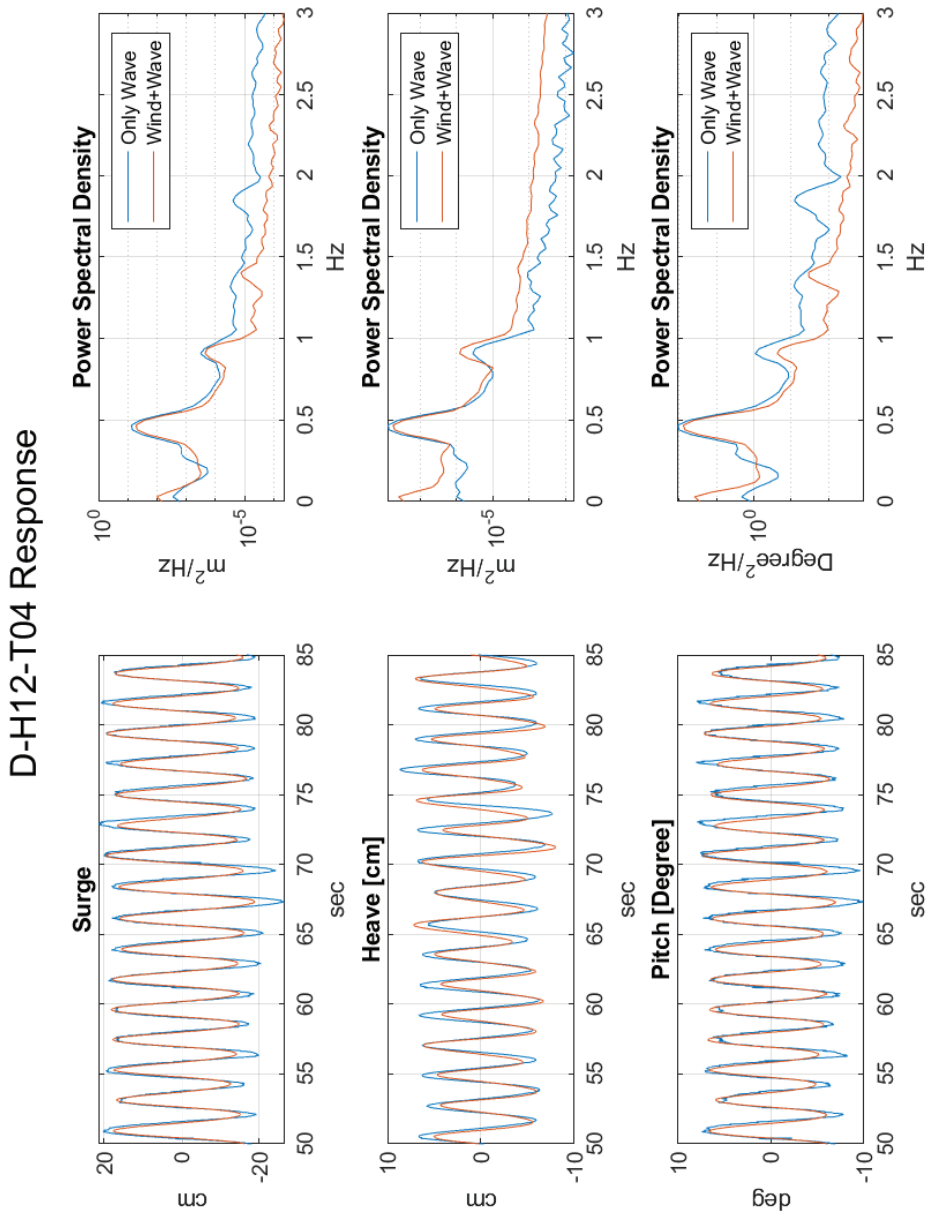


Figure 5.28. Power spectral densities and time series of surge, heave, pitch motions of D-H12-T04-Test

### 5.2.4. Wind and Irregular Wave Tests

Irregular waves are synthesized by sea state spectrums such as JONSWAP and Pierson-Moskowitz. Displacement values are obtained as time series by inverse Fourier transform and sent as inputs to the wave maker within the scope of experiments. In the literature, it has been suggested that these time series should be long enough to cover 1000 waves for sensible desired spectral properties. Moreover, the data acquisition frequency of the wave-meter should be sufficient to measure at least 10 discrete data points of one wave (84). For example, the test duration of irregular wave series ,which have average period of 1 s, must be at least 1x1000=1000 s, and the sampling frequency of the wave-meter must be at least 10Hz.

It has been observed that the wave generator stops the motor by touching the limit switches during the production of some extreme waves in the series, which have high wave heights. Considering these constraints, only one wave condition were performed in the channel. The number of data has been chosen as $2^n = 4096$ to facilitate power spectral density calculations to be used in the processing of wave data.

The preliminary studies of irregular waves were completed in the channel. The obtained data were processed with written Python code. Both the time-dependent and the frequency-dependent data were examined, and the frequency-dependent spectrum was extracted and compared with the spectrum of the theoretical wave. The result shows that, wave maker can achieves the desired irregular wave.

The D-H8-T04 test condition was tested under the only wave and wind + wave conditions. The power spectral density of the motion are shown in Figure 5.29.

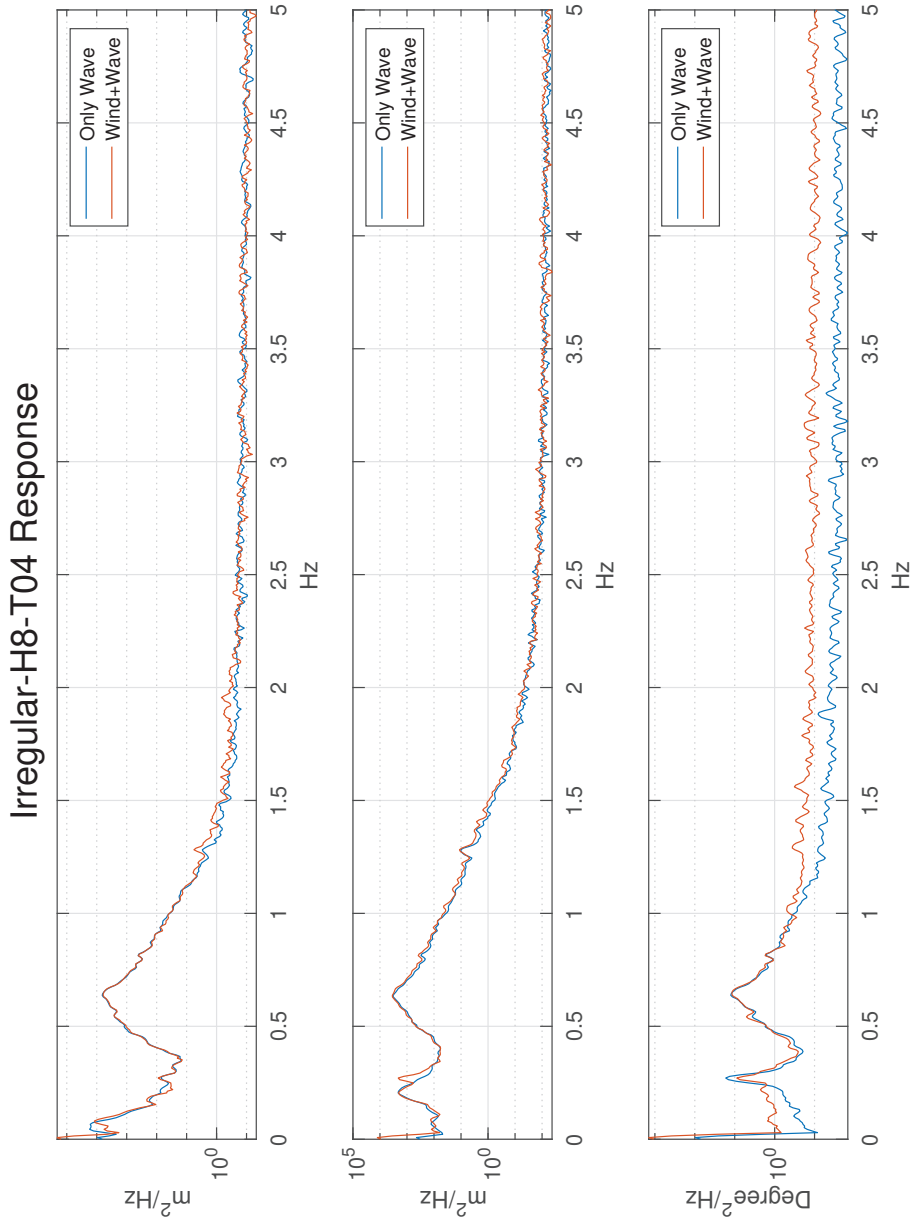


Figure 5.29. Power spectral densities of surge, heave, pitch motions of Irregular-H8-T04-Test

# CHAPTER 6

# CONCLUSION, DISCUSSION AND FUTURE STUDIES

## 6.1. Conclusions

Within the scope of the thesis, the dynamic behavior of the turbine system in extreme wind and various wave conditions was investigated by using the Froude-scaled model of Northel Poyra P36/300 turbine and spar type floating platform. An accurate geometric, dynamic and kinematic similarities are vital in the experiment. In this context, the consistency of the pitot tube was measured at low wind speeds for wind nozzle characterization. The hot-wire sensor has been calibrated with this pitot tube to investigate the wind characteristics in more detail. Electrical and computer connection of the traverse mechanism has been established and it has been made ready for hot-wire and pitot tube. The atmospheric boundary layer profile that should come to the turbine was calculated theoretically by considering the IEC standard. As a result of the measurements, it was decided that the first nozzle was not suitable for the desired wind profile, and the new nozzle was designed. After the new nozzle was produced, measurements were taken at various distances and fan performances for the desired atmospheric boundary layer profile and the most appropriate distance was selected. Optimization studies were carried out to achieve the most accurate profile in 1D, which is the most suitable distance. While the lower fans were operating at 80.5 percent and the upper fans at 83 percent, great accuracy has been achieved with average of 0.03 m/s difference from the desired wind over the rotor sweep area.

In order to achieve dynamic similarity, the weight and center of gravity of the each components are important. The ballast of the spar platform was calculated theoretically considering this situation, and as a result of the experimental studies, the sand-pebble mixture was placed in the spar and the steel plate was placed under the spar, and the model matched with design requirements.

Image processing method was chosen to collect system motion data. In the image processing method, both the in-house code developed in python and the open source

Tracker program used, which is common program in both academy and industry. As a result of the preliminary studies, it was seen that the results of the two programs matched each other and the experiments were analyzed with Tracker, which is easier to use. For the RGB algorithm of the Tracker, a black curtain was hung behind the turbine system and 3 red ping-pong balls were attached to the turbine for detection of the ping-pong balls in program. The total motion obtained as a result of the program was divided into degree of freedoms with the in-house code written in Matlab, and the results were obtained.

Within the scope of dynamic test, free decay tests, only wind tests, only wave tests and wind + wave tests were carried out. The damping characteristics of the displacements and rotations in the model matched the theory and provided preliminary validation in terms of dynamic behavior. Only wind tests were carried out to measure the thrust force. The average thrust force was measured as 0.29 N, that providing high match with the numerical analysis. In order to see the effect of the wind on the oscillation of the floating platform, the system was first subjected to wave tests only, and then the same wave conditions were repeated under the extreme wind.

A combination of 6 different wave heights and 2 different wave periods, 12 different regular waves and one irregular wave test were conducted. Studies show that hydrodynamic forces have dominant role on floating wind turbine oscillation. On the other hand, aerodynamic forces changes only the amplitude of these oscillations. While the wind increases the oscillation in the system at low wave heights, it is seen that the wind dampens the oscillation as the wave height increases.

## 6.2. Discussion and Limitation of the Tests

Although using the wave flume instead of wave basin brings novelty, the wave flume constrains the experiment. Using a scale factor greater than 40 greatly reduces the weight of the scale model and limits both production and the sensors to be used. A turbine model with a scale factor of less than 40 does not fit into the flume dimensions. Because of these limitations, obtaining the model weight was taken as a priority. Although the overall center of gravity matched, the weight distribution on a component basis did not match due to the manufacturing issues. Since it is very difficult to place a sensor on the turbine in terms of weight distribution, motion tracking was done with image processing. Moreover, the strain gauge was placed at the bottom of the tower to measure the thrust

force. In terms of applicability, only one atmospheric boundary layer has been created. The experimental tests cover the situations where the wind and the wave come in the same direction.

## 6.3. Recommendation for Future Studies

In nature, wind and waves usually do not come from the same direction. Therefore, expanding the experimental work on various wave directions can represent better real-world scenarios. Analyzing the dynamic behavior of the turbine with a fixed system consisting of more than one camera and accelerometers to be placed on the floating platform will increase both the scope and accuracy of the study. In future studies, the operation can be expanded under various operation conditions by increasing the number of wind profiles. In real world, wind turbines actively change the pitch angle of the blades according to the wind speed. Using active pitch sensors together with the controller on the turbine will provide better aerodynamic loads that expected from the rotor during the experiment.

# REFERENCES


[1] (2022). ”wind energy data”. `https://www.irena.org/wind`.

[2] Castro-Santos, L. and V. Diaz Casas (2015, 07). *”Floating Offshore Wind Farms and Their Application in Galicia (NW Spain)”*, pp. 455–465.

[3] (1993). *”Wind resources part I: The European wind climatology In A. D. Garrad, W. Palz, S. Scheller (Eds.)”*, Bedford. H.S. Stephens and Associates.

[4] GWEC (2022a). ” floating offshore wind – a global opportunity”.

[5] Sebastian, T. and M. Lackner (2012). ”development of a free vortex wake method code for offshore floating wind turbines”. *Renewable Energy 46*, 269–275.

[6] Martin, H. (2011, 12). *”Development of a Scale Model Wind Turbine for Testing of Offshore Floating Wind Turbine Systems”*.

[7] Tran, T. and D.-H. Kim (2015, 07). ”the platform pitching motion of floating offshore wind turbine: A preliminary unsteady aerodynamic analysis”. *Journal of Wind Engineering and Industrial Aerodynamics 142*.

[8] Lomholt, A. K. (2019). ”numerical study in bhawc and validation against experimental data of a model scaled 10 mw floating wind turbine with active pitch control using the tetraspar floater”. Master’s thesis, Lyngby Denmark.

[9] Branlard, E. (2017, 01). *”Wind Turbine Aerodynamics and Vorticity-Based Methods”*, Volume 7.

[10] Matha, D., J. Cruz, M. Masciola, E. Bachynski-Polić, M. Atcheson, A. Goupee, S. Gueydon, and A. Robertson (2016a, 08). *”Modelling of Floating Offshore Wind Technologies”*, pp. 133–240.

[11] Goupee, A., B. Koo, R. Kimball, K. Lambrakos, and H. Dagher (2012, 07). ”experimental comparison of three floating wind turbine concepts”. Volume 136.

[12] Robertson, A., J. Jonkman, A. Goupee, A. Coulling, I. Prowell, J. Browning, M. Masciola, and P. Molta (2013, 06). ”summary of conclusions and recommendations drawn from the deepcwind scaled floating offshore wind system test campaign”.

[13] Kimball, R., A. Goupee, M. Fowler, E.-J. Ridder, and J. Helder (2014, 06). ”wind/wave basin verification of a performance-matched scale-model wind turbine on a floating offshore wind turbine platform”. Volume 9, pp. V09BT09A025.

[14] Pegalajar-Jurado, A., A. Hansen, R. Laugesen, R. Mikkelsen, M. Borg, T. Kim, N. Heilskov, and H. Bredmose (2016, 09). ”experimental and numerical study of a 10mw tlp wind turbine in waves and wind”. *Journal of Physics: Conference Series 753*, 092007.

[15] Roddier, D., C. Cermelli, A. Aubault, and A. Weinstein (2010, 05). ”windfloat: A floating foundation for offshore wind turbines”. *Journal of Renewable and Sustainable Energy 2*.

[16] Azcona, J., F. Bouchotrouch, M. González, J. Garciandía, X. Munduate, F. Kelberlau, and T. Nygaard (2014, 06). ”aerodynamic thrust modelling in wave tank tests of offshore floating wind turbines using a ducted fan”. *Journal of Physics: Conference Series 524*, 012089.

[17] Bachynski-Polić, E., M. Thys, T. Sauder, V. Chabaud, and L. Sæther (2016, 06). ”real-time hybrid model testing of a braceless semi-submersible wind turbine: Part ii — experimental results”. pp. V006T09A040.

[18] Bayati, I., A. Facchinetti, A. Fontanella, H. Giberti, and M. Belloli (2018, 06). ”a wind tunnel/hil setup for integrated tests of floating offshore wind turbines”. *Journal of Physics: Conference Series 1037*, 052025.

[19] Alkarem, Y. (2020). ”numerical examination of floating offshore wind turbine and development of an innovative floating platform design”. Master’s thesis, Izmir.

[20] Doerry and A. Doerry (2008, 02). ”ship dynamics for maritime isar imaging”.

[21] Company, H.-P. (1985). ”the fundamentals of signal analysis”.

[22] Landberg, L. (2015). *”Meteorology for Wind Energy: An Introduction*. Wiley.

[23] GWEC (2021). ”global offshore wind report-2021”.

[24] IRENA (2022). ”renewable energy statistics 2022”. Available at `www.irena.org/Statistics/Download-Data`.

[25] Bingöl, F. (2010, March). *Complex Terrain and Wind Lidars*. Ph. D. thesis.

[26] Unnewehr, J. F., E. Jalbout, C. Jung, D. Schindler, and A. Weidlich (2021). ”getting more with less? why repowering onshore wind farms does not always lead to more wind power generation – a german case study”. *Renewable Energy 180*, 245–257.

[27] ”Siemens Gamesa launches 5.8 MW wind turbine”. `https://www.rechargenews.com/wind/siemens-gamesa-launch\-es-5-8mw-wind-turbine/2-1-579633`. Accessed: 24th of August 2022.

[28] ”The next step in our modularisation journey”. https://www.vestas.com/en/media/blog/technology/the-next-step-in-our-modularisation-journey. Accessed: 24th of August 2022.

[29] Europe, W. (February 2022). ”wind energy in europe - 2021 statistics and the outlook for 2022-2026”.

[30] IEA (2022). ”a 10-point plan to reduce the european union’s reliance on russian natural gas”. Available at https://www.iea.org/reports/a-10-point-plan-to-reduce-the-european-unions-reliance\--on-russian-natural-gas.

[31] Marijuán, A. R. (2017). ”offshore floating platforms : Analysis of a solution for motion mitigation”.

[32] GWEC (2022b). ”global offshore wind report-2022”.

[33] Robertson, A. and J. Jonkman (2011, 01). ”loads analysis of several offshore floating wind turbine concepts”. *Proceedings of the International Offshore and Polar Engineering Conference*.

[34] Wiser, R., J. Rand, J. Seel, P. Beiter, E. Baker, E. Lantz, and P. Gilman (2021, 05). ”expert elicitation survey predicts 37% to 49% declines in wind energy costs by 2050”. *Nature Energy 2021*.

[35] Jonkman, J. (2007, 01). ”dynamics modeling and loads analysis of an offshore floating wind turbine”.

[36] Sebastian, T. (2012). *The Aerodynamics and Near Wake of an Offshore Floating Horizontal Axis Wind Turbine*. Ph. D. thesis.

[37] (2013, 06). *”Variations in Ultimate Load Predictions for Floating Offshore Wind Turbine Extreme Pitching Motions Applying Different Aerodynamic Methodologies”*, Volume All Days of *International Ocean and Polar Engineering Conference*. ISOPE-I-13-102.

[38] Sebastian, T. and M. Lackner (2013, 04). ”characterization of the unsteady aerodynamics of offshore floating wind turbines”. *Wind Energy 16*, 339–352.

[39] Chen, P., J. Chen, and Z. Hu (2020, 10). ”review of experimental-numerical methodologies and challenges for floating offshore wind turbines”. *Journal of Marine Science and Application*.

[40] Chakrabarti, S. K. (1994). *”Offshore Structure Modeling”*. WORLD SCIENTIFIC.

[41] Sørensen, J. (2016). *General Momentum Theory for Horizontal Axis Wind Turbines*. Ph. D. thesis.

[42] Betz, A. (1926). *"Wind-Energie Und Ihre Ausnutzung Durch Windmuhle"*. Gottingen: Vandenhoe.

[43] Glauert, H. (1935). *"Airplane Propellers"*, Volume Vol. IV. New York.

[44] (2011). *"Aerodynamics of Horizontal Axis Wind Turbines"*, Chapter 3, pp. 39–136. John Wiley Sons, Ltd.

[45] Castro, I. (2017). "design of a 10mw wind turbine rotor blade for testing of a scaled-down floating offshore support structure".

[46] Fowler, M., R. Kimball, D. Thomas, and A. Goupee (2013, 06). "design and testing of scale model wind turbines for use in wind/wave basin model tests of floating offshore wind turbines". Volume 8.

[47] Matha, D., J. Cruz, M. Masciola, E. Bachynski-Polić, M. Atcheson, A. Goupee, S. Gueydon, and A. Robertson (2016b, 08). *"Modelling of Floating Offshore Wind Technologies"*, pp. 133–240.

[48] Sarpkaya, T. S. (2010). *"Wave Forces on Offshore Structures"*. Cambridge University Press.

[49] Jonkman, J. (2009, 07). "dynamics of offshore floating wind turbines-model development and verification". *Wind Energy 12*, 459 – 492.

[50] Svendsen, I. and I. Jonsson (1976). *Hydrodynamics of coastal regions*. Den Private ingeniørfond, Technical University of Denmark.

[51] Pedersen, P., C. Aage, and E. o. K. Danmarks Tekniske Universitet. Institut for Mekanik (2001). *"Grundlæggende skibs- og offshoreteknik"*. Danmarks Tekniske Universitet, Institut for Makanik, energi og konstruktion, Maritim teknik.

[52] Gueydon, S., I. Bayati, and E. de Ridder (2020). "discussion of solutions for basin model tests of fowts in combined waves and wind". *Ocean Engineering 209*, 107288.

[53] Skaare, B., T. Hanson, F. Nielsen, R. Yttervik, A. Hansen, K. Thomsen, T. Larsen, B. Skaare@hydro, No, T. David, F. No, Gunnar, R. Com, A. No, and Melchior (2007, 01). "integrated dynamic analysis of floating offshore wind turbines". *European Wind Energy Conference and Exhibition*.

[54] Goupee, A., B. Koo, K. Lambrakos, and R. Kimball (2012, 04). "model tests for three floating wind turbine concepts". *Offshore Technology Conference, Proceedings 3*.

[55] JM, J., S. Butterfield, W. Musial, and G. Scott (2009, 01). ”definition of a 5mw reference wind turbine for offshore system development”. *National Renewable Energy Laboratory (NREL)*.

[56] Jonkman, J. (2010, 01). ”definition of the floating system for phase iv of oc3”. *NREL technical report*.

[57] Coulling, A., A. Goupee, A. Robertson, J. Jonkman, and H. Dagher (2013, 03). ”validation of a fast semi-submersible floating wind turbine numerical model with deepcwind test data”. *Journal of Renewable and Sustainable Energy 5*.

[58] Martin, H., R. Kimball, A. Viselli, and A. Goupee (2012, 07). ”methodology for wind/wave basin testing of floating offshore wind turbines”. Volume 136.

[59] Ridder, E.-J., W. Otto, G. Zondervan, F. Huijs, and G. Vaz (2014, 06). ”development of a scaled-down floating wind turbine for offshore basin testing”. *Proceedings of the International Conference on Offshore Mechanics and Arctic Engineering - OMAE 9*.

[60] Le Boulluec, M., J. Ohana, A. Martin, and A. Houmard (2013, 06). ”tank testing of a new concept of floating offshore wind turbine”. Volume 8.

[61] Lemmer, F, A. J. M. D. A. F. C. F. B. H. and P. Montinari (2014). ”innwind.eu d4.24: Floating wind model tests ecole centrale de nantes 2014”. Technical report, Nantes.

[62] Robertson, A., J. Jonkman, M. Masciola, H. Song, A. Goupee, A. Coulling, and C. Luan (2014, 9). ”definition of the semisubmersible floating system for phase ii of oc4”.

[63] Borisade, F., C. Koch, F. Lemmer, P. W. Cheng, F. Campagnolo, and D. Matha (2018, 03). ”validation of innwind.eu scaled model tests of a semisubmersible floating wind turbine”. *International Journal of Offshore and Polar Engineering 28*, 54–64.

[64] (2013). ” the dtu 10-mw reference wind turbine ”.

[65] Kumari Ramachandran, G. (2013). *A Numerical Model for a Floating TLP Wind Turbine*. Ph. D. thesis.

[66] Roddier, D., C. Cermelli, and A. Weinstein (2009, 01). ”windfloat: A floating foundation for offshore wind turbines—part i: Design basis and qualification process”. Volume 4.

[67] Sauder, T., V. Chabaud, M. Thys, E. Bachynski-Polić, and L. Sæther (2016, 06). ”real-time hybrid model testing of a braceless semi-submersible wind turbine: Part i — the hybrid approach”. pp. V006T09A039.

[68] Urbán, A. M. and R. Guanche (2019). ”wind turbine aerodynamics scale-modeling for

floating offshore wind platform testing". *Journal of Wind Engineering and Industrial Aerodynamics 186*, 49–57.

[69] Bayati, I., M. Belloli, L. Bernini, H. Giberti, and A. Zasso (2017, 04). "scale model technology for floating offshore wind turbines". *IET Renewable Power Generation 11*.

[70] Jonkman, J. M. and M. L. Buhl, Jr (2005, 10). "fast user's guide - updated august 2005".

[71] Canet, H., P. Bortolotti, and C. L. Bottasso (2021). "on the scaling of wind turbine rotors". *Wind Energy Science 6*(3), 601–626.

[72] Mehta, R. and P. Bradshaw (1979). "design rules for small low speed wind tunnels". *The Aeronautical Journal (1968) 83*(827), 443–453.

[73] Erol, S. (2020). "scaled down modelling of a horizontal wind turbine for a floating wind turbine research". Master's thesis, Izmir.

[74] Aktaş, K. (2020). "wave generation and analysis in the laboratory wave channel to conduct experiments on the numerically modeled spar type floating wind turbine". Master's thesis, Izmir.

[75] Bruun, H. (2009, 07). "hot-wire anemometry: Principles and signal analysis". *Measurement Science and Technology 7*.

[76] Brown, D. (2009). "tracker video analysis and modelling tool".

[77] Emeis, S. (2018, 04). *"Wind Energy Meteorology - Second Edition"*.

[78] (1988). "chapter 13 marine atmospheric boundary layer". In S. P. Arya (Ed.), *Introduction to Micrometeorology*, Volume 42 of *International Geophysics*, pp. 197–222. Academic Press.

[79] Charnock, H. (1955). "wind stress on a water surface". *Quarterly Journal of the Royal Meteorological Society 81*, 639–640.

[80] IEC (2019). "iec 61400-3-1, design requirements of offshore wind turbines".

[81] Türk, M. and S. Emeis (2010). "the dependence of offshore turbulence intensity on wind speed". *Journal of Wind Engineering and Industrial Aerodynamics 98*(8), 466–471.

[82] Wang, H., R. Barthelmie, S. Pryor, and H.-G. Kim (2014, 10). "a new turbulence model for offshore wind turbine standards". *Wind Energy 17*.

[83] Stull, R. (1988). *"An Introduction to Boundary Layer Meteorology"*. Atmospheric and Oceanographic Sciences Library. Springer Netherlands.

[84] Goda, Y. (2010). *"Random Seas and Design of Maritime Structures"* (3rd ed.). WORLD SCIENTIFIC.

[85] "jrk g2 18v27 usb motor controller with feedback". `https://www.pololu.com/product/3148`. Accessed: 16th of October 2022.

[86] "20.4:1 metal gearmotor 25dx65l mm hp 12v with 48 cpr encoder". `https://www.pololu.com/product/4843`. Accessed: 16th of October 2022.

# APPENDIX A

# SIGNAL ANALYSIS

In signal analysis, the variable can be examined in both the time and frequency domains without data loss, as shown in Figure A.1. Time-dependent variation of the 2-dimensional motions was obtained during the experiment in this study. In order to evaluate this data in detail and detect hidden effects that may not be visible in the time series, the data has also been translated into the frequency domain (21).

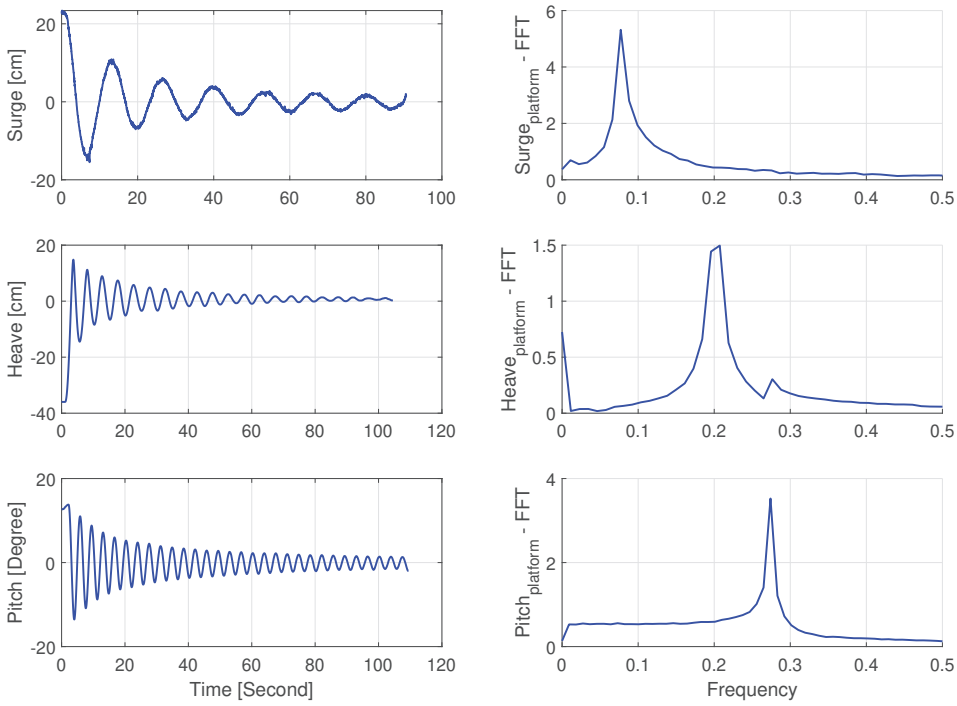


Figure A.1. Frequency spectrum of data according to time series

Furthermore, the y-axis that show amplitude is scaled logarithmically to make minor effects even more visible, which compresses large signal amplitudes and expands small amplitudes. Figure A.2 shows same data in log and linear scale for comparison.

(a) Linear amplitude scale (b) Logarithmic amplitude scale

Figure A.2. Two different amplitude scale for same data (21)

Issues must be considered when converting time series data to the frequency domain (21). The first of these is the ”aliasing” problem. When the sampling rate $f_s$ of our sensor is not greater than twice the maximum frequency of our signal $f_{max}$, which occurs during the experiment, undesired aliasing appears. Figure A.3 depicts the aliased signal, and removing this signal from the spectrum is not possible with filtering since it is an artifact of Fourier Transformation (21). This minimum sample requirement is known as Nyquist criteria, and the formula is given below:

$$f_s > 2.f_{max} \tag{A.1}$$

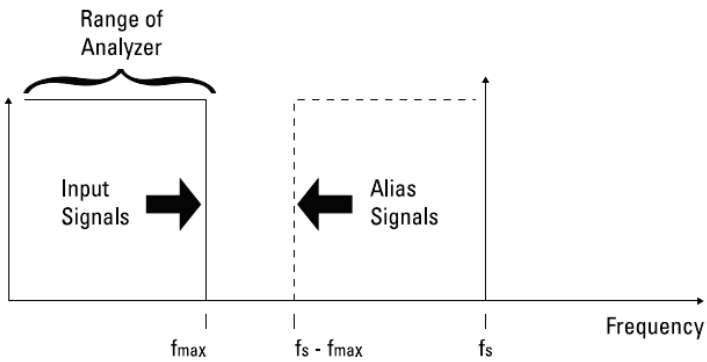


Figure A.3. Condition of aliasing occurrence in the frequency domain (21)

As another precaution, leakage shall be considered. Leakage occurs in the spectrum if the combination of the edges (beginning, ending) of the time-recorded signal is not periodic. Therefore, instead of single or multiple peaks in the spectrum, the signal amplitude is spread into the entire spectrum range, as seen in Figure A.4. Various windowing

schemes are used to avoid leakage (21).

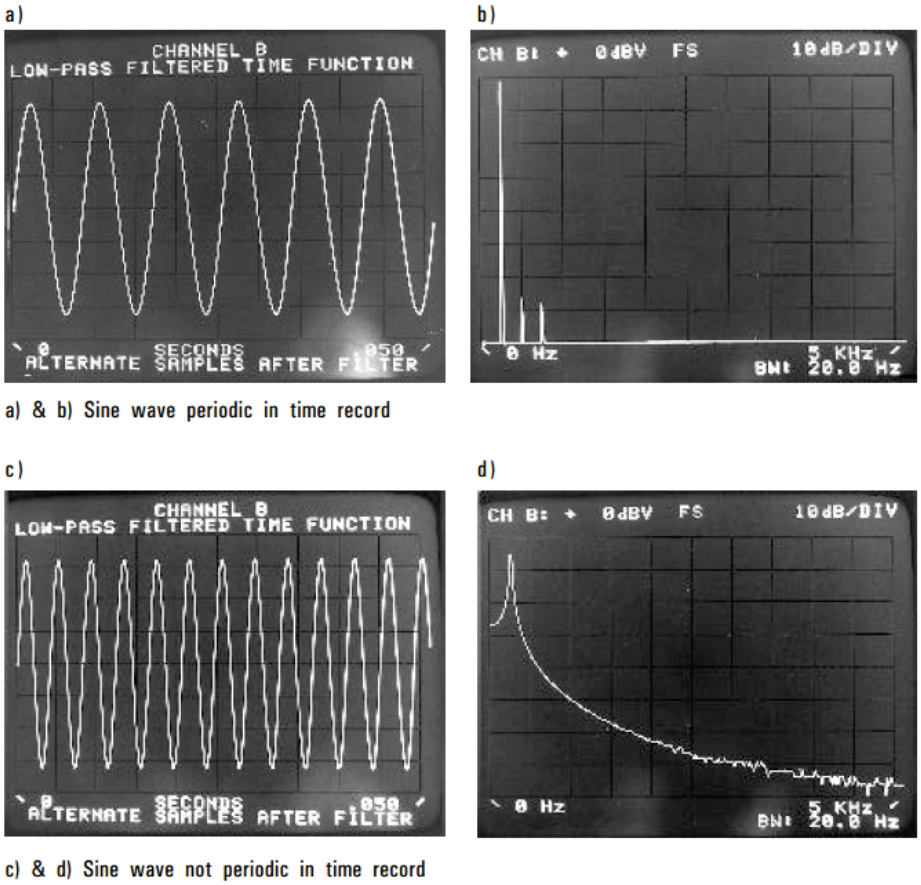


Figure A.4. The smeared amplitude in the entire frequency range which is known as the leakage problem (21)

# APPENDIX B

# CALIBRATION PROCESS OF HOT-WIRE ANEMOMETER

In order to calibrate the hot-wire, first of all, the hot-wire is connected to the IFA300 cabinet in one of the first two channels, which is a constant temperature anemometer channel in 8 channels; the schematic view is shown in Figure B.1.

Since the current BNC connecter board does not work, the signal is collected with the Advantech PCI-1710 HCG DAQ card from the A/D converter board output of the hot-wire channel.

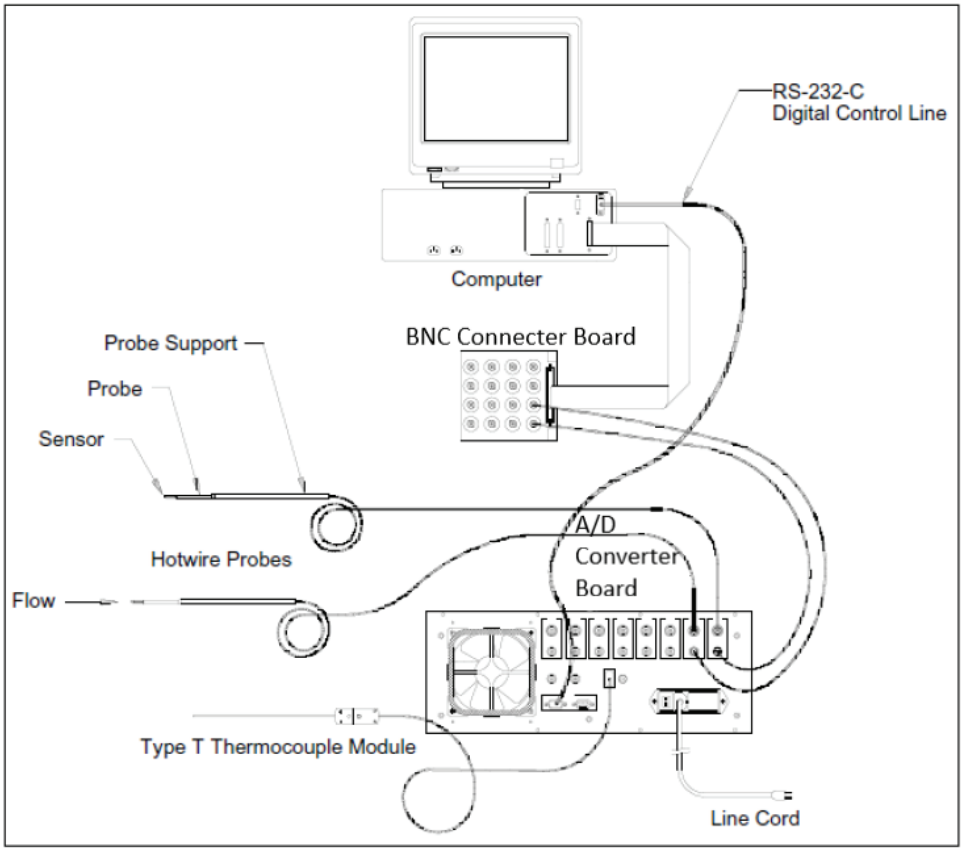


Figure B.1. Schematic view of the IFA 300 Constant Temperature Anemometer System

1. Complete the connections of Hot-wire, IFA300 cabinet, and DAQ card, as depicted in Figure B.1. Next, connect the GND and signal outputs from the A/D board to

channels 60 (60th channel: AI GND) and 68 (68th channel: Analog Input) on the DAQ card.

2. In the ”ThermalPRO” interface, open the IFA300 Communication tab shown in Figure B.3. After selecting the single wire type, which is the hot-wire type used in the experiment, from the probe types, measure the probe resistance from the Measure box.

3. After making sure that the hot-wire and BNC connector are disconnected, connect the closed connector to the free end of the BNC cable and measure the cable resistance from the measure box.

4. Go to Calibration $\rightarrow$ Probe Data tab (Figure B.2) and enter probe type, no of IFA channel, measured cable resistance and operate resistance, then set offset to 0 and gain to 1.

5. After entering the information, create a dummy calibration file with the ”Save as” button and go directly to the Acquisition-Probe tab instead of the ”Next screen” button. Then, run hot-wire with the saved calibration file.

6. Open the block diagram created in the LabVIEW program to collect the data on the DAQ card, control algorithm of the program is shown in Figure B.4. Next, calculate the offset and gain values within the $\pm$ 10 Volt limits of the DAQ card by giving the hot-wire the minimum and maximum velocities it encounters during the experiment at the calibration nozzle.

7. After repeating steps 4 and 5 with the new offset and gain values, measure at least 14 different velocities, which are also measured externally with a pitot tube, between the minimum and maximum velocities through LabVIEW.

8. The hot-wire can be used to measure the velocity of air after it has been calibrated against the pitot tube with measurements from LabVIEW.

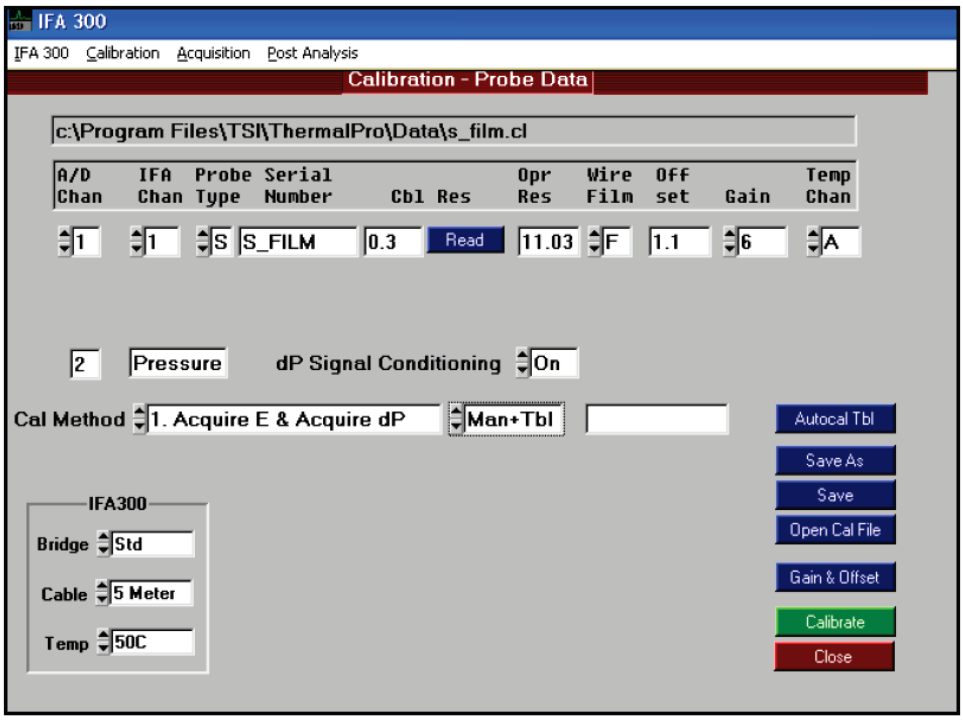


Figure B.2. Calibration - Probe Data screen of the IFA 300

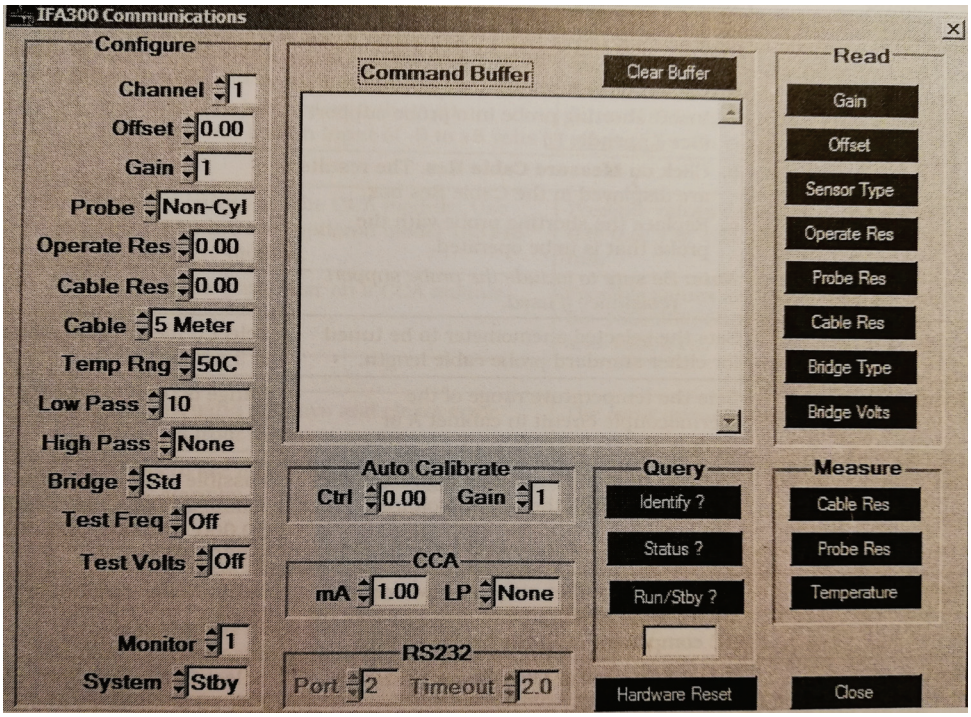


Figure B.3. Communications screen of the IFA 300

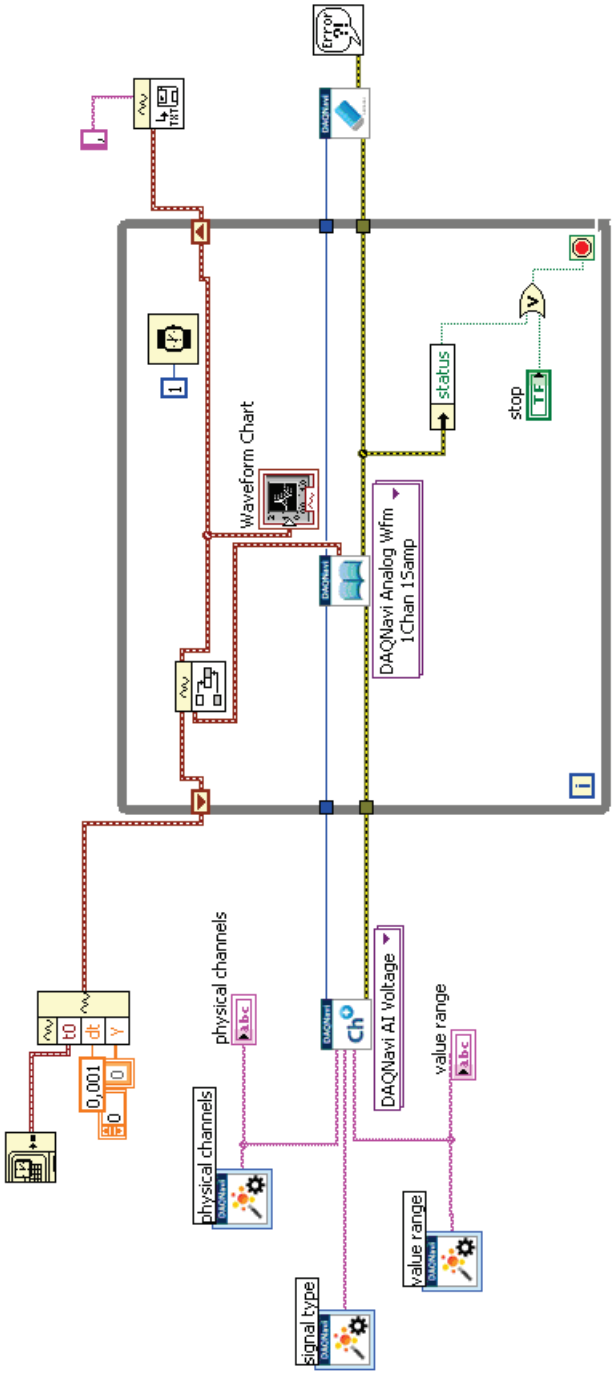


Figure B.4. Block diagram of LabVIEW for the calibration

# APPENDIX C

# DECOMPOSITION CODE OF COUPLED MOTION

```
clc;
clear;
close all;
%% Decomposition of coupled motion

%Arrange the readtable input based on the experiment output
Data = readtable('rotated_GOPR2817.csv');

        dt=1/119.88; %Camera fps

        x1=Data(:,2); %Point 1 x coordinate
        y1=Data(:,3); %Point 1 y coordinate
        x2=Data(:,6); %Point 2 x coordinate
        y2=Data(:,7); %Point 2 y coordinate

        x1=table2array(x1);
        y1=table2array(y1);
        x2=table2array(x2);
        y2=table2array(y2);

        len = length(x1);
        dist = 1.40343; %Real distance between Point 1 and CoG

        for i=1:len
            %Calculation of distance between Point 1 and Point 2
            Distance_point1_point2(i)=sqrt((x1(i)-x2(i))^2...
                                    +(y1(i)-y2(i))^2);

            %Calculation of angle between Point 1 and Point 2
            Angle(i) = atan((y1(i)-y2(i))/(x1(i)-x2(i)))*(180/pi);
```

```
    if Angle(i)<=0
       Angle(i)=Angle(i)+180;
    end
   Angle(i)=-Angle(i);
end

mean_distance =mean(Distance_point1_point2);

for i=1:len
    %CoG can be calculated mathematically.
    CoG_x(i)= x1(i) + (dist * cos(deg2rad(Angle(i))));
    CoG_y(i)= y1(i) + (dist * sin(deg2rad(Angle(i))));
    Center_of_gravity(i,:) = [CoG_x(i) CoG_y(i)];
end

for i=1:len-1
     time(i)=dt*i;
     surge(i) = CoG_x(i+1)-CoG_x(i);
     heave(i) = CoG_y(i+1)-CoG_y(i);
     pitch(i) = atan((y1(i+1)-heave(i)-y1(i))...
                /(x1(i+1)-surge(i)-x1(i)))*(180/pi);
end

k =0;
u= 0;

for i=1:len-1
   k=k+surge(i);
   total_surge(i) = k; %Add all individual surge respectively.
   u=u+heave(i);
   total_heave(i) = u; %Add all individual heave respectively.
end

figure
subplot(1,3,1);
plot(time,total_surge,'k-','LineWidth',0.5)
```

```
ylim([-0.5 0.5]) %Limit adjustment can be made according to test
grid on;
title('Surge [m]')
subplot(1,3,2);
plot(time,total_heave,'k-','LineWidth',0.5)
ylim([-0.2 0.2]) %Limit adjustment can be made according to test
grid on;
title('Heave [m]')
subplot(1,3,3);
plot(time,pitch,'k-','LineWidth',0.5)
ylim([-10 10]) %Limit adjustment can be made according to test
grid on;
title('Pitch [Degree]')
suptitle('Irregular Wave Experiment')
```

# APPENDIX D

# WIND TURBINE'S MOTOR

It is seen that it is impossible (with a very low torque coefficient) for the model turbine to reach 316.22 rpm at a wind speed of 3.16 m/s on its own; thus, the rotor must be driven by the motor to achieve the desired speed. Therefore, the motor and driver with PID controller were used in this study, and Table D.1 shows the name of the instruments.

Table D.1. Details of instruments of wind turbine motor's

| **Instrument** | **Part Number** | **Part Name** |
|---|---|---|
| Motor | Pololu #4843 | 20.4:1 Metal Gearmotor 25Dx65L mm HP 12 with 48 CPR Encoder |
| Driver | Pololu #3148 | Jrk G2 18v27 USB Motor Controller with Feedback |

After the motor-driver-computer connections are completed, the driver's recommended voltage (24 Volt) is provided with a power supply. Details about instruments, connections, and setup can be found on Pololu's official webpage (85, 86). With the "Pololu Jrk G2 Configuration Utility" program, which is downloaded to the computer, the PID settings of the motor are tuned and driven with this interface.

Since direct rpm control cannot be done through the interface, the rpm value, which is a function of the target value in the interface, is recorded based on the target value, as shown in Table D.2. Rotor rotation direction may change depending on where motor power terminals are connected. According to the last connection configuration, Target (counterclockwise$< 2048$, clockwise$> 2048$) is raised above $2048$.

Table D.2. Preliminary study outputs of wind turbine motor's

| **Target** | **Measured rpm** | **Duty Cycle Target** | **Duty Cycle Target [%]** |
|---|---|---|---|
| 2051 | 66 | 67 | 11 |
| 2052 | 82 | 89 | 15 |
| 2053 | 99 | 102 | 17 |
| 2054 | 113 | 120 | 20 |
| 2055 | 132 | 141 | 24 |
| 2056 | 150 | 169 | 28 |
| 2057 | 163 | 184 | 31 |
| 2058 | 182 | 211 | 35 |
| 2059 | 200 | 236 | 39 |
| 2060 | 212 | 253 | 42 |
| 2061 | 232 | 283 | 47 |
| 2062 | 250 | 312 | 52 |
| 2063 | 261 | 341 | 57 |
| 2064 | 281 | 383 | 64 |
| 2065 | 298 | 400 | 67 |
| 2066 | 316 | 428 | 71 |

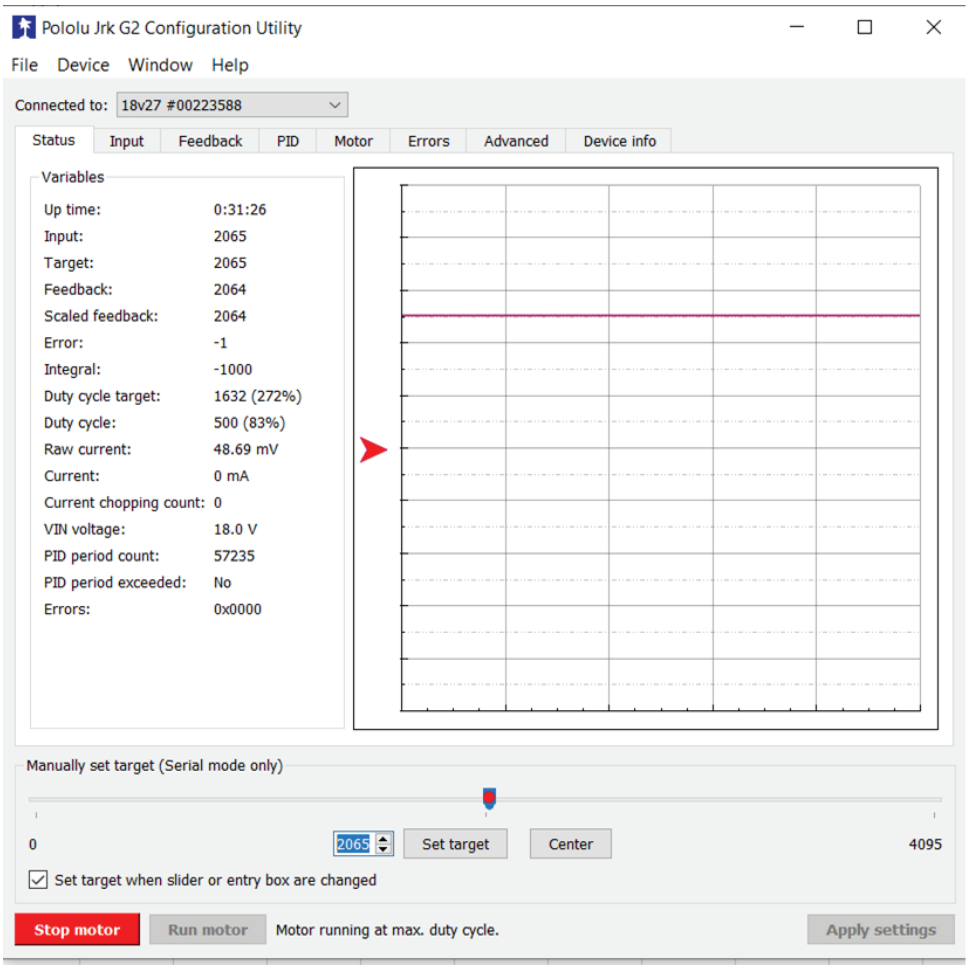


Figure D.1. The Pololu Jrk G2 Configuration Utility user interface